

# Colossal Strain Tuning of Ferroelectric Transitions in $\text{KNbO}_3$ Thin Films

Sankalpa Hazra, Tobias Schwaigert, Aiden Ross, Haidong Lu, Utkarsh Saha, Victor Trinquet, Betül Akkopru-Akgun, Benjamin Z. Gregory, Anudeep Mangu, Suchismita Sarker, Tatiana Kuznetsova, Saugata Sarker, Xin Li, Matthew R. Barone, Xiaoshan Xu, John W. Freeland, Roman Engel-Herbert, Aaron M. Lindenberg, Andrej Singer, Susan Trolier-McKinstry, David A. Muller, Gian-Marco Rignanese, Salva Salmani-Rezaie, Vladimir A. Stoica, Alexei Gruverman, Long-Qing Chen, Darrell G. Schlom, and Venkatraman Gopalan\*

Strong coupling between polarization ( $P$ ) and strain ( $\varepsilon$ ) in ferroelectric complex oxides offers unique opportunities to dramatically tune their properties. Here colossal strain tuning of ferroelectricity in epitaxial  $\text{KNbO}_3$  thin films grown by sub-oxide molecular beam epitaxy is demonstrated. While bulk  $\text{KNbO}_3$  exhibits three ferroelectric transitions and a Curie temperature ( $T_c$ ) of  $\approx 676$  K, phase-field modeling predicts that a biaxial strain of as little as  $-0.6\%$  pushes its  $T_c > 975$  K, its decomposition temperature in air, and for  $-1.4\%$  strain, to  $T_c > 1325$  K, its melting point. Furthermore, a strain of  $-1.5\%$  can stabilize a single phase throughout the entire temperature range of its stability. A combination of temperature-dependent second harmonic generation measurements, synchrotron-based X-ray reciprocal space mapping, ferroelectric measurements, and transmission electron microscopy reveal a single tetragonal phase from 10 K to 975 K, an enhancement of  $\approx 46\%$  in the tetragonal phase remanent polarization ( $P_r$ ), and a  $\approx 200\%$  enhancement in its optical second harmonic generation coefficients over bulk values. These properties in a lead-free system, but with properties comparable or superior to lead-based systems, make it an attractive candidate for applications ranging from high-temperature ferroelectric memory to cryogenic temperature quantum computing.

## 1. Introduction

The ability to apply large strains in epitaxial thin films makes it possible to engineer emergent phases in materials with enhanced material properties that are inaccessible in their bulk form.<sup>[1]</sup> Owing to a strong coupling between strain and polar order in ferroelectrics, large shifts in properties such as paraelectric-to-ferroelectric transition temperature ( $T_c$ ) and remanent polarization ( $P_r$ ) have been theoretically predicted and experimentally observed.<sup>[2-6]</sup> Notable examples of strain-enhanced properties and tunable phase transitions in perovskite oxides include a large shift in  $T_c$  in  $\text{BaTiO}_3$ ,<sup>[2]</sup> observation of room temperature ferroelectricity in quantum paraelectric  $\text{SrTiO}_3$ ,<sup>[3,4]</sup> and the realization of super-tetragonal  $\text{BiFeO}_3$ .<sup>[7]</sup> Given that there are practical limits to epitaxially straining a ceramic thin film on a rigid single crystal substrate to typically a few percent (a maximum

S. Hazra, A. Ross, U. Saha, B. Akkopru-Akgun, T. Kuznetsova, S. Sarker, S. Trolier-McKinstry, V. A. Stoica, L.-Q. Chen, V. Gopalan  
Department of Materials Science and Engineering  
Pennsylvania State University  
University Park, PA 16802, USA  
E-mail: [vgopalan@psu.edu](mailto:vgopalan@psu.edu)

 The ORCID identification number(s) for the author(s) of this article can be found under <https://doi.org/10.1002/adma.202408664>

© 2024 The Author(s). Advanced Materials published by Wiley-VCH GmbH. This is an open access article under the terms of the [Creative Commons Attribution](#) License, which permits use, distribution and reproduction in any medium, provided the original work is properly cited.

DOI: 10.1002/adma.202408664

T. Schwaigert, M. R. Barone  
Platform for the Accelerated Realization, Analysis, and Discovery of Interface Materials (PARADIM)  
Cornell University  
Ithaca, NY 14853, USA

T. Schwaigert, M. R. Barone, A. Singer, D. G. Schlom  
Department of Materials Science and Engineering  
Cornell University  
Ithaca, NY 14853, USA

H. Lu, X. Li, X. Xu, A. Gruverman  
Department of Physics and Astronomy  
University of Nebraska  
Lincoln, NE 68588, USA

of 6.6% has been demonstrated<sup>[7]</sup>), one ideally desires the maximum strain *tunability* of the film properties, measured in units of property per unit strain, such as  $\frac{dT_c}{d\varepsilon}$  and  $\frac{dP_r}{d\varepsilon}$ .

Moreover, to achieve the desired phase over a broad temperature range, undesirable thermal phase transitions require suppression. For instance, in BaTiO<sub>3</sub>-based electrooptic modulators employed in quantum computing at cryogenic temperatures, symmetry-lowering phase transitions in BaTiO<sub>3</sub> significantly diminish the superior electrooptic properties of the room-temperature tetragonal phase.<sup>[8]</sup> Stabilization of the tetragonal phase in this system at cryogenic operational temperatures would thus be ideal. For high-temperature ferroelectric memory and actuation applications, the stabilization of ferroelectricity at high temperatures through a large  $T_c$  is desired. Further, environmentally benign ferroelectrics<sup>[9,10]</sup> are desired, in contrast to Pb-based ferroelectrics.

Strain tuning of environmentally benign perovskite alkali niobates have been explored due to their strong ferroelectricity,<sup>[11]</sup> piezoelectricity,<sup>[12,13]</sup> and nonlinear optical responses.<sup>[14]</sup> In (Na,K)NbO<sub>3</sub> films, strain tuning proves to be an effective pathway

to control phase transitions,<sup>[15,16]</sup> while allowing properties competing with those of Pb-based ferroelectrics.<sup>[17]</sup> Unfortunately, NaNbO<sub>3</sub> is highly polymorphic as compared with KNbO<sub>3</sub>, making pure KNbO<sub>3</sub> a more suitable material system to establish a single structural phase across a large temperature range.<sup>[18]</sup> While strain-relaxed KNbO<sub>3</sub> films have been studied,<sup>[19–24]</sup> strain tuning of this Pb-free, environmentally benign system has not been explored thus far. Furthermore, prior demonstrations of the growth of KNbO<sub>3</sub> on a silicon substrate<sup>[25,26]</sup> make KNbO<sub>3</sub> appealing for semiconductor device integration.

In this work, we demonstrate that strain-tuning of KNbO<sub>3</sub> provides a colossal strain tunability of its  $T_c$ , while retaining the desirable tetragonal phase from 10 K to 975 K, its decomposition temperature in air. Strain mediates the stabilization of a superior tetragonal phase in KNbO<sub>3</sub>, mimicking the tetragonality of PbTiO<sub>3</sub> but with much higher  $T_c$ , and significantly larger nonlinear optical coefficients.

## 2. Theory Prediction of the Strain Phase Diagram

Bulk KNbO<sub>3</sub> has a rich phase diagram undergoing a series of phase transitions from cubic to tetragonal at 676 K, tetragonal to orthorhombic at 492 K, and eventually orthorhombic to rhombohedral at 223 K.<sup>[11]</sup> To predict the influence of biaxial strain on the lattice parameters and temperature-dependent phase diagram of KNbO<sub>3</sub>, we performed phase-field simulations of biaxially compressed KNbO<sub>3</sub> thin films.

**Figure 1a** depicts the phase diagram predicted from phase-field simulations as a function of biaxial epitaxial strain,  $\varepsilon = (a_{\parallel} - a_o)/a_o$ , where  $a_o$  is the effective cubic lattice parameter extrapolated from the high-temperature KNbO<sub>3</sub> cubic phase and  $a_{\parallel}$  is the in-plane lattice parameter of the biaxially strained KNbO<sub>3</sub>. Under a compressive strain of  $\approx -0.7\%$ , it is possible to stabilize the high-temperature tetragonal phase at room temperature where the orthorhombic phase is observed in its bulk counterpart. Further, a strain of  $\approx -1.5\%$  is sufficient to stabilize the tetragonal phase down to 0 K, eliminating all other phase transitions. At such strains, the Curie temperature,  $T_c$  is predicted to be enhanced beyond its melting temperature of 1325 K<sup>[18]</sup> as seen in **Figure 1a**. Strikingly, the rate of change of  $T_c$  with respect to strain, i.e.,  $\frac{dT_c}{d\varepsilon}$ , is predicted to be a factor of  $\approx 3 \times$  higher compared to most well-known ferroelectrics as shown in **Figure 1b**, while its rate of change of remanent polarization with respect to strain,  $\frac{dP_r}{d\varepsilon}$ , is predicted to be intermediate between that of tetragonal BiFeO<sub>3</sub><sup>[27]</sup> and PbZr<sub>0.3</sub>Ti<sub>0.7</sub>O<sub>3</sub>.<sup>[28]</sup>

The superior stability of the tetragonal phase under higher compressive strains is driven by its better match with strain conditions imposed by the substrate, resulting in minimal elastic energy in comparison to other possible phases. For lower compressive strains, KNbO<sub>3</sub> is predicted to undergo a transition from the tetragonal to a lower symmetry monoclinic phase instead of an orthorhombic phase as seen in bulk KNbO<sub>3</sub>. This is because of the large enhancement of the  $c/a$  lattice parameter ratio (**Figure 1c**) due to the epitaxial clamping to the substrate, effectively distorting the orthorhombic phase in bulk KNbO<sub>3</sub> into a monoclinic phase under compressive strain (see Supporting Information). At room temperature, the  $c/a$  ratio increases from its bulk value of  $\approx 1.01$  (similar to that of bulk BaTiO<sub>3</sub>) to a value of  $\approx 1.07$  (larger

V. Trinquet, G.-M. Rignanese  
Institute of Condensed Matter and Nanosciences  
UCLouvain

Louvain-la-Neuve 1348, Belgium

B. Z. Gregory  
Department of Physics

Cornell University  
Ithaca, NY 14853, USA

A. Mangu, A. M. Lindenberg  
Department of Materials Science and Engineering  
Stanford University  
Stanford, CA 94305, USA

A. Mangu, A. M. Lindenberg  
Stanford Institute for Materials Energy Sciences  
SLAC National Accelerator Laboratory  
Menlo Park, CA 94025, USA

S. Sarker  
Cornell High Energy Synchrotron Source  
Cornell University  
Ithaca, NY 14853, USA

J. W. Freeland  
Advanced Photon Source  
Argonne National Laboratory  
Argonne, IL 60439, USA

R. Engel-Herbert  
Paul-Drude-Institut für Festkörperelektronik  
Leibniz-Institut im Forschungsverbund Berlin e.V.  
Hausvogteiplatz 5, 10117 Berlin, Germany

D. A. Muller  
School of Applied and Engineering Physics  
Cornell University  
Ithaca, NY 14853, USA

S. Salmani-Rezaie  
Department of Materials Science and Engineering  
Ohio State University  
Columbus, OH 43210, USA

S. Salmani-Rezaie, D. G. Schlom  
Kavli Institute at Cornell for Nanoscale Science  
Ithaca, NY 14853, USA

D. G. Schlom  
Leibniz-Institut für Kristallzüchtung  
Max-Born-Straße 2, 12489 Berlin, Germany

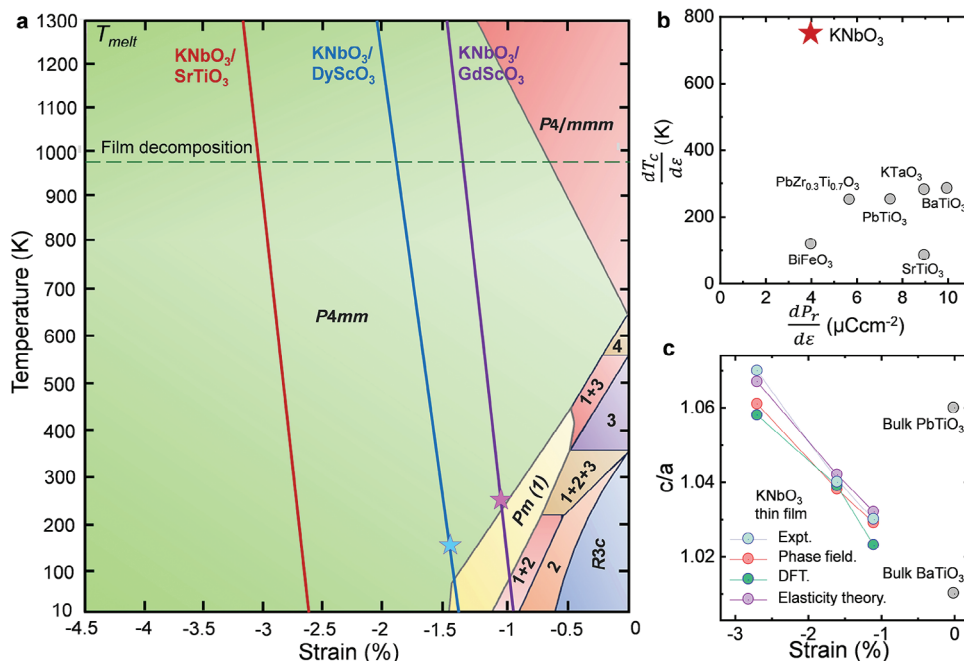


**Figure 1.** a) Thermodynamic phase-field simulations of biaxially compressed KNbO<sub>3</sub>. The three different strain films on SrTiO<sub>3</sub>, DyScO<sub>3</sub>, and GdScO<sub>3</sub> studied here are marked by red, blue, and violet lines. Legend for numerically labeled phases: 1: *Pm*, 2: *Cm*, 3: *Amm*<sub>2</sub>, 4: Phase mixture of *P4mm* with *c*-axis poled in the in-plane direction and out-of-plane direction. Blue and violet stars indicate the onset of the tetragonal-to-monoclinic transition temperature observed experimentally. b)  $\frac{dT_c}{d\varepsilon}$  and  $\frac{dP_r}{d\varepsilon}$  plotted for KNbO<sub>3</sub> in comparison to related materials: BaTiO<sub>3</sub>,<sup>[27,75]</sup> PbTiO<sub>3</sub>,<sup>[1,27,76]</sup> PbZr<sub>0.3</sub>Ti<sub>0.7</sub>O<sub>3</sub>,<sup>[28,77]</sup> SrTiO<sub>3</sub>,<sup>[3,78]</sup> KTaO<sub>3</sub>,<sup>[79,80]</sup> and BiFeO<sub>3</sub>.<sup>[7,27,81]</sup>  $\frac{dT_c}{d\varepsilon}$  for KNbO<sub>3</sub> is labeled by predicted values from phase-field simulations. c) *c/a* ratio (out-of-plane to in-plane lattice parameter ratio) plotted as a function of strain experimentally measured for KNbO<sub>3</sub> thin films at room temperature compared to phase-field predictions, DFT calculations, and elasticity theory calculations (see Supporting information), showing the effect of strain in enhancing the stability of the tetragonal phase in KNbO<sub>3</sub>.

than that for bulk PbTiO<sub>3</sub>) at  $-2.7\%$  strain. The polarization direction and lattice structure of the strain-stabilized tetragonal and monoclinic phases in the KNbO<sub>3</sub> thin films are shown in Figure S1 (Supporting Information).

Density functional theory calculations also predict the stability of the monoclinic phase to be comparable to the tetragonal phase for intermediate strains (Figure S2, Supporting Information). From finite-temperature phase-field simulations, it is evident that for higher compressive strains (more than  $\approx -1.5\%$ ) all symmetry-lowering phase transitions can be eliminated and the single desirable tetragonal phase can be stabilized across the entire temperature regime from 0 K to  $T_c$ .

From thermodynamic calculations, the Curie temperature,  $T_c$ , for the tetragonal *c*-phase under a biaxial compressive strain (*c*-axis perpendicular to the substrate) is given by,

$$T_c(\varepsilon) = T_c(\varepsilon = 0) + 4\varepsilon_0 C \left( \frac{Q_{13}}{S_{11} + S_{13}} \right) |\varepsilon| \quad (1)$$

where  $C$  is the Curie–Weiss constant,  $Q$  is the electrostrictive coefficient,  $S$  is the elastic compliance, and  $\varepsilon_0$  is the vacuum permittivity. Comparing the  $C$ ,  $Q$ , and  $S$  of KNbO<sub>3</sub> versus those for PbTiO<sub>3</sub>, BaTiO<sub>3</sub>, and SrTiO<sub>3</sub>, (Table S3 Supporting Information) it is evident that the strong sensitivity of  $T_c$  to strain is predominantly due to a larger electrostrictive coefficient,  $Q_{13}$ , in KNbO<sub>3</sub>. For example,  $C$ ,  $\frac{1}{S_{11} + S_{13}}$ , and  $Q_{13}$  are  $\approx 6\%$ ,  $\approx 40\%$ , and  $\approx 200\%$

larger in KNbO<sub>3</sub> relative to PbTiO<sub>3</sub>, thus leading to a  $\approx 3 \times$  larger  $\frac{dT_c}{d\varepsilon}$ .

Following Equation (1), it is evident that a larger  $Q_{13}$  and lower  $S_{11} + S_{13}$  translates to a higher  $T_c$  and  $\frac{dT_c}{d\varepsilon}$ . Unfortunately, this linear relationship does not extend to the case of  $P_r$  and  $\frac{dP_r}{d\varepsilon}$ , where there are optimal values for  $Q$  and  $S$  which maximize  $P_r$  and  $\frac{dP_r}{d\varepsilon}$ , as shown in Figure S3 (Supporting Information). In particular, the  $Q_{13}$  and  $S_{11} + S_{13}$  values of KNbO<sub>3</sub> do not optimize the maximum possible value of  $P_r$  and  $\frac{dP_r}{d\varepsilon}$ ; nonetheless these values are highly competitive with other material systems as shown in Figure 1b.

### 3. Epitaxy and Phase Transitions by Optical Second Harmonic Generation

To experimentally measure the strain phase diagram, single crystal (001)<sub>c</sub> SrTiO<sub>3</sub>, (110)<sub>o</sub> DyScO<sub>3</sub>, and (110)<sub>o</sub> GdScO<sub>3</sub> (subscript “c” for cubic, “o” for orthorhombic) were used as compatible substrates, which allows us to impart compressive strain,  $\varepsilon$ , of  $\approx -2.7\%$ ,  $-1.6\%$ , and  $-1.1\%$ , respectively, on (001) KNbO<sub>3</sub> films. (To be precise, the biaxial in-plane strain for the scandate substrates is anisotropic, namely  $-1.65\%$  and  $-1.5\%$  for DyScO<sub>3</sub>, and  $-1.15\%$  and  $-1.05\%$  for GdScO<sub>3</sub>. Note that this difference was not experimentally resolved and is hence ignored in the rest of this study). Epitaxial KNbO<sub>3</sub> thin films were grown by suboxide molecular-beam epitaxy with in situ reflection high-energy

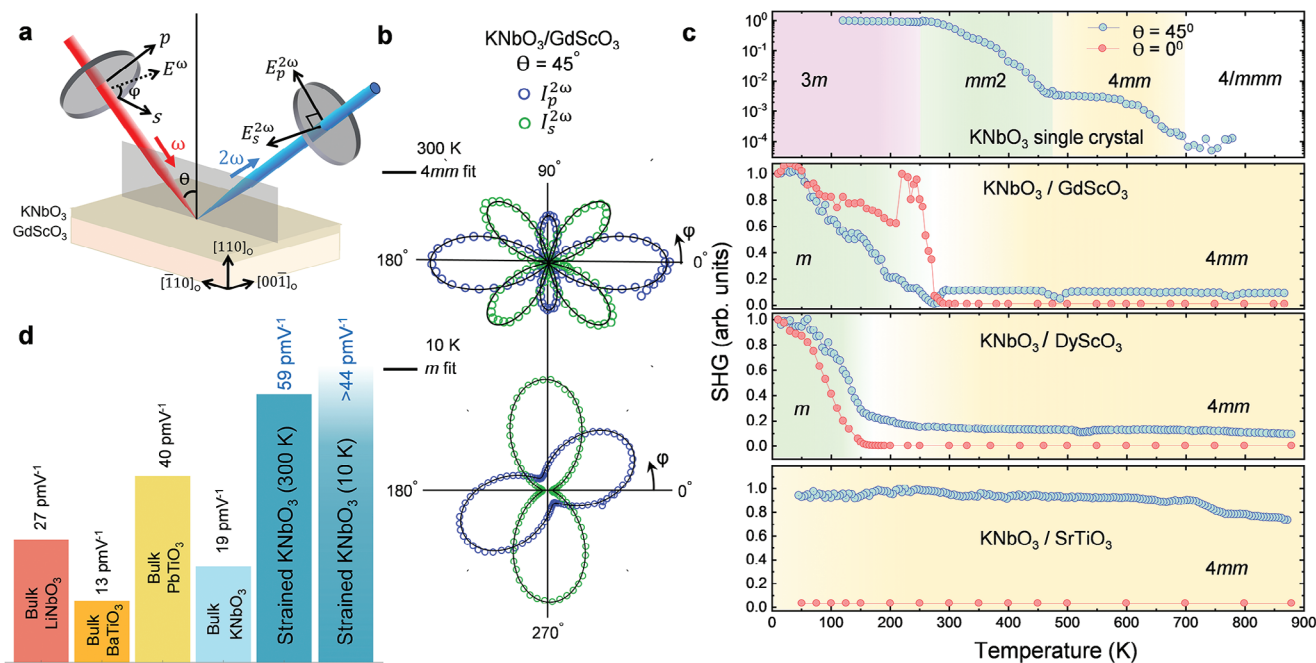


**Figure 2.** a) Schematic of second harmonic generation (SHG) setup in reflection geometry. b) SHG polar plots for KNbO<sub>3</sub> on GdScO<sub>3</sub> at 300 K (upper panel) and 10 K (lower panel) fitted to tetragonal and multidomain monoclinic models, respectively, showing symmetry lowering from room temperature to low temperature consistent with phase-field predictions. Equations for SHG modeling are discussed in the Supporting information. c) Normal and oblique-incidence SHG intensity versus temperature between 10 K and 900 K shown for bulk KNbO<sub>3</sub> single crystal, and strained KNbO<sub>3</sub> films on GdScO<sub>3</sub>, DyScO<sub>3</sub>, and SrTiO<sub>3</sub> substrates. Bulk phase transition temperatures are consistent with previous reports. Normal-incidence SHG signal (red traces) shows signatures of transition from tetragonal to a lower symmetry monoclinic phase since it is sensitive only to the latter phase. With increasing compressive strain, this symmetry-lowering phase transition (marked by green regions) is pushed down in temperature and eventually eliminated in the highest strained KNbO<sub>3</sub> on SrTiO<sub>3</sub>. d) Nonlinear optical coefficients ( $d_{33}$ ) calculated from SHG modeling for KNbO<sub>3</sub> thin films for both 300 K and 10 K compared to bulk room temperature values in similar materials. Due to the multidomain model for the low temperature monoclinic phase, only a lower bound for the  $d_{11}$  monoclinic coefficient could be extracted.

electron diffraction (RHEED) (Figure S4, Supporting information). Atomic force microscopy (AFM) was used to confirm smooth surface morphology with root-mean-square (rms) roughness < 1 nm for all three films (Figure S5, Supporting information). X-ray reciprocal space mapping (RSM) confirms the commensurately strained nature of the thin films on all three substrates (Figures S6 and S7, Supporting information). Cross-sectional transmission electron microscopy shows a uniform interface structure with minimum interface intermixing, with the film being coherently strained to the substrate with no extended defects (Figures S8–S11 Supporting information). X-ray photoemission spectroscopy confirms the expected valence states of K, Nb, and O in KNbO<sub>3</sub> films (Figure S12, Supporting Information).

To experimentally identify the phase diagram of the strained KNbO<sub>3</sub> thin films, temperature-dependent second harmonic generation (SHG) measurements were performed. Electric-dipole SHG is a nonlinear optical process where incident light at the fundamental frequency of  $\omega$  is converted into the SHG frequency of  $2\omega$  due to the broken inversion symmetry in the material.<sup>[29]</sup> A schematic of the setup used for SHG measurements is shown in Figure 2a. By rotating the incident polarization of light at the fundamental frequency, SHG polar plots can be measured corresponding to two orthogonally polarized ( $s$  and  $p$ -polarized) second harmonic light reflected from the sample surface; this is called SHG polarimetry. By fitting the polar plots, the point group symmetry of the thin films can be determined.

Figure 2b shows the oblique incidence SHG polarimetry for the KNbO<sub>3</sub> on GdScO<sub>3</sub> film (lowest biaxial strain,  $\epsilon \approx -1.1\%$ ) at 300 K fitted to a  $4mm$  (tetragonal) model (see Supporting information), validating the influence of the strain in stabilizing a tetragonal phase of KNbO<sub>3</sub> at room temperature even for the lowest strained thin film of the set. A tetragonal unit cell with polarization completely out-of-plane will exhibit no SHG signal at normal incidence. Nonetheless, symmetry lowering from a tetragonal to a lower symmetry phase will generate SHG at normal incidence due to the appearance of an in-plane polarization component in lower symmetry phases. Temperature-dependent SHG at normal incidence indeed shows that KNbO<sub>3</sub> on GdScO<sub>3</sub> undergoes critical behavior  $\approx 275$  K, below which a non-zero SHG intensity is observed in this geometry (Figure 2c). In oblique incidence, the SHG intensity increases below  $\approx 275$  K reaching  $10 \times$  the room temperature intensity at 10 K. Following phase-field predictions, the low-temperature SHG polarimetry can be fitted to a multidomain monoclinic  $m$  model (see Supporting information), shown in the lower panel of Figure 2b for KNbO<sub>3</sub> on GdScO<sub>3</sub> at 10 K. Note that a multidomain orthorhombic  $mm2$  symmetry can also be used to fit the polar plots at low-temperature. Hence, to conclusively determine the symmetry of the low-temperature phase, complementary temperature-dependent x-ray diffraction studies are necessary as discussed in Section 4.

The phase transition from tetragonal to a lower symmetry phase is further suppressed to  $\approx 150$  K for the  $\text{KNbO}_3$  on  $\text{DyScO}_3$  film ( $\epsilon \approx -1.6\%$ ), while for the highest strained  $\text{KNbO}_3$  on  $\text{SrTiO}_3$  ( $\epsilon \approx -2.7\%$ ), the low-temperature phase is completely absent, as evidenced from the temperature-dependence of normal and oblique incidence SHG amplitude as well as from the SHG polarimetry for both films (Figures S13 and S14, Supporting information). The observed phase transition temperatures are consistent with phase-field predictions and reflect the influence of strain in favoring a tetragonal phase in  $\text{KNbO}_3$ . Furthermore, it is noteworthy that the rhombohedral phase which appears in bulk  $\text{KNbO}_3$  below 225 K is completely suppressed in all these films, even for the lowest strained sample on  $\text{GdScO}_3$ .

On the high-temperature end, the strain-stabilized tetragonal phase persists on heating up until 900 K for all three films, with no appreciable change in the measured SHG intensity. This suggests the robustness of the tetragonal phase. To test the highest operating temperature possible for the  $\text{KNbO}_3$  films, a  $\text{KNbO}_3$  film on  $\text{GdScO}_3$  was heated in air to temperatures higher than the film growth temperature ( $\approx 925$  K). The film shows signs of decomposition evidenced by the declining SHG intensity when heated beyond  $\approx 975$  K, while still maintaining a tetragonal symmetry that persists when cooled back down to room temperature (Figure S15, Supporting Information).

By benchmarking the SHG polarimetry to a reference sample, nonlinear optical coefficients are derived using the #SHAARP.m package,<sup>[30,31]</sup> and is discussed in further detail in Supporting Information. The measured  $d_{33}$  coefficient in strained tetragonal  $\text{KNbO}_3$  is shown in Figure 2d in reference to other similar ferroelectrics, reflecting a  $\approx 200\%$  enhancement of the  $d_{33}$  coefficient as compared to the bulk  $\text{KNbO}_3$  values while  $\approx 50\%$  higher than bulk  $\text{PbTiO}_3$  values.<sup>[32]</sup> Since at low temperatures, the films have multiple domains, extracting the full SHG tensor at low temperatures is challenging. From multi-domain modeling however, only a domain area-fraction scaled  $d_{11}d$  coefficient can be estimated which is  $\approx 44 \text{ pm V}^{-1}$  at 10 K. Since the domain area-fraction is strictly less than 1, this value should be considered only as a lower bound estimate of the low-temperature  $d_{11}$  coefficient, i.e.,  $d_{11} \geq 44 \text{ pm V}^{-1}$ .

#### 4. Structural Characterization by X-Ray Diffraction

To elucidate the structural phase transition to a lower symmetry phase upon cooling, the temperature-dependent out-of-plane lattice parameter was measured for the  $\text{KNbO}_3$  thin film grown on  $\text{GdScO}_3$ ; this is the film with the lowest strain ( $-1.1\%$ ). As shown in Figure 3a the  $\text{KNbO}_3$  film undergoes a change in its thermal expansion coefficient at 275 K, as extracted from the slope of lattice parameter variation versus temperature. This observation points to a film structure change that agrees with the SHG observations of the symmetry lowering at the same temperature of 275 K.

Additional 3D RSMs were obtained by synchrotron X-ray diffraction that shed more light on the nature of these observations. Diffraction images were collected with a large area detector with an incident X-ray photon energy of 50 keV, which allows sampling large reciprocal space volumes extending from 0

to  $6.5 \text{ \AA}^{-1}$  in the out-of-plane direction and from  $-5$  to  $5 \text{ \AA}^{-1}$  in the in-plane direction. In this configuration, the RSM measurements covered several peaks that are compared to each other to suggest a domain-averaged tetragonal structure for the  $\text{KNbO}_3$  film (Figure S16, Supporting information). Unfortunately, the symmetry of the film structure may remain hidden in the domain-averaged measurements. For this reason, the diffuse scattering patterns around selected peaks are more closely inspected that provide added information about the domain arrangements in the film. A  $213_c$  peak is chosen as a representative peak since this peak is sensitive to in-plane polarization components along both  $[100]$  or  $[010]$  directions. For the case of  $\text{KNbO}_3$  on  $\text{GdScO}_3$  at 400 K, the 2D RSM of the film peak around the  $213_c$   $\text{GdScO}_3$  peak (Figure 3b) shows film-substrate commensuration where additional diffuse scattering patterns near the film peak could not be observed. In the case of low-symmetry phases, we would have expected the formation of ferroelastic twins to generate diffuse scattering around the film position, whereas, in a tetragonal phase that is fully polarized out-of-plane as indicated by SHG measurements, the ferroelastic twin formation is not expected. Thus, X-ray measurements are consistent with the SHG measurements and the phase-field simulations in observing a tetragonal phase at  $>275$  K. When cooled down below the phase transition temperature, the  $\text{KNbO}_3$  film peaks develop diffuse scattering patterns nearby, which correspond to the formation of twins with an in-plane periodic arrangement. This reflects the symmetry lowering from the high-temperature tetragonal structure to a low-temperature monoclinic phase for the  $-1.1\%$  biaxially strained thin films, supporting the SHG observations. The tilt of the diffuse satellite peaks can be directly correlated to the tilt of the monoclinic domains themselves relative to the substrate.<sup>[33,34]</sup> Averaging over several peaks (Figure S17, Supporting Information), this tilt is measured to be  $17^\circ \pm 4^\circ$  away from the  $[110]$  in-plane direction toward the  $[001]$  out-of-plane direction, which agrees with the phase-field microstructure modeling of monoclinic domains at 100 K, which shows a similar tilt of  $\approx 19^\circ$  away from the  $[110]$  direction (Figure 3c, left and bottom panels). Diffraction simulation of the phase-field microstructure at 100 K (Figure 3d) also supports this expectation where diffuse satellites around the  $213_c$   $\text{KNbO}_3$  peak show the same tilt of  $\approx 19^\circ$ , emphasizing the connection between the tilt of the satellite peaks and the tilt of the domains themselves. The same tilt is similarly observed for diffraction simulations around several other peaks as well (Figure S17, Supporting Information) which considerably strengthens our claim. In comparison, diffraction simulation of the phase-field microstructure at 400 K (Figure 3d, right panel) shows diffuse scattering around the  $213_c$   $\text{KNbO}_3$  peak without any tilt, consistent with the formations of only tetragonal domain variants with polarization along the  $[001]$  or  $[00\bar{1}]$  directions with  $180^\circ$  domain walls between them. The experimentally measured RSM at 400 K does not show such diffuse scattering patterns around the film peak. This is due to the absence of  $180^\circ$  tetragonal domains in these films. Only the polarization direction pointing upwards from the substrate appears to be stable as confirmed by piezoresponse force microscopy measurements (Section 5 and Figure S23, Supporting Information). Additionally, the experimentally observed diffuse satellite peaks at 100 K correspond to an in-plane domain periodicity of  $\approx 27$  nm in agreement with the  $\approx 22$  nm periodicity predicted by phase field modeling.

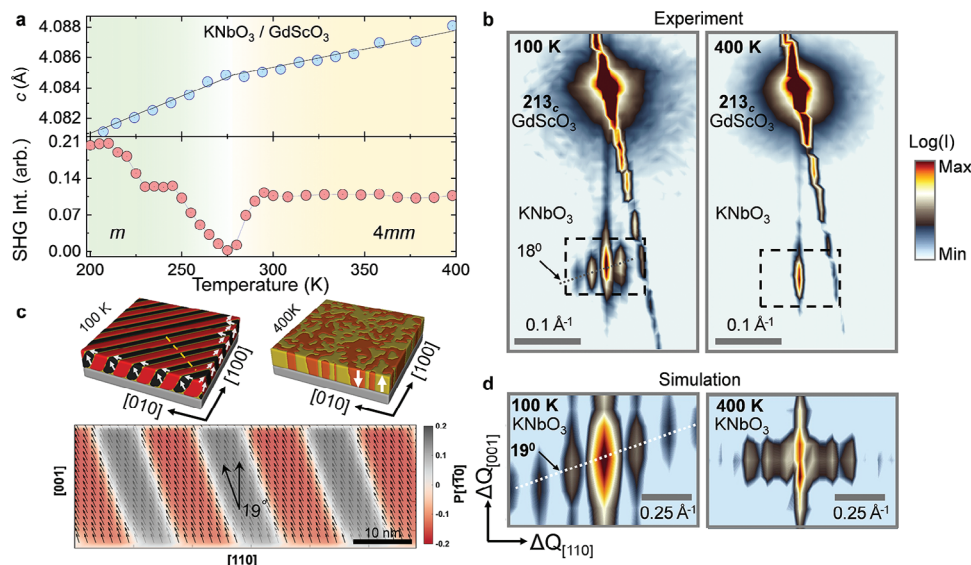


**Figure 3.** a) (Upper panel) Out-of-plane lattice parameter measured for the KNbO<sub>3</sub> film grown on a GdScO<sub>3</sub> substrate deduced from the position of the 002<sub>c</sub> specular peak between 200 K and 400 K, showing a change of the thermal expansion coefficient at 275 K. The phase transition temperature from the X-ray agrees with the SHG measurements (lower panel, zoomed in from Figure 2c). b) Synchrotron-based x-ray reciprocal space maps (RSM) at 400 K and 100 K for the KNbO<sub>3</sub> film grown on a GdScO<sub>3</sub> substrate around the 213<sub>c</sub> (*c* stands for cubic) substrate Bragg reflection (tetragonal to monoclinic phase transition found from SHG at 275 K). The strong diagonal streak passing through the substrate peak is an artifact due to the spreading of the signal on the area detector for high intensity and is oriented along the Ewald sphere. Both at 400 K and 100 K, the films are coherent to the substrate but at 100 K, the film peak develops diffuse satellite peaks which are attributed to the formation of periodic monoclinic twin domains. The satellite peaks are tilted away from the in-plane [110] direction toward the [001] direction by  $17^\circ \pm 4^\circ$  calculated by averaging over several peaks. The domains exhibit a 27 nm periodicity in the [110] direction extracted from the satellite peak separation. c) (left panel) Phase-field simulated microstructure at 100 K showing monoclinic domains consistent with the domain pattern experimentally observed (left panel of (b)). A vertical cut of this microstructure is shown in the bottom panel along the [110] direction (bottom panel) revealing a tilt of the domain by  $19^\circ$  similar to experimental observations (left panel of (b)). Predicted domain periodicity is measured to be  $\approx 22$  nm through phase field simulations matching the experimental observation ( $\approx 27$  nm). Phase field simulated microstructure at 400 K shows tetragonal domains with no in-plane periodic structures (right panel) consistent with right panel of (b). d) Diffraction simulation of the phase field microstructure at 100 K and 400 K around the 213<sub>c</sub> KNbO<sub>3</sub> peak (zoomed in to match q-vectors corresponding to dotted boxes in panel (b)) showing a  $19^\circ$  tilt in the diffuse satellites at 100 K matching experimental observations whereas no tilt is seen corresponding to the simulation at 400 K.

## 5. Ferroelectricity

To test the ferroelectric behavior of KNbO<sub>3</sub>, thin films were grown on SrTiO<sub>3</sub> and DyScO<sub>3</sub> substrates with a 15 nm thick SrRuO<sub>3</sub> bottom electrode layer. RHEED and RSMs were performed to confirm the crystallinity and commensurate strain nature of the films on the substrate (Figures S18 and S19, Supporting Information). Cross-sectional TEM of KNbO<sub>3</sub>/SrRuO<sub>3</sub>/SrTiO<sub>3</sub> films shows a uniform interface structure without any extended defects suggesting high-quality epitaxial growth (Figure S11, Supporting Information). Temperature-dependent SHG on KNbO<sub>3</sub> films with SrRuO<sub>3</sub> bottom electrode shows no effect of SrRuO<sub>3</sub> on the phase transition temperatures of the KNbO<sub>3</sub> films (Figure S20, Supporting Information).

Piezoresponse force microscopy (PFM) and electrical measurements of the switching current were performed on the Pt/KNbO<sub>3</sub>/SrRuO<sub>3</sub>/DyScO<sub>3</sub> capacitors with 21.8 nm thick KNbO<sub>3</sub>. Figure 4a shows a representative PFM switching spectroscopy loop obtained at an arbitrary location on the capacitor at a quasi-static frequency of 0.2 Hz, which exhibits standard ferroelectric  $d_{33}$ -*V* behavior with coercive voltages of  $-0.5$  and  $2.2$  V. The films appear to be self-poled in the as-grown state with a remanent polarization,  $P_r$ , pointing from the bottom to

the top of the film. When poled down by applying a bias using the PFM tip, the strong upward built-in field ( $\approx 0.8$  MV cm<sup>-1</sup>) causes the downward polarization to relax back to the upward state in seconds (Figures S21–S23, Supporting Information). *I*-*V* measurements (Figure 4b) at a frequency of 100 kHz from the capacitors show clear switching current peaks on the negative voltage side, while a high leakage current appears on the positive voltage side obscuring the switching current signal. Additional testing shows that the high leakage on the positive voltage side increases with time. In addition, it can also be seen in Figure 4b that the current for the voltage decreasing from 4 to 0 V is higher than that for the voltage increasing from 0 to 4 V. This leakage, which cannot be subtracted using a standard PUND (positive-up-negative-down) method,<sup>[35]</sup> prevents measurements of the switching current on the positive bias side. In contrast, the switching current can be measured on the negative bias side using the PUND method (Figure 4c). The extracted switching current peak shows a switching time for the  $5 \times 5$  μm<sup>2</sup> capacitors on the order of 80 ns and a  $P_r$  of  $\approx 38$  μC cm<sup>-2</sup>. Nonetheless, further investigation reveals that there is a dynamic leakage current during the polarization switching process that is not subtracted with the standard PUND method (Figure S22, Supporting Information), which suggests that the calculated polarization value is perhaps overestimated.<sup>[36,37]</sup> Polarization switching in KNbO<sub>3</sub>

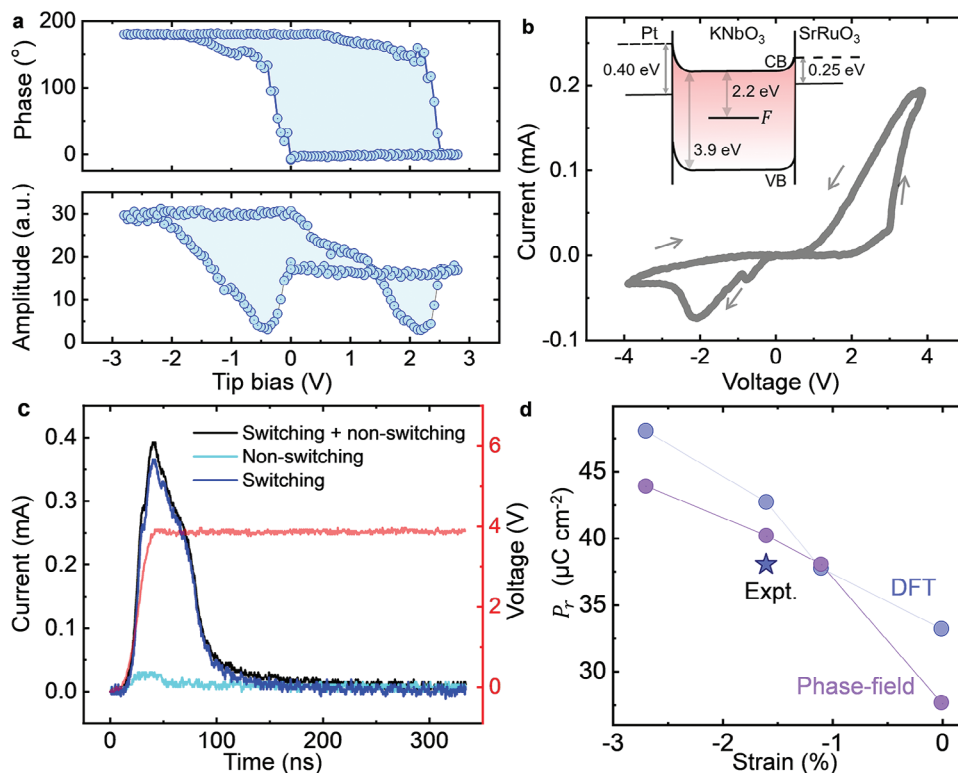


**Figure 4.** PFM switching spectroscopy and electrical measurements of the switching current on the  $5 \times 5 \mu\text{m}^2$  Pt/KNbO<sub>3</sub>/SrRuO<sub>3</sub>/DyScO<sub>3</sub> capacitors. a) PFM switching spectroscopy measured at an arbitrary location on the capacitor shows standard ferroelectric  $d_{33}$ -V behavior. b) I-V measurement shows switching current peaks on the negative voltage side, while high leakage current smears out the switching peak on the positive side. The inset shows a schematic band diagram of KNbO<sub>3</sub> depicting the measured Schottky barrier heights at both Pt-KNbO<sub>3</sub> and SrRuO<sub>3</sub>-KNbO<sub>3</sub> interfaces and the known F-center (Oxygen-vacancy which traps electrons) energy level in KNbO<sub>3</sub>.<sup>[43,44]</sup> c) PUND measurement of the switching peak at  $-4$  V shows a switching time in the order of 80 ns and a remnant polarization of  $\approx 38 \mu\text{C cm}^{-2}$ . d) Comparison of polarization versus strain predicted from phase-field simulations and DFT calculations along with experimentally observed value from PUND measurements. All values are for the tetragonal phase of KNbO<sub>3</sub>.

films on DyScO<sub>3</sub> and SrTiO<sub>3</sub> substrates with SrRuO<sub>3</sub> bottom electrode have also been confirmed with PFM measurements (Figure S21, Supporting Information), where the presence of the strong upward built-in fields causes the polarization down state to be very unstable, and the as-grown films are preferentially in the upward single domain states. Figure 4d shows a comparison of the measured  $P_r$  with predicted  $P_r$  values from phase field simulations and PBEsol calculations, indicating further room for the enhancement of the experimental  $P_r$ .

Our current PFM measurements on the Pt/KNbO<sub>3</sub>/SrRuO<sub>3</sub> capacitors show asymmetric leakage currents for opposite polarities. To understand the origin of the leakage current, temperature-dependent IV measurements under DC bias were performed on Pt/KNbO<sub>3</sub>/SrRuO<sub>3</sub>/SrTiO<sub>3</sub> capacitors. The IV measurements can be fitted to a Schottky emission model (Figures S24 and S25, Supporting Information), suggesting electrode-film interface-controlled Schottky emission to be one of the dominant contributors of leakage in KNbO<sub>3</sub> films. The estimated Schottky barrier height is  $0.4 \pm 0.04$  eV for the Pt/KNbO<sub>3</sub> interface and  $0.25 \pm 0.03$  eV for the SrRuO<sub>3</sub>/KNbO<sub>3</sub> interface. The asymmetric Schottky barrier height is responsible for the asymmetric leakage current and is due to the different work functions of Pt (5.6 eV<sup>[38]</sup>) and SrRuO<sub>3</sub> (5.2 eV<sup>[39]</sup>) electrodes and different interface chemistry at each interface (Figure 4b).

To further explore the dielectric response and additional charge transport mechanisms in the KNbO<sub>3</sub> film, temperature, and frequency-dependent modulus spectroscopy measurements were performed. The frequency-dependent imaginary part of the electric modulus shows a dielectric relaxation peak with a corresponding Arrhenius activation energy of  $0.45 \pm 0.04$  eV (Figure S27, Supporting Information). We hypothesize that this relaxation process is related to the polaron hopping mechanism which has previously been observed in KNbO<sub>3</sub> single crystals.<sup>[40,41]</sup> Due to high K vapor pressure, K vacancies are common in KNbO<sub>3</sub>, which subsequently leads to oxygen vacancies. Since these oxygen vacancies are necessary for charge neutrality, they are thermodynamically stable and cannot be removed via an annealing process. Oxygen vacancies can also be formed due to oxygen leaving lattice positions serving as electron donor defects leading to carrier injection in KNbO<sub>3</sub>.<sup>[42]</sup> Oxygen vacancies can contribute to both electronic and ionic conductivity in KNbO<sub>3</sub> films. Oxygen vacancies in KNbO<sub>3</sub> can also serve as electron trapping sites (F-center) which produces deep energy levels,  $\approx 2.2$  eV below the conduction band.<sup>[43,44]</sup> Finally, migration of K<sup>+</sup> ions and oxygen vacancies (activation energies of 0.6 and 1.2 eV respectively)<sup>[45]</sup> and the formation of conductive domain walls and pinholes across a thin film can also contribute to leakage in KNbO<sub>3</sub> thin films.

Our present investigations in strain-tuned KNbO<sub>3</sub> films present a unique opportunity in KNbO<sub>3</sub> where strain can not only be employed to enhance ferroelectric properties in KNbO<sub>3</sub> but also these properties can be accessed stably across a wide temperature range of operation by pushing out phase transitions which would otherwise lead to divergence of ferroelectric properties. Though further work is necessary to understand the nature and role of intrinsic defects in KNbO<sub>3</sub> thin films, SHG experiments show the robustness of KNbO<sub>3</sub> films at high temperatures ranging up to ≈975 K. Notably, surface capping of KNbO<sub>3</sub>, the development of KNbO<sub>3</sub>-based superlattice heterostructures, and slightly doping the film with electron acceptors would not only further enhance the stability of KNbO<sub>3</sub> from the formation of intrinsic K and O vacancy point defects, but also would allow the growth of thicker coherently strained films avoiding mechanical sources of leakage like pinhole formations.

## 6. Conclusion

In summary, our experiments and simulations demonstrate that biaxially strained KNbO<sub>3</sub> films result in the stabilization of a single tetragonal phase throughout the entire temperature range from 10 K to 975 K in contrast to four competing phases observed in bulk single crystals; this is challenging to achieve in other competing Pb-free ferroelectrics such as BaTiO<sub>3</sub> and Na<sub>x</sub>K<sub>1-x</sub>NbO<sub>3</sub>. Concomitantly, a large enhancement in the tetragonality through strain is observed with its *c/a* ratio reaching values that exceed even those of bulk PbTiO<sub>3</sub>. A ≈200% increase in the tetragonal phase optical second harmonic generation coefficients over bulk single crystal values is observed. A dramatic *T<sub>c</sub>* enhancement well beyond its decomposition and melting temperatures are seen with a 3 × higher tunability,  $\frac{dT_c}{de}$ , as compared to all other strain-tuned perovskite oxides. A broad design trend gleaned from this study is that for tetragonal perovskite ferroelectrics, a high *T<sub>c</sub>* is achieved by maximizing electrostriction and minimizing elastic compliance (Figure S3, Supporting information). Importantly, there are optimal values of electrostriction and compliance that maximize *P<sub>r</sub>*. For KNbO<sub>3</sub>, its superior electrostriction and low elastic stiffness coefficients compared to similar materials result in a large and highly strain-tunable *T<sub>c</sub>* in addition to a competitive magnitude and tunability in *P<sub>r</sub>*. All these observations render strained KNbO<sub>3</sub> thin films as a strong, thermally stable lead-free ferroelectric with a large operating temperature regime suitable for a wide range of applications.

## 7. Experimental Section

**Thin Film Synthesis and Characterization:** Epitaxial thin films of KNbO<sub>3</sub> were grown using a Veeco Gen 10 MBE system. A molecular beam of NbO<sub>2</sub> (gas) flux was generated from an effusion cell containing Nb<sub>2</sub>O<sub>5</sub> (H.C. Stark 99.99%) contained in an iridium crucible. NbO<sub>2</sub> is the most volatile species in the growth temperature range.<sup>[46]</sup> Potassium was evaporated from an effusion cell containing an indium-rich (≈4:1 In:K ratio) mixture of potassium and indium so it forms the air-stable intermetallic In<sub>4</sub>K.<sup>[47]</sup> The K-In alloy was prepared in a glove box and contained in a titanium crucible. Once prepared, it can be exposed to air, facilitating its handling and loading. The vapor pressure of potassium was more than 10<sup>10</sup> times higher than indium at the K-In cell temperature of 300–400 °C.<sup>[48]</sup> GdScO<sub>3</sub> (110)<sub>o</sub>, and DyScO<sub>3</sub> (110)<sub>o</sub> (Crystec GmbH) substrates were used as re-

ceived and the SrTiO<sub>3</sub> (001) substrates were terminated following the procedure developed by Koster.<sup>[49]</sup>

Films were grown by co-deposition of potassium, niobium, and ozone at a substrate temperature of 700–650 °C as measured by an optical pyrometer operating at a wavelength of 1550 nm. The pyrometer measures the temperature of the platinum coating that had been evaporated on the backside of the substrate to facilitate radiative heat transfer from the SiC heating element of the MBE system to the substrate. The K:Nb flux ratio was kept at ≈10:1. A mixture of ozone and oxygen (10% O<sub>3</sub> + 90% O<sub>2</sub>) was used as the oxidant. The films were grown at an oxidant background pressure of 1 × 10<sup>-6</sup> Torr. Typical fluxes for the sources were (1–2) × 10<sup>13</sup> atoms cm<sup>-2</sup> s<sup>-1</sup> for NbO<sub>2</sub> and (1–4) × 10<sup>14</sup> atoms cm<sup>-2</sup> s<sup>-1</sup> for potassium, determined by a quartz crystal microbalance (QCM), with an accuracy of ≈15%. In a typical growth experiment, the potassium flux was measured first, followed by NbO<sub>2</sub> to ensure that the QCM was as close to room temperature as possible for the most accurate reading. For a more detailed description, the reader was referred to an identical procedure reported for KTaO<sub>3</sub>.<sup>[50]</sup> Co-deposition with these fluxes results in a KNbO<sub>3</sub> film growth rate of ≈0.3 Å s<sup>-1</sup>.

X-ray diffraction (XRD), X-ray reflectometry (XRR), and RSM measurements were carried out using a PANalytical Empyrean diffractometer with Cu Kα<sub>1</sub> radiation. The raw XRR spectra were analyzed using the PANalytical X'Pert Reflectivity software package and the layer thickness was derived from a fast Fourier transform (FFT) after manually defining the critical angle to account for refractive effects. In situ reflection high-energy electron diffraction (RHEED) patterns were recorded using KSA-400 software and a Staib electron source operated at 14 kV and a filament current of 1.5 A. The morphology of the film surface was characterized using an Asylum Cypher ES environmental AFM.

**Transmission Electron Microscopy:** The cross-sectional samples for scanning transmission electron microscopy (STEM) were prepared using a standard focused ion beam lift-out process. The KNbO<sub>3</sub> thin film on the SrTiO<sub>3</sub> substrate was milled using the FEI Helios NanoLab 600 DualBeam, while the samples on GdScO<sub>3</sub> and DyScO<sub>3</sub> substrates were milled using the Helios G4 UX DualBeam system. All samples were initially thinned with 5 kV Ga ions and then polished at 2 kV to minimize surface damage. HAADF-STEM images of KNbO<sub>3</sub> samples on GdScO<sub>3</sub> and DyScO<sub>3</sub> were obtained using the Spectra 300 X-CFEG microscope with a 60–200 mrad HAADF detector. For the KNbO<sub>3</sub> film on SrTiO<sub>3</sub>, the Thermo Scientific Themis Z S/TEM with a 64–200 mrad HAADF detector was used. Both microscopes operated at 200 kV with a semi-convergence angle of 30 mrad. To improve the signal-to-noise ratio, HAADF-STEM images were captured as a series of 20 fast scan images (2048 × 2048 pixels, 200 ns per frame) and then averaged them. STEM energy-dispersive X-ray (EDX) spectroscopy data for films on GdScO<sub>3</sub> and DyScO<sub>3</sub> were collected using a steradian Dual-X EDX detector. The resulting spectrum was then denoised using principal component analysis.

**Second Harmonic Generation (SHG) Measurement:** SHG polarimetry and temperature-dependent measurements were done with femtosecond pulses at λ = 800 nm fundamental light from a regeneratively amplified Spectra-Physics Solstice Ace Ti:Sapphire laser system (1kHz, 100 fs). The schematic of the setup is shown in Figure 2a. Linearly polarized light incident on the sample at an incidence angle θ generate second harmonic light at λ = 400 nm. The *p*-polarized and *s*-polarized SHG intensities were spectrally filtered and measured by a photomultiplier tube through lock-in amplifier (SR830) detection. Polar plots were generated by rotating the polarization angle (φ) of the incident fundamental light by a half-wave plate. Temperature-dependent measurements were done through a Janis 300 gas flow cryostat for low-temperature and a home-built heating stage for high-temperature experiments.

**Synchrotron-Based Reciprocal Space Mapping:** Synchrotron x-ray diffraction experiments were performed on the ID4B (QM2) beamline at the Cornell high energy synchrotron source (CHESS). The incident X-ray energy was 50 keV (λ = 0.247 Å), which was selected using a double-bounce diamond monochromator. An area detector array (Pilatus 6M) was used to collect the scattering intensities in a reflection geometry. The sample was rotated with a 1° tilt through 180° rotations, sliced into 0.1° frames. Geometric parameters of the Pilatus 6M detector such

as detector distance, tilting, rotation, and direct beam position were extracted using standard CeO<sub>2</sub> powder. The uncertainty in temperature was <10 K.

**X-Ray Photoelectron Spectroscopy:** The XPS experiment was performed using the Physical Electronics VersaProbe III instrument with a monochromatic Al K $\alpha$  x-ray source ( $h\nu = 1486.6$  eV) and a concentric hemispherical analyzer. Charge neutralization was performed using low-energy electrons (<5 eV) and argon ions. The binding energy axis was calibrated using sputter-cleaned Cu (Cu 2p<sub>3/2</sub> = 932.62 eV, Cu 3p<sub>3/2</sub> = 75.1 eV) and Au foils (Au 4f<sub>7/2</sub> = 83.96 eV). Measurements were made at a takeoff angle of 45° with respect to the sample surface plane. This resulted in a typical sampling depth of 3–6 nm. On homogeneous samples, major elements (>5 atom%) tend to have standard deviations of <3%, while minor elements can be significantly higher. The analysis size was 200  $\mu\text{m}$  in diameter.

**PFM Spectroscopy Measurements:** The PFM switching spectroscopy data were measured using an atomic force microscopy system (MFP3D, Asylum Research) with Pt-coated tips (PPP-EFM, Nanosensors) in the resonance enhanced mode (DART) with AC-modulation voltage of 0.2 V at 340 kHz. DC voltage was applied to the top electrodes in the pulsed mode, where the pulse-on period is for polarization switching and the pulse-off period is for PFM signal detection.

**Pt Top Electrodes Deposition:** The Pt top electrodes with a thickness of  $\approx 15$  nm were deposited ex situ by pulsed laser deposition (PLD) in vacuum at room temperature.  $5 \times 5 \mu\text{m}^2$  electrode patterns were prepared using a standard liftoff approach with a laser lithography system (Heidelberg DWL 66FS).

**PUND and I–V Measurements:** A function generator (Keysight 33621A) was used for voltage pulse generation, and an oscilloscope (Tektronix TDS 3014B) was used for recording the switching current signal. Standard triangular waves at 100 kHz were used for the I–V measurements, and square pulses of 500 ns in width with one negative pulse followed by two positive and then two negative pulses were used for the PUND measurements (see Figure S17, Supporting Information). The pulse rise time is  $\approx 20$  ns. All voltages were applied to the top electrodes through the PFM tip.

**Leakage Current and Modulus Spectroscopy Measurements:** To investigate the dominant conduction mechanisms responsible for the rise in leakage current in KNbO<sub>3</sub> films, leakage current measurements were performed on 21.8 nm thick KNbO<sub>3</sub> films grown on DyScO<sub>3</sub> with a 15 nm thick SrRuO<sub>3</sub> bottom electrode, using a 4140 Pico-Ampere Meter/DC Voltage Source (Hewlett Packard). 100 nm thick Pt electrodes which were lithographically patterned into 50  $\mu\text{m} \times 50 \mu\text{m}$  squares, were used as the top electrode.

To further explore additional charge transport mechanisms in the KNbO<sub>3</sub> film, temperature-dependent modulus spectroscopy measurements were performed using a Solartron 1260 Impedance analyzer with a 100 mV AC amplitude, over a frequency range from 1 MHz to 0.01 Hz.

**Phase-Field Modeling:** Using the phase field method, the evolution of the ferroelectric polarization ( $P_i$ ) was governed by the time-dependent Ginzburg Landau equation:

$$\gamma_{ij} \frac{\partial P_j(x_i, t)}{\partial t} = \frac{\delta F}{\delta P_i(x_i, t)} \quad (2)$$

where  $\gamma_{ij}$  is the kinetic coefficient tensor which is chosen to be isotropic and  $F$  is the total free energy of the system which is the integral of all energy density components:

$$F = \iiint_V \left[ f_{\text{Landau}}(P_i) + f_{\text{grad}}(\nabla P_i) + f_{\text{elas}}(P_i, \epsilon_{ij}) + f_{\text{elec}}(P_i, E_i) \right] dV \quad (3)$$

where  $f_{\text{Landau}}$ ,  $f_{\text{grad}}$ ,  $f_{\text{elas}}$  and  $f_{\text{elec}}$  denote the Landau free-energy density, the gradient energy density, the elastic energy density, and the electrostatic energy density respectively, and  $V$  is the volume of the system.

The Landau free energy density describes the intrinsic stability of the ferroelectric phases compared to the high symmetry phase ( $m\bar{3}m$ ) as a

Taylor expansion of the polarization about the high symmetry phase:

$$\begin{aligned} f_{\text{Landau}}(P_i) = & \alpha_1 (T) (P_1^2 + P_2^2 + P_3^2) + \alpha_{11} (P_1^4 + P_2^4 + P_3^4) \\ & + \alpha_{12} (P_1^2 P_2^2 + P_1^2 P_3^2 + P_2^2 P_3^2) + \alpha_{111} (P_1^6 + P_2^6 + P_3^6) \\ & + \alpha_{112} (P_1^4 (P_2^2 + P_3^2) + P_2^4 (P_1^2 + P_3^2) + P_3^4 (P_1^2 + P_2^2)) \\ & + \alpha_{123} P_1^2 P_2^2 P_3^2 + \alpha_{1111} (P_1^8 + P_2^8 + P_3^8) + \alpha_{1112} (P_1^6 (P_2^2 + P_3^2) \\ & + P_2^6 (P_1^2 + P_3^2) + P_3^6 (P_1^2 + P_2^2)) \\ & + \alpha_{1122} (P_1^4 P_2^4 + P_2^4 P_3^4 + P_3^4 P_1^4) \\ & + \alpha_{1123} (P_1^4 P_2^2 P_3^2 + P_1^2 P_2^4 P_3^2 + P_1^2 P_2^2 P_3^4) \end{aligned} \quad (4)$$

The Landau expansion coefficients were adjusted from the work of Liang<sup>[11]</sup> to fit with experimentally measured polarization and dielectric properties.<sup>[51–53]</sup> The revised set of coefficients is listed under Table S1 in Section S1 (Supporting Information).

The gradient energy density is represented by:

$$f_{\text{grad}} = \frac{1}{2} G_{ijkl} \frac{\partial P_i}{\partial x_j} \frac{\partial P_k}{\partial x_l} \quad (5)$$

where  $G_{ijkl}$  is the gradient energy tensor where the non-zero coefficients are chosen to be  $G_{11} = 0.6$ ,  $G_{22} = -0.6$  and  $G_{44} = 0.6$  and the units are normalized by  $\alpha_1 l_0^2$  where  $\alpha_1$  is the first Landau expansion coefficient and  $l_0$  is chosen as 1 nm per grid.

The elastic energy density is calculated as:

$$f_{\text{elas}}(P_i, \epsilon_{ij}) = \frac{1}{2} c_{ijkl} (\epsilon_{ij} - \epsilon_{ij}^o) (\epsilon_{kl} - \epsilon_{kl}^o) \quad (6)$$

where  $c_{ijkl}$  represents the stiffness tensor,  $\epsilon_{ij}$  is the total strain using the parent cubic phase as a reference, and  $\epsilon_{ij}^o$  is the eigenstrain which is dictated by the ferroelectric polarization and the electrostrictive tensor  $Q_{ijkl}$  as:

$$\epsilon_{ij}^o = Q_{ijkl} P_k P_l \quad (7)$$

The elastic constant tensor components and electrostrictive coefficients used in this work are listed in Table S2 in Section S1 (Supporting Information).

The electrostatic energy density can be expressed as:

$$f_{\text{elec}}(P_i, E_i) = -E_i P_i - \frac{1}{2} \epsilon_o \kappa_{ij} E_i E_j \quad (8)$$

where  $E_i$  is the component of the electric field,  $\epsilon_o$  is the dielectric permittivity of vacuum and  $\kappa_{ij}$  is the background dielectric susceptibility which accounts for the contributions to the total dielectric susceptibility beyond the ferroelectric soft mode following the work of Tagentsev.<sup>[54]</sup>

The evaluation of the elastic and electrostatic energy contributions in the phase-field method could be found in the existing literature.<sup>[55–57]</sup> At each time step, the electrical and mechanical equilibrium equations were solved under short-circuit and thin-film boundary conditions respectively.

For the simulations, a spatially discretized system of  $128\Delta x \times 128\Delta y \times 36\Delta z$  grids was employed with a grid spacing  $\Delta x = \Delta y = \Delta z = 1$  nm. The film thickness was set to  $20\Delta x$ , and the substrate was  $10\Delta x$ , with a  $4\Delta x$  layer of air above the film. The in-plane strains  $\epsilon_{11}$  and  $\epsilon_{22}$  were set equal to the misfit strains imposed by the lattice mismatch with the substrate. An initial random polarization distribution with a small magnitude of fluctuations of  $\Delta P = 0.1 \text{ Cm}^{-2}$  was started and let the system evolve to equilibrium.

The details on the construction of the phase diagram are provided in Note S1 (Supporting Information).

**Diffraction Simulation:** The diffraction intensity ( $I$ ) was calculated at the reciprocal space position  $\mathbf{q}$  from:

$$I(\mathbf{q}) = |F(\mathbf{q})|^2 \quad (9)$$

where  $F$  is the structure factor obtained by:

$$F(\mathbf{q}) = \sum_{m,n} f_n e^{-i\mathbf{q}\cdot\mathbf{r}_{m,n}} \quad (10)$$

where  $m$  is the unit cell index,  $n$  is the index of the atoms within the unit cell, and  $f_n$  is the atomic form factor of the  $n$ -th atom which is comprised of a real and imaginary part:

$$f_n = f_n^1 + if_n^2 \quad (11)$$

The atomic form factors for the constituent atoms were obtained from the tabulated atomic data,<sup>[58]</sup> assuming a photon energy of 10 KeV. The position of each atom ( $\mathbf{r}_{m,n}$ ) was calculated assuming a linear dependence of the atomic positions upon the polar order, i.e.,:

$$\mathbf{r}_{m,n} = \mathbf{R}_{m,n} + \mathbf{s}_n P_m \quad (12)$$

where  $\mathbf{R}_{m,n}$  is the reference position in the absence of a polarization and  $\mathbf{s}_n$  are atomic site-specific displacement coefficients relating the polarization to the atomic displacement. Atomic form factors and site-specific displacement coefficients are given in Table S4 (Supporting Information).

**Density Functional Theory:** The different phases were structurally optimized in the framework of density-functional theory (DFT) with the open-source software ABINIT.<sup>[59–61]</sup> A plane-wave basis set with a kinetic energy cutoff of 49 Ha was used to expand the wavefunctions. Optimized norm-conserving Vanderbilt pseudopotentials from the PseudoDojo<sup>[62,63]</sup> (v0.4.1) were adopted and the exchange-correlation energy was modeled using the Perdew–Burke–Ernzerhof generalized-gradient approximation modified for solids (GGA-PBESol).<sup>[64,65]</sup> The Brillouin zone was sampled with a Monkhorst–Pack<sup>[66,67]</sup>  $8 \times 8 \times 8$  k-point mesh and the self-consistent field cycles were converged until the residual on the potential reached  $10^{-12}$ . The structures were relaxed until a maximum force of  $2.5 \text{ meV } \text{Å}^{-1}$  on each atom was reached. The local-density approximation<sup>[68]</sup> and the GGA-PBE exchange correlation were also tested, but the PBESol functional resulted in the best  $c/a$  ratio for the tetragonal and orthorhombic phases. For each phase, the in-plane lattice parameters were fixed while the out-of-plane lattice parameter and the internal atomic positions were allowed to relax. For the monoclinic phase, since it presents too many degrees of freedom to adopt the same methodology, the in-plane lattice parameters were set to the average values obtained by the phase-field simulations at 25K for the two strains corresponding to the  $\text{GdScO}_3$  and  $\text{DyScO}_3$  substrates.

The polarization was computed with the Vienna ab initio simulation package (VASP v6.3.0).<sup>[69–72]</sup> The exchange-correlation energy was modeled with the GGA-PBE and the projector augmented wave method (PAW) method was used.<sup>[73]</sup> The wavefunctions were expanded on a plane-wave basis set with a kinetic energy cutoff of 680 eV. A  $6 \times 6 \times 6$   $\Gamma$ -centered k-point mesh was adopted to sample the Brillouin zone, and the total energy was converged to  $1 \text{ } \mu\text{eV}$  in the electronic self-consistent loops. The polarization calculations were automated with the atomate2 python package.<sup>[74]</sup>

## Supporting Information

Supporting Information is available from the Wiley Online Library or from the author.

## Acknowledgements

S.H. and T.S. contributed equally to this work. S.H., A.M., J.W.F., A.M.L., V.A.S., and V.G. acknowledge support from the DOE-BES grant DE-

SC0012375 for thin film growth efforts (S.H.), optical SHG experiments (S.H., V.G.), x-ray characterization (S.H., A.M., J.W.F., V.A.S., V.G.), and manuscript preparation. This work made use of the synthesis and electron microscopy facilities of the Platform for the Accelerated Realization, Analysis, and Discovery of Interface Materials (PARADIM), which are supported by the National Science Foundation under Cooperative Agreement No. DMR-2039380. TS, MRB, DAM, and DGS, also acknowledge the support of the National Science Foundation under Cooperative Agreement No. DMR-2039380. A.R., U.S., T.K., R.E.H., L.Q.C., and V.G. acknowledge support from the U.S. Department of Energy, Office of Science, Office of Basic Energy Sciences, under Contract No. DE-SC0020145 for the phase-field simulations (A.R., U.S., L.Q.C.) and part of the growth efforts (T.K., R.E.H. and V.G.). A.R. also acknowledges the support of the National Science Foundation Graduate Research Fellowship Program under Grant No. DGE1255832. The phase-field simulations in this work were performed using Bridges-2 at the Pittsburgh Supercomputing Center through allocation MAT230041 from the ACCESS program, which is supported by National Science Foundation grants #2138259, #2138286, #2138307, #2137603 and #2138296. The PFM studies at UNL have been supported by the UNL Grand Challenges catalyst award “Quantum Approaches addressing Global Threats”. B.Z.G. and A.S. acknowledge support for the generation of 3D reciprocal space maps from the U.S. Department of Energy, Office of Science, Office of Basic Energy Sciences, under Contract No. DE-SC0019414. V.T. acknowledges the support from the FRS-FNRS through an FRIA Grant. Computational resources have been provided by the supercomputing facilities of the Université Catholique de Louvain (CISM/UCL) and the Consortium des Équipements de Calcul Intensif en Fédération Wallonie Bruxelles (CÉCI) funded by the Fond de la Recherche Scientifique de Belgique (F.R.S.-FNRS) under convention 2.5020.11 and by the Walloon Region. The present research benefited from computational resources made available on Lucia, the Tier-1 supercomputer of the Walloon Region, infrastructure funded by the Walloon Region under grant agreement No. 1910247. Research conducted at the Center for High-Energy X-ray Science (CHEXS) was supported by the National Science Foundation (BIO, ENG, and MPS Directorates) under award DMR-1829070. X.L. and X.X. acknowledge the support of Intel. This work made use of a Helios FIB supported by NSF (grant no. DMR-1539918) and the Cornell Center for Materials Research (CCMR) Shared Facilities, which were supported through the NSF MRSEC Program (grant no. DMR-1719875). The Thermo Fisher Spectra 300 X-CFEG was acquired with support from PARADIM (NSF MIP DMR-2039380) and Cornell University. Part of the Electron microscopy experiment was performed at the Center for Electron Microscopy and Analysis (CEMAS) at The Ohio State University. S.S. and V.G. acknowledge support from National Science Foundation grant number NSF DMR-2210933 for optical SHG characterization. For electrical leakage measurements, the authors acknowledge the Center for 3D Ferroelectric Microelectronics (3DFeM), an Energy Frontier Research Center funded by the U.S. Department of Energy (DOE), Office of Science, Basic Energy Sciences, under Award No. DE-SC0021118. [Correction added on November 19, 2024, after first online publication: Data Availability Section has been updated.]

## Conflict of Interest

The authors declare no conflict of interest.

## Data Availability Statement

The data that support the findings of this study are available within the article. Additional data related to the film growth and structural characterization by XRD and STEM are available at <https://doi.org/10.34863/fs5e-s772>. Any additional data connected to the study are available from the corresponding author upon reasonable request.

## Keywords

ferroelectrics, phase-field modeling, second harmonic generation, strain-tuning, thin films

Received: June 18, 2024  
Revised: October 24, 2024  
Published online: November 12, 2024

- [1] D. G. Schlom, L.-Q. Chen, C.-B. Eom, K. M. Rabe, S. K. Streiffer, J.-M. Triscone, *Annu. Rev. Mater. Res.* **2007**, *37*, 589.
- [2] K. J. Choi, M. Biegalski, Y. L. Li, A. Sharan, J. Schubert, R. Uecker, P. Reiche, Y. B. Chen, X. Q. Pan, V. Gopalan, L.-Q. Chen, D. G. Schlom, C. B. Eom, *Science* **2004**, *306*, 1005.
- [3] R. Xu, J. Huang, E. S. Barnard, S. S. Hong, P. Singh, E. K. Wong, T. Jansen, V. Harbola, J. Xiao, B. Y. Wang, S. Crossley, D. Lu, S. Liu, H. Y. Hwang, *Nat. Commun.* **2020**, *11*, 3141.
- [4] J. H. Haeni, P. Irvin, W. Chang, R. Uecker, P. Reiche, Y. L. Li, S. Choudhury, W. Tian, M. E. Hawley, B. Craigo, A. K. Tagantsev, X. Q. Pan, S. K. Streiffer, L. Q. Chen, S. W. Kirchoefer, J. Levy, D. G. Schlom, *Nature* **2004**, *430*, 758.
- [5] J. H. Lee, L. Fang, E. Vlahos, X. Ke, Y. W. Jung, L. F. Kourkoutis, J.-W. Kim, P. J. Ryan, T. Heeg, M. Roeckerath, V. Goian, M. Bernhagen, R. Uecker, P. C. Hammel, K. M. Rabe, S. Kamba, J. Schubert, J. W. Freeland, D. A. Muller, C. J. Fennie, P. Schiffer, V. Gopalan, E. Johnston-Halperin, D. G. Schlom, *Nature* **2010**, *466*, 954.
- [6] J. Wang, J. B. Neaton, H. Zheng, V. Nagarajan, S. B. Ogale, B. Liu, D. Viehland, V. Vaithyanathan, D. G. Schlom, U. V. Waghmare, N. A. Spaldin, K. M. Rabe, M. Wuttig, R. Ramesh, *Science* **2003**, *299*, 1719.
- [7] R. J. Zeches, M. D. Rossell, J. X. Zhang, A. J. Hatt, Q. He, C.-H. Yang, A. Kumar, C. H. Wang, A. Melville, C. Adamo, G. Sheng, Y.-H. Chu, J. F. Ihlefeld, R. Erni, C. Ederer, V. Gopalan, L. Q. Chen, D. G. Schlom, N. A. Spaldin, L. W. Martin, R. Ramesh, *Science* **2009**, *326*, 977.
- [8] F. Eltes, G. E. Villareal-Garcia, D. Caimi, H. Siegwart, A. A. Gentile, A. Hart, P. Stark, G. D. Marshall, M. G. Thompson, J. Barreto, J. Fompeyrine, S. Abel, *Nat. Mater.* **2020**, *19*, 1164.
- [9] V. S. Puli, A. Jayakrishnan, D. K. Pradhan, K. Madgula, S. N. Babu, D. B. Chrisey, R. S. Katiyar, A. Reed, M. McConney, T. Back, R. M. Van Ginhoven, S. Heidger, *Energy Storage* **2023**, *5*, e359.
- [10] H. Zhang, T. Wei, Q. Zhang, W. Ma, P. Fan, D. Salamon, S.-T. Zhang, B. Nan, H. Tan, Z.-G. Ye, *J. Mater. Chem. C Mater.* **2020**, *8*, 16648.
- [11] L. Liang, Y. L. Li, L.-Q. Chen, S. Y. Hu, G.-H. Lu, *J. Appl. Phys.* **2009**, *106*, 104118.
- [12] K. Yamanouchi, H. Odagawa, T. Kojima, T. Matsumura, *Electron. Lett.* **1997**, *33*, 193.
- [13] K. Nakamura, T. Tokiwa, Y. Kawamura, *J. Appl. Phys.* **2002**, *91*, 9272.
- [14] T. T. A. Lummen, J. Leung, A. Kumar, X. Wu, Y. Ren, B. K. VanLeeuwen, R. C. Haislmaier, M. Holt, K. Lai, S. V. Kalinin, V. Gopalan, *Adv. Mater.* **2017**, *29*, 1700530.
- [15] L. Bogula, L. von Helden, C. Richter, M. Hanke, J. Schwarzkopf, M. Schmidbauer, *Nano Futures* **2020**, *4*, 035005.
- [16] L. von Helden, L. Bogula, P.-E. Janolin, M. Hanke, T. Breuer, M. Schmidbauer, S. Ganschow, J. Schwarzkopf, *Appl. Phys. Lett.* **2019**, *114*, 232905.
- [17] M. Schmidbauer, D. Braun, T. Markurt, M. Hanke, J. Schwarzkopf, *Nanotechnology* **2017**, *28*, 24LT02.
- [18] M. Adachi, Y. Akishige, T. Asahi, K. Deguchi, K. Gesi, K. Hasebe, T. Hikita, T. Ikeda, Y. Iwata, M. Komukae, T. Mitsui, E. Nakamura, N. Nakatani, M. Okuyama, T. Osaka, A. Sakai, E. Sawaguchi, Y. Shiozaki, T. Takenaka, K. Toyoda, T. Tsukamoto, T. Yagi, in *Oxides*, Springer Nature, Berlin, Germany **2001**, pp. 1–20.
- [19] V. Gopalan, R. Raj, *Appl. Phys. Lett.* **1996**, *68*, 1323.
- [20] V. Gopalan, R. Raj, *J. Am. Ceram. Soc.* **1995**, *78*, 1825.
- [21] V. Gopalan, R. Raj, *J. Appl. Phys.* **1997**, *81*, 865.
- [22] Y. Luo, Z. Wang, Y. Chen, M. Qin, Z. Fan, M. Zeng, G. Zhou, X. Lu, X. Gao, D. Chen, J.-M. Liu, *ACS Appl. Mater. Interfaces* **2023**, *15*, 16902.
- [23] M. V. Romanov, I. E. Korsakov, A. R. Kaul, S. Y. Stefanovich, I. A. Bolshakov, G. Wahl, *Chem. Vap. Deposition* **2004**, *10*, 318.
- [24] T. Saito, T. Wada, H. Adachi, I. Kanno, *Jpn. J. Appl. Phys.* **2004**, *43*, 6627.
- [25] T.-H. Lee, H.-G. Hwang, J.-U. Woo, D.-H. Kim, T.-W. Kim, S. Nahm, *ACS Appl. Mater. Interfaces* **2018**, *10*, 25673.
- [26] T.-H. Lee, D.-H. Kim, B.-Y. Kim, H.-Y. Choi, J.-H. Oh, C.-Y. Kang, S. Nahm, *Acta Mater.* **2016**, *112*, 53.
- [27] C. Ederer, N. A. Spaldin, *Phys. Rev. Lett.* **2005**, *95*, 257601.
- [28] N. A. Pertsev, V. G. Kukhar, H. Kohlstedt, R. Waser, *Phys. Rev. B* **2003**, *67*, 054107.
- [29] S. A. Denev, T. T. A. Lummen, E. Barnes, A. Kumar, V. Gopalan, *J. Am. Ceram. Soc.* **2011**, *94*, 2699.
- [30] R. Zu, B. Wang, J. He, J.-J. Wang, L. Weber, L.-Q. Chen, V. Gopalan, *npj Comput. Mater.* **2022**, *8*, 246.
- [31] R. Zu, B. Wang, J. He, L. Weber, A. Saha, L.-Q. Chen, V. Gopalan, *npj Comput. Mater.* **2024**, *10*, 64.
- [32] S. Singh, J. P. Remeika, J. R. Potopowicz, *Appl. Phys. Lett.* **1972**, *20*, 135.
- [33] A. S. Everhardt, S. Matzen, N. Domingo, G. Catalan, B. Noheda, *Adv. Electron. Mater.* **2016**, *2*, 1500214.
- [34] Z. Shao, N. Schnitzer, J. Ruf, O. Y. Gorobtsov, C. Dai, B. H. Goodge, T. Yang, H. Nair, V. A. Stoica, J. W. Freeland, J. P. Ruff, L.-Q. Chen, D. G. Schlom, K. M. Shen, L. F. Kourkoutis, A. Singer, *Proceedings of the National Academy of Sciences* **2023**, *120*, e2303312120.
- [35] J. F. Scott, L. Kammerdiner, M. Parris, S. Traynor, V. Ottenbacher, A. Shawabkeh, W. F. Oliver, *J. Appl. Phys.* **1988**, *64*, 787.
- [36] G. Schönweger, N. Wolff, M. R. Islam, M. Gremmel, A. Petraru, L. Kienle, H. Kohlstedt, S. Fichtner, *Adv. Sci.* **2023**, *10*, 202302296.
- [37] H. Lu, G. Schönweger, A. Petraru, H. Kohlstedt, S. Fichtner, A. Gruverman, *Adv. Funct. Mater.* **2024**, *34*, 2315169.
- [38] B. Ofuonye, J. Lee, M. Yan, C. Sun, J.-M. Zuo, I. Adesida, *Semicond. Sci. Technol.* **2014**, *29*, 095005.
- [39] V. S. Kumar, M. K. Niranjan, *J. Appl. Phys.* **2014**, *115*, 173705.
- [40] S. Torbrügge, M. Imlau, B. Schoke, C. Merschjann, O. F. Schirmer, S. Vernay, A. Gross, V. Wesemann, D. Rytz, *Phys. Rev. B* **2008**, *78*, 125112.
- [41] J. Handerek, R. Manka, A. Aleksandrowicz, J. Szatanek, *Ferroelectrics* **1978**, *22*, 735.
- [42] N. Zhong, S. Okamura, K. Uchiyama, T. Shiosaki, *Appl. Phys. Lett.* **2005**, *87*, 252901.
- [43] R. I. Eglitis, E. A. Kotomin, A. V. Postnikov, N. E. Christensen, M. A. Korotin, G. Borstel, *Ferroelectrics* **1999**, *229*, 69.
- [44] R. I. Eglitis, N. E. Christensen, E. A. Kotomin, A. V. Postnikov, G. Borstel, *Phys. Rev. B* **1997**, *56*, 8599.
- [45] R. I. Eglitis, E. A. Kotomin, G. Borstel, *physica status solidi c* **2005**, *2*, 113.
- [46] K. M. Adkison, S.-L. Shang, B. J. Bocklund, D. Klimm, D. G. Schlom, Z.-K. Liu, *APL Mater* **2020**, *8*, 081110.
- [47] H. Okamoto, *J. Phase Equilib.* **1992**, *13*, 217.
- [48] R. E. Honig, D. A. Kramer, *RCA Review* **1969**, *30*, 567.
- [49] G. Koster, B. L. Kropman, G. J. H. M. Rijnders, D. H. A. Blank, H. Rogalla, *Mater. Sci. Eng., B* **1998**, *56*, 209.
- [50] T. Schwaigert, S. Salmani-Rezaie, M. R. Barone, H. Paik, E. Ray, M. D. Williams, D. A. Muller, D. G. Schlom, K. Ahadi, *J. Vac. Sci. Technol. A* **2023**, *41*, 022703.
- [51] A. Nazeri-Eshghi, A. X. Kuang, J. D. Mackenzie, *J. Mater. Sci.* **1990**, *25*, 3333.
- [52] S. Triebwasser, *Phys. Rev.* **1956**, *101*, 993.
- [53] G. Shirane, H. Danner, A. Pavlovic, R. Pepinsky, *Phys. Rev.* **1954**, *93*, 672.
- [54] A. K. Tagantsev, *Ferroelectrics* **1986**, *69*, 321.
- [55] L. Q. Chen, *J. Am. Ceram. Soc.* **2008**, *91*, 1835.
- [56] Y. L. Li, S. Y. Hu, Z. K. Liu, L. Q. Chen, *Acta Mater.* **2002**, *50*, 395.
- [57] Y. L. Li, S. Y. Hu, Z. K. Liu, L. Q. Chen, *Appl. Phys. Lett.* **2002**, *81*, 427.
- [58] B. L. Henke, E. M. Gullikson, J. C. Davis, *At. Data Nucl. Data Tables* **1993**, *54*, 181.

- [59] A. H. Romero, D. C. Allan, B. Amadon, G. Antonius, T. Applencourt, L. Bague, J. Bieder, F. Bottin, J. Bouchet, E. Bousquet, F. Bruneval, G. Brunin, D. Caliste, M. Côté, J. Denier, C. Dreyer, P. Ghosez, M. Giantomassi, Y. Gillet, O. Gingras, D. R. Hamann, G. Hautier, F. Jollet, G. Jomard, A. Martin, H. P. C. Miranda, F. Naccarato, G. Petretto, N. A. Pike, V. Planes, et al., *J. Chem. Phys.* **2020**, *152*, 124102.
- [60] X. Gonze, B. Amadon, G. Antonius, F. Arnardi, L. Bague, J.-M. Beuken, J. Bieder, F. Bottin, J. Bouchet, E. Bousquet, N. Brouwer, F. Bruneval, G. Brunin, T. Cavignac, J.-B. Charraud, W. Chen, M. Côté, S. Cottenier, J. Denier, G. Geneste, P. Ghosez, M. Giantomassi, Y. Gillet, O. Gingras, D. R. Hamann, G. Hautier, X. He, N. Helbig, N. Holzwarth, Y. Jia, et al., *Comput. Phys. Commun.* **2020**, *248*, 107042.
- [61] X. Gonze, F. Jollet, F. A. Araujo, D. Adams, B. Amadon, T. Applencourt, C. Audouze, J.-M. Beuken, J. Bieder, A. Bokhanchuk, E. Bousquet, F. Bruneval, D. Caliste, M. Côté, F. Dahm, F. Da Pieve, M. Delaveau, M. Di Gennaro, B. Dorado, C. Espejo, G. Geneste, L. Genovese, A. Gerossier, M. Giantomassi, Y. Gillet, D. R. Hamann, L. He, G. Jomard, J. L. Janssen, S. Le Roux, et al., *Comput. Phys. Commun.* **2016**, *205*, 106.
- [62] M. J. van Setten, M. Giantomassi, E. Bousquet, M. J. Verstraete, D. R. Hamann, X. Gonze, G.-M. Rignanese, *Comput. Phys. Commun.* **2018**, *226*, 39.
- [63] D. R. Hamann, *Phys. Rev. B* **2013**, *88*, 085117.
- [64] J. P. Perdew, M. Ernzerhof, K. Burke, *J. Chem. Phys.* **1996**, *105*, 9982.
- [65] J. P. Perdew, K. Burke, M. Ernzerhof, *Phys. Rev. Lett.* **1996**, *77*, 3865.
- [66] J. D. Pack, H. J. Monkhorst, *Phys. Rev. B* **1977**, *16*, 1748.
- [67] H. J. Monkhorst, J. D. Pack, *Phys. Rev. B* **1976**, *13*, 5188.
- [68] J. P. Perdew, Y. Wang, *Phys. Rev. B* **1992**, *45*, 13244.
- [69] G. Kresse, D. Joubert, *Phys. Rev. B* **1999**, *59*, 1758.
- [70] G. Kresse, J. Furthmüller, *Phys. Rev. B* **1996**, *54*, 11169.
- [71] G. Kresse, J. Furthmüller, *Comput. Mater. Sci.* **1996**, *6*, 15.
- [72] G. Kresse, J. Hafner, *Phys. Rev. B* **1993**, *47*, 558.
- [73] P. E. Blöchl, *Phys. Rev. B* **1994**, *50*, 17953.
- [74] T. E. Smidt, S. A. Mack, S. E. Reyes-Lillo, A. Jain, J. B. Neaton, *Sci. Data* **2020**, *7*, 72.
- [75] Y. L. Li, L. E. Cross, L. Q. Chen, *J. Appl. Phys.* **2005**, *98*, 064101.
- [76] M. J. Haun, E. Furman, S. J. Jang, H. A. McKinstry, L. E. Cross, *J. Appl. Phys.* **1987**, *62*, 3331.
- [77] H. N. Lee, S. M. Nakhmanson, M. F. Chisholm, H. M. Christen, K. M. Rabe, D. Vanderbilt, *Phys. Rev. Lett.* **2007**, *98*, 217602.
- [78] T. Le, O. Kurt, J. Ouyang, J. Wang, L.-Q. Chen, E. L. Lin, J. G. Ekerdt, Y. Ren, *Scr. Mater.* **2020**, *178*, 489.
- [79] M. J. Weber, *Handbook of Optical Materials*, CRC Press, Boca Raton, FL, USA **2018**.
- [80] H. Uwe, T. Sakudo, *J. Phys. Soc. Jpn.* **1975**, *38*, 183.
- [81] I. C. Infante, S. Lisenkov, B. Dupé, M. Bibes, S. Fusil, E. Jacquet, G. Geneste, S. Petit, A. Courtial, J. Juraszek, L. Bellaiche, A. Barthélémy, B. Dkhil, *Phys. Rev. Lett.* **2010**, *105*, 057601.

## Supporting Information

### **Colossal Strain Tuning of Ferroelectric Transitions in KNbO<sub>3</sub> Thin Films**

*Sankalpa Hazra\**, *Tobias Schwaigert\**, *Aiden Ross*, *Haidong Lu*, *Utkarsh Saha*, *Victor Trinquet*,  
*Betul Akkopru-Akgun*, *Benjamin Z. Gregory*, *Anudeep Mangu*, *Suchismita Sarker*, *Tatiana*  
*Kuznetsova*, *Saugata Sarker*, *Xin Li*, *Matthew R. Barone*, *Xiaoshan Xu*, *John W. Freeland*, *Roman*  
*Engel-Herbert*, *Aaron M. Lindenberg*, *Andrej Singer*, *Susan Trolier-McKinstry*, *David A. Muller*,  
*Gian-Marco Rignanese*, *Salva Salmani-Rezaie*, *Vladmir A. Stoica*, *Alexei Gruverman*, *Long-Qing*  
*Chen*, *Darrell G. Schlom*, and *Venkatraman Gopalan*

## Note 1: Phase-field simulations

**Table S1.** Set of Landau expansion coefficients

Coefficient	Value	Unit
$\alpha_1$	$1.906 \times 10^7 \left( \coth \left( \frac{54}{T(K)} \right) - \coth \left( \frac{54}{650} \right) \right)$	$[\text{C}^{-2} \text{m}^2 \text{N}]$
$\alpha_{11}$	$-5.86 \times 10^8$	$[\text{C}^{-4} \text{m}^6 \text{N}]$
$\alpha_{12}$	$9.66 \times 10^8$	$[\text{C}^{-4} \text{m}^6 \text{N}]$
$\alpha_{111}$	$2.71 \times 10^9$	$[\text{C}^{-6} \text{m}^{10} \text{N}]$
$\alpha_{112}$	$-2.2 \times 10^9$	$[\text{C}^{-6} \text{m}^{10} \text{N}]$
$\alpha_{123}$	$4.4 \times 10^9$	$[\text{C}^{-6} \text{m}^{10} \text{N}]$
$\alpha_{1111}$	$1.74 \times 10^{10}$	$[\text{C}^{-8} \text{m}^{14} \text{N}]$
$\alpha_{1112}$	$5.99 \times 10^9$	$[\text{C}^{-8} \text{m}^{14} \text{N}]$
$\alpha_{1122}$	$2.5 \times 10^{10}$	$[\text{C}^{-8} \text{m}^{14} \text{N}]$
$\alpha_{1123}$	$-1.63 \times 10^{10}$	$[\text{C}^{-8} \text{m}^{14} \text{N}]$

Modified from Liang et. al<sup>[1]</sup> based upon experimental data from <sup>[2-4]</sup>.

**Table S2.** Elastic stiffness coefficients and electrostrictive coefficients

$c_{11}$	$2.3 \times 10^{11}$	$[\text{Pa}]$
$c_{22}$	$0.9 \times 10^{11}$	$[\text{Pa}]$
$c_{44}$	$0.76 \times 10^{10}$	$[\text{Pa}]$
$Q_{11}$	0.11	$[\text{C}^{-2} \text{m}^4]$
$Q_{13}$	-0.053	$[\text{C}^{-2} \text{m}^4]$

$Q_{44}$	0.052	$[\text{C}^{-2} \text{m}^4]$
----------	-------	------------------------------

The phase diagram is established based on the polydomain structures obtained at equilibrium from phase-field simulations. The temperature is varied from 10 K to 1300 K at intervals of 25 K and the strain is varied from -4.5% to 0% at intervals of 0.1%. The phase classification in the phase diagram is performed based on the domain structure that exists at the end of a simulation.

The paraelectric region in the phase diagram marks the phase where  $(P_1, P_2, P_3) = 0$ . For the single-phase tetragonal, orthorhombic and rhombohedral regions, all the polarization vectors falling within the interior of a conical surface with the boundaries of the surface tilted  $10^\circ$  to the family of nominal crystallographic directions [001], [101] and [111] are classified in the single-phase regions, with the phase fraction in the classified phase greater than 0.95. For polarization vectors deviating more than  $10^\circ$  from the above nominal crystallographic directions, they are classified in the monoclinic  $M_A$  and  $M_C$  phases depending on the minimum angle created with the family of monoclinic planes (110) or (100) with phase fraction greater than 0.95.

The visualization of the domain structures from phase-field simulations also confirms the classified single phases with the remaining phase fraction of the polarization vectors in these single-phase regions formed in the domain walls separating two domain variants of the same phase, e.g., orthorhombic [101] and orthorhombic [10-1]. The remaining data points in the phase diagram not satisfying the above phase classification criteria are classified in either a two-phase mixture or a three-phase mixture depending on the phase fraction and the visualization of the domain structure.

**Table S3:** Comparison of  $C$ ,  $Q$ ,  $S$  and  $\frac{dT_c}{d\varepsilon}$  coefficients for  $\text{KNbO}_3$  and related materials:

Material	$C$ [K]	$Q_{11}$ [ $\text{m}^4\text{C}^{-2}$ ]	$Q_{13}$ [ $\text{m}^4\text{C}^{-2}$ ]	$S_{11}$ [ $\text{m}^2\text{N}^{-1}$ ]	$S_{13}$ [ $\text{m}^2\text{N}^{-1}$ ]	$\frac{dT_c}{d\varepsilon}$ = $4\varepsilon_0 C \frac{(Q_{13})}{(S_{11}+S_{13})}$
$\text{SrTiO}_3$ <sup>[5]</sup>	$0.505 \times 10^5$	0.0457	-0.0135	$3.8 \times 10^{-12}$	$-9.1 \times 10^{-13}$	83 K
$\text{PbTiO}_3$ <sup>[6]</sup>	$1.5 \times 10^5$	0.089	-0.026	$8.0 \times 10^{-12}$	$-2.5 \times 10^{-12}$	251 K

BaTiO <sub>3</sub> <sup>[7]</sup>	$1.37 \times 10^5$	0.10	-0.034	$9.0 \times 10^{-12}$	$-3.2 \times 10^{-12}$	284 K
KTaO <sub>3</sub> <sup>[8,9]</sup>	$0.698 \times 10^5$	0.0872	-0.023	$2.5 \times 10^{-12}$	$-0.4 \times 10^{-12}$	280 K
KNbO <sub>3</sub>	$1.6 \times 10^5$	0.11	-0.053	$5.6 \times 10^{-12}$	$-1.6 \times 10^{-12}$	<b>750 K</b>

**Table S4: Parameters used for diffraction simulations**

Atom	$f^1$	$f^2$	$s$
K	19.3678	0.746466	$1.01 \text{E-}11 \text{ (m}^3/\text{C)}$
Nb	40.5697	1.67439	$-0.56 \text{E-}11 \text{ (m}^3/\text{C)}$
O	8.035	0.021	$-3.15 \text{E-}11 \text{ (m}^3/\text{C)}$

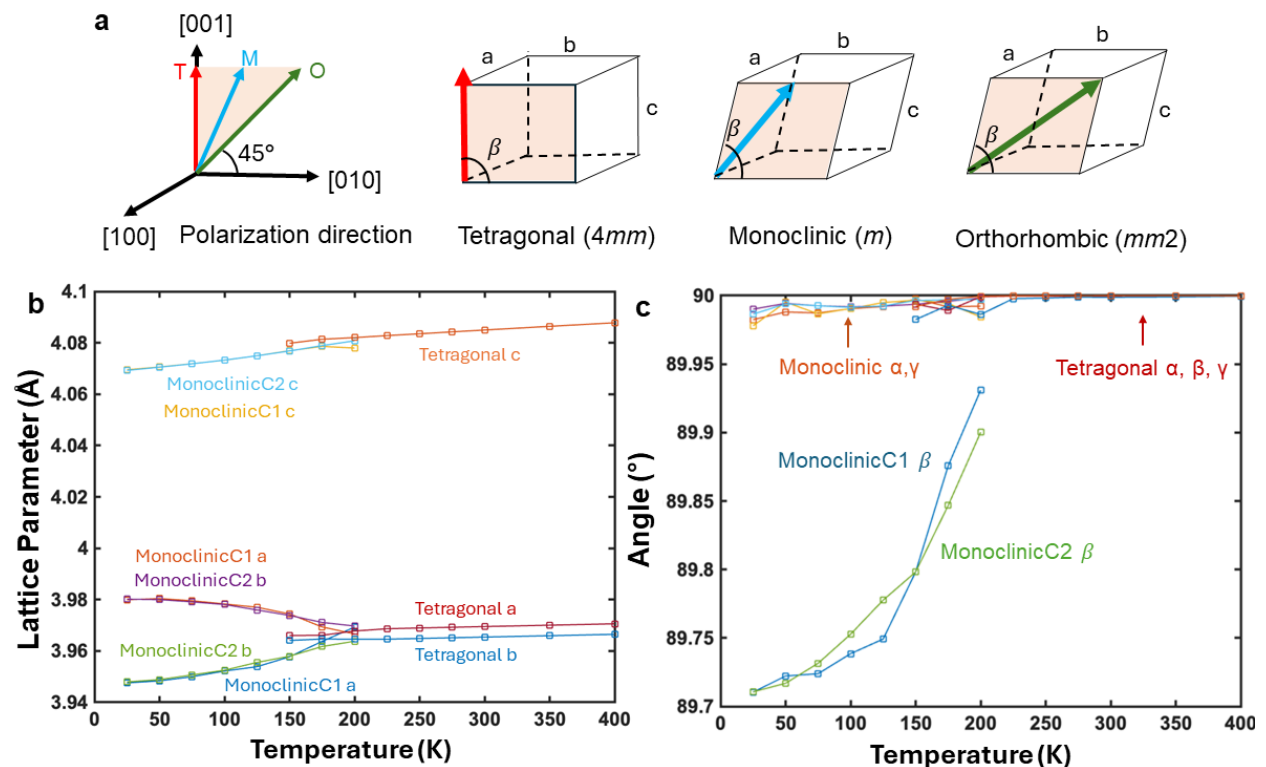


**Figure S1:** Schematic of polarization direction and unit cell corresponding to Tetragonal ( $4mm$ ), Monoclinic ( $m$ ) and Orthorhombic ( $mm2$ ) phases observed in phase field simulations under compressive strains. Lattice parameters of KNbO<sub>3</sub> on GdScO<sub>3</sub> as a function of temperature across the tetragonal-to-monoclinic phase transition is shown in (b) and (c). Monoclinic C1 and C2 refer to the two variants of the monoclinic phases stabilized from symmetry lowering from the

Tetragonal phase. These two monoclinic unit cells represent shearing along [100] and [010] respectively. Lattice parameters and angles are all derived from phase field simulations.

The phase transitions seen from the phase field simulations are primarily driven by a reduction in the total free energy. In the case of ferroelectric domain structures under a substrate induced epitaxial strain, the main driving forces involve a competition between the intrinsic stability of the ferroelectric phase (Landau Energy) which favors the polarization along certain crystallographic directions and the elastic energy which aligns the polarization driven by the misfit strain due to the lattice mismatch between the film and the substrate.

From the Landau energy, under stress-free conditions, we find that the cubic phase is stabilized above  $T_c = 435$  °C, the tetragonal phase is stabilized from 225-435 °C, the orthorhombic phase is stabilized from -50-225 °C, and the rhombohedral phase is stable below -50 °C [1]. However, under thin-film boundary conditions<sup>[10]</sup>, these bulk phase boundaries will be shifted and the bulk phases themselves may become distorted to better compensate for the elastic boundary conditions.

The driving mechanism for the stabilization of the tetragonal phase with out-of-plane polarization under a compressive strain is primarily elastic in origin. Under stress free conditions, this tetragonal phase possesses an intrinsic compressive strain along its a-axis and tensile strain along its c-axis (using the high symmetry cubic phase as the strain zero reference state). In the compressive strain region, since the tetragonal phase best matches the strain conditions imposed by the substrate, it has a minimal elastic energy in comparison to the other possible phases. While the tetragonal phase with out-of-plane polarization is favored with increasing compressive strain, the lower symmetry phases become more stable at lower compressive strains < - 0.5% regime.

Under these strain conditions, distorted versions of lower symmetry bulk orthorhombic and rhombohedral phases are observed which are described by monoclinic phases with space group *Pm* and *Cm* respectively in our phase diagram.

The *Pm* monoclinic phase occurs at strain values from  $\sim -1\%$  to  $\sim -0.75\%$  at room temperature with the phase boundaries shifting towards higher compressive strains at lower temperatures. Conceptually, this monoclinic phase (**Figure S1a**) can be viewed as a distorted orthorhombic phase, where the compressive strain causes the polarization to rotate away from the  $45^\circ$  angle seen in the bulk orthorhombic phase towards the c-axis. This monoclinic phase has multiple domain variants resulting in a twinned domain microstructure seen in **Figure 3c, Main text. Figure S1b and c** show the change of unit cell lattice parameters as function of temperature predicted for  $\text{KNbO}_3$  on  $\text{GdScO}_3$  ( $\epsilon \sim -1.1\%$ ) showing the structural phase transition from a tetragonal (*P4mm*) to monoclinic (*Pm*) structure.

The *Cm* monoclinic phase occurs at a strain around  $\sim -0.25\%$  at room temperature with the phase boundaries shifting towards higher compressive strains at lower temperatures. This monoclinic phase can be viewed as a distorted version of the bulk rhombohedral phase where the compressive strain causes the polarization to rotate towards the c-axis away from the [111] nominal direction.

Furthermore, these thin-film boundary conditions allow for the coexistence of multiple ferroelectric phases which may be understood from the theory of strain-phase decomposition<sup>[11]</sup>.

For a system with strain inhomogeneity, i.e., different strains along the in-plane a and b axes, at a fixed temperature, the maximum number of possible coexisting phases is three according to the Gibbs phase rule. Considering the three possible phases as  $\alpha$ ,  $\beta$  and  $\gamma$  with homogeneous strains  $\varepsilon_1^i$  and  $\varepsilon_2^i$  ( $i = \alpha, \beta, \gamma$ ) at equilibrium, the triangular region of the common tangent plane of the free energy bounded by the three tangent points corresponds to the three-phase coexisting region in the  $\varepsilon_1$ - $\varepsilon_2$  diagram. For each two of the single-phase free energy surfaces, a set of common tangent planes, and the associated tangent points and lines can be identified. These lines link the local strains at equilibrium and constitute the two-phase regions in the  $\varepsilon_1$ - $\varepsilon_2$  phase diagram. If we only consider the biaxial strain, i.e.,  $\varepsilon_1 = \varepsilon_2$ , we can construct a diagonal  $\varepsilon_1 = \varepsilon_2$  line in the  $\varepsilon_1$ - $\varepsilon_2$  phase diagram which gives us the possible two-phase and three-phase coexistence regions at each temperature.

The temperature-strain phase diagram for biaxial compressive strains where the tetragonal phase with out-of-plane polarization is mainly favored over other phases as mentioned earlier due to the dominance of the elastic energy over other energy contributions. However, in the tensile strain region, above room temperature, in-plane orthorhombic or in-plane tetragonal phases are favored<sup>[12]</sup> as these phases possess a spontaneous in-plane tensile strain and an out-of-plane compressive strain along the c-axis leading to the best match with the strain conditions imposed by the substrate and consequently, lower elastic energy compared to other phases.

## Note 2: Density functional theory simulation.

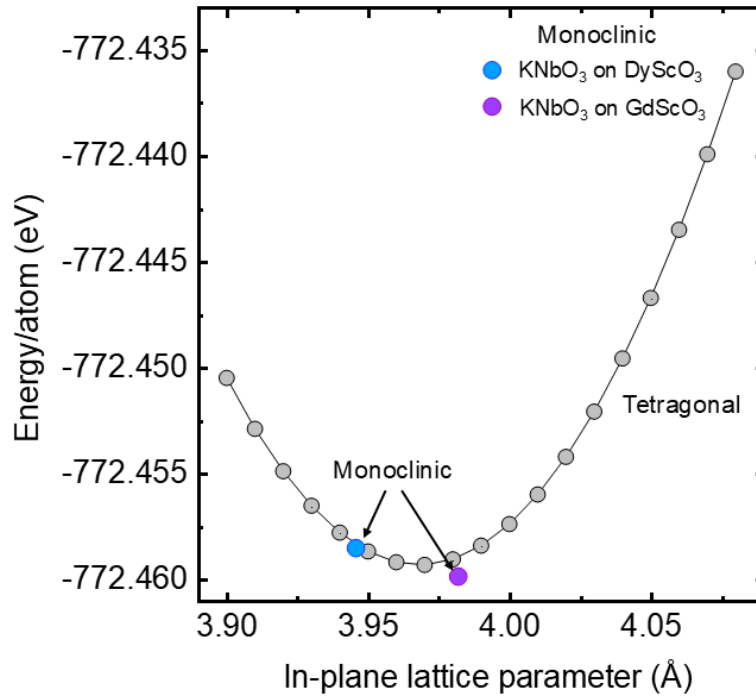


**Figure S2:** Atomic level density functional theory calculations (DFT) of total energy/atom showing the competitive stability of the tetragonal phase (grey curve) and monoclinic phase for KNbO<sub>3</sub> on GdScO<sub>3</sub> and KNbO<sub>3</sub> on DyScO<sub>3</sub> (blue and purple points).

For the tetragonal unit cell, the in-plane lattice parameter was fixed while the out-of-plane lattice parameter and internal atomic positions were allowed to relax. Hence, a continuous curve (grey) for the tetragonal structure could be extracted as a function in-plane lattice parameter. However, for monoclinic symmetry, the large number of degrees of freedom restricts the same methodology. For calculations for the monoclinic unit cell, the in-plane lattice parameters of KNbO<sub>3</sub> on GdScO<sub>3</sub> and DyScO<sub>3</sub> substrates were adapted from phase field simulations at 25K for both samples. Hence, total energy/atom of the monoclinic unit cell could be calculated only at two distinct points.

From figure S2, although the monoclinic phase seems to be energetically favored over the tetragonal one, the difference in energy is less than 1 meV/atom, which is within the typical error margin of DFT. Hence, through DFT calculations the tetragonal and monoclinic phases are predicted to be comparable to one another.

It is important to note that, for calculations of total energy/atom our DFT does not account for multiple domain variants in the lower symmetry monoclinic phase, which has both been experimentally observed and predicted through phase-field simulations.

**Note 3: Dependence of  $\frac{dT_c}{d\varepsilon}$  and  $\frac{dP_r}{d\varepsilon}$  on electrostriction ( $Q_{13}$ ) and elastic compliance ( $S_{11} + S_{13}$ ) coefficients.**

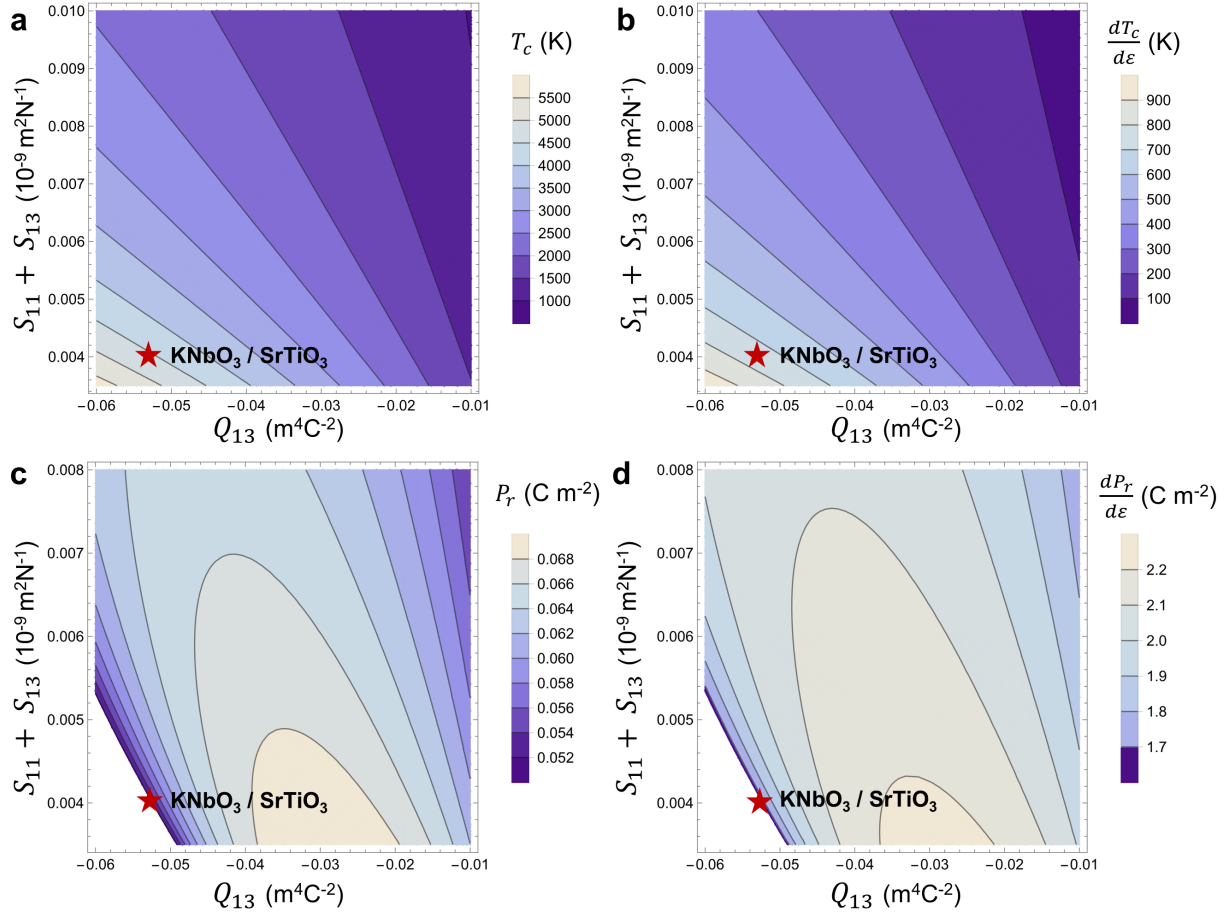


**Figure S3:** Contour plot showing the dependence of (a)  $T_c$ , (b)  $\frac{dT_c}{d\varepsilon}$ , (c)  $P_r$ , (d)  $\frac{dP_r}{d\varepsilon}$  on electrostriction ( $Q_{13}$ ) and elastic compliance ( $S_{11} + S_{13}$ ) coefficients for compressively strained tetragonal phase calculated from analytical thermodynamic expressions, where any other relevant tensor coefficients are assumed to be the same as for  $\text{KNbO}_3$  (Table S1 Supporting Information). The white regions in panel c and d represent points where no real solution of the polarization exists. The red star on each panel denotes  $\text{KNbO}_3$  on  $\text{SrTiO}_3$  film, showing that the low ( $S_{11} + S_{13}$ ) and high  $Q_{13}$  values of  $\text{KNbO}_3$  render a high  $T_c$  and  $\frac{dT_c}{d\varepsilon}$  value, however  $P_r$  and  $\frac{dP_r}{d\varepsilon}$  are lower than maximum achievable.

#### **Note 4: Growth of strained KNbO<sub>3</sub> thin films by suboxide molecular beam epitaxy**

Epitaxial KNbO<sub>3</sub> thin films were grown on (001) SrTiO<sub>3</sub>, (110)<sub>o</sub> DyScO<sub>3</sub> and (110)<sub>o</sub> GdScO<sub>3</sub> substrates by suboxide molecular beam epitaxy with in-situ high pressure reflection high energy electron diffraction (RHEED). RHEED was used to monitor the evolution of surface structure reconstruction during growth. **Figure S4a-c** show RHEED patterns along the high symmetry directions where diffractions streaks and Kikuchi lines are visible for GdScO<sub>3</sub> (110)<sub>o</sub>, DyScO<sub>3</sub> (110)<sub>o</sub> and SrTiO<sub>3</sub> (001) substrates during the deposition of the first monolayer of KNbO<sub>3</sub>. **Figure S4d-f** show the KNbO<sub>3</sub> RHEED streaks immediately after the deposition was stopped, where the shutter of the NbO<sub>2</sub> and potassium source have been closed, but still at growth temperature (650 °C) and immersed in ozone. Atomic force microscopy (AFM) images are shown in **Figure S5** at different magnifications. Atomic steps are visible from the 0.1° off-cut GdScO<sub>3</sub> and SrTiO<sub>3</sub> are visible. The root-mean-square (rms) roughness for KNbO<sub>3</sub> (001) on GdScO<sub>3</sub> (110)<sub>o</sub> (**Figure S5d**) is 0.55 nm, KNbO<sub>3</sub> (001) on DyScO<sub>3</sub> (110)<sub>o</sub> (**Figure S5e**) is 0.61 nm and KNbO<sub>3</sub> (001) on SrTiO<sub>3</sub> (001) is 0.74 nm (**Figure S5f**).

**Figure S6a** shows the X-ray reciprocal space mapping (RSM) around the GdScO<sub>3</sub> (332) DyScO<sub>3</sub> (332) and SrTiO<sub>3</sub> (103) reflections confirm that the KNbO<sub>3</sub> films are commensurately strained to the respective substrates. **Figure S6b** compares the expected and measured out-of-plane lattice constants for KNbO<sub>3</sub> films grown on different substrates. **Figure S6c** shows the  $\theta - 2\theta$  x-ray diffraction (XRD) scans for all three films. The rocking curves full width at half maximum (FWHM) of the KNbO<sub>3</sub> films and the GdScO<sub>3</sub> (110)<sub>o</sub>, DyScO<sub>3</sub> (110)<sub>o</sub> and SrTiO<sub>3</sub> (001) substrates are shown in **Fig. S7**. FWHM are comparable to that of the respective substrates and increase with lattice mismatch between the substrate and the film. For the “cube-on-pseudocube” substrates (GdScO<sub>3</sub> and DyScO<sub>3</sub>), rocking curves are collected along the two orthogonal in-plane directions of the substrate.

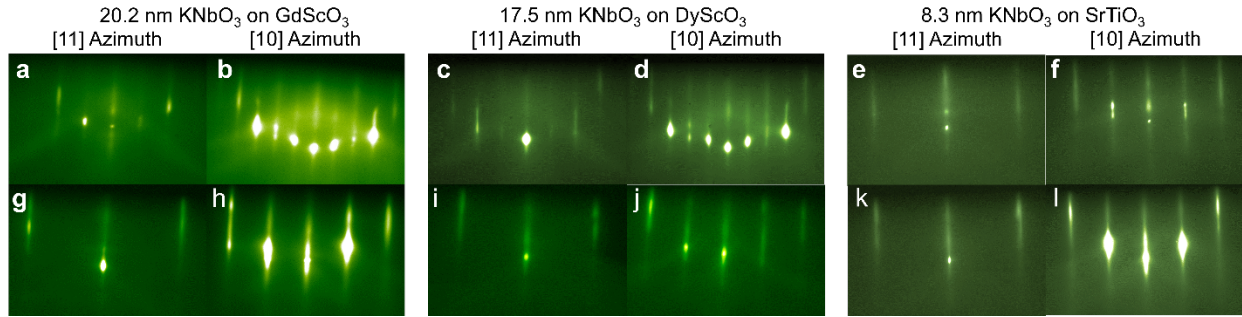


**Figure S4:** RHEED patterns of KNbO<sub>3</sub> films grown on **a.** GdScO<sub>3</sub>, **b.** DyScO<sub>3</sub> and **c.** SrTiO<sub>3</sub> substrates. The top row depicts the deposition of the first unit-cell and the bottom row represents the patterns immediately after deposition was stopped.

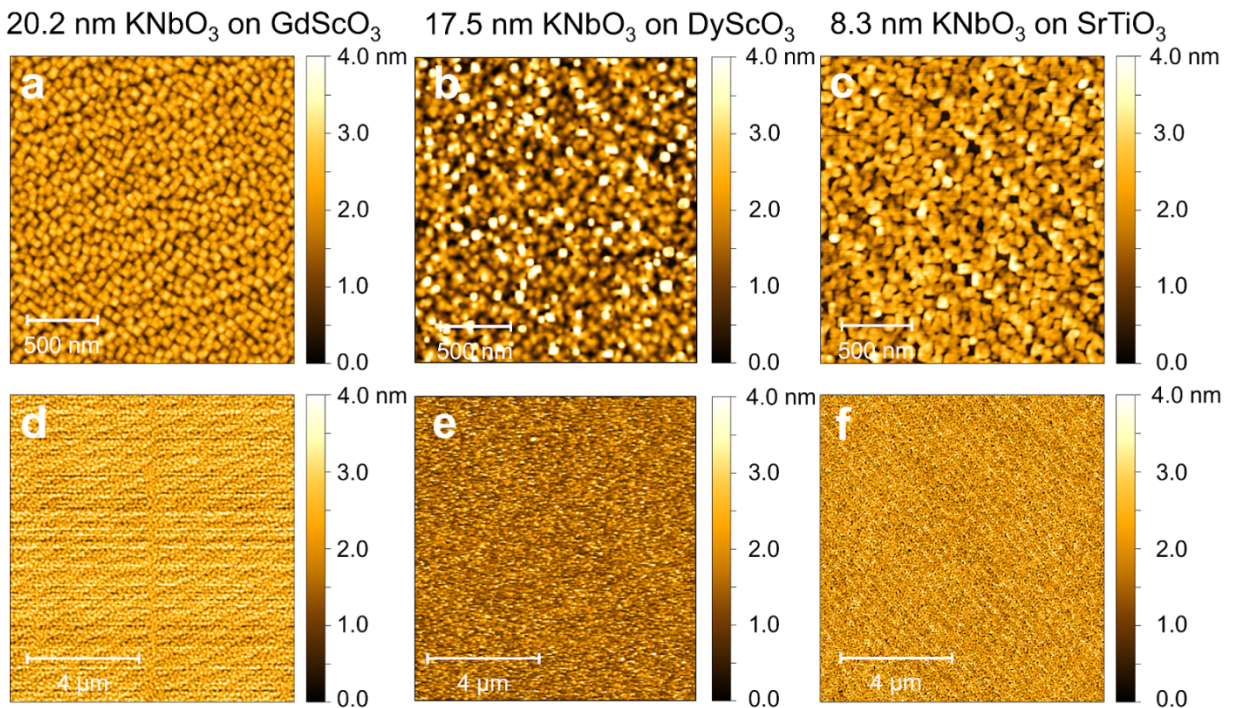


**Figure S5:** AFM images of KNbO<sub>3</sub> films grown on **(a), (d)** (110)<sub>o</sub> GdScO<sub>3</sub>, **(b), (e)** (110)<sub>o</sub> DyScO<sub>3</sub> and **(c), (f)** (001) SrTiO<sub>3</sub> substrates, with RMS roughness  $\sim < 1$  nm for all the three films.

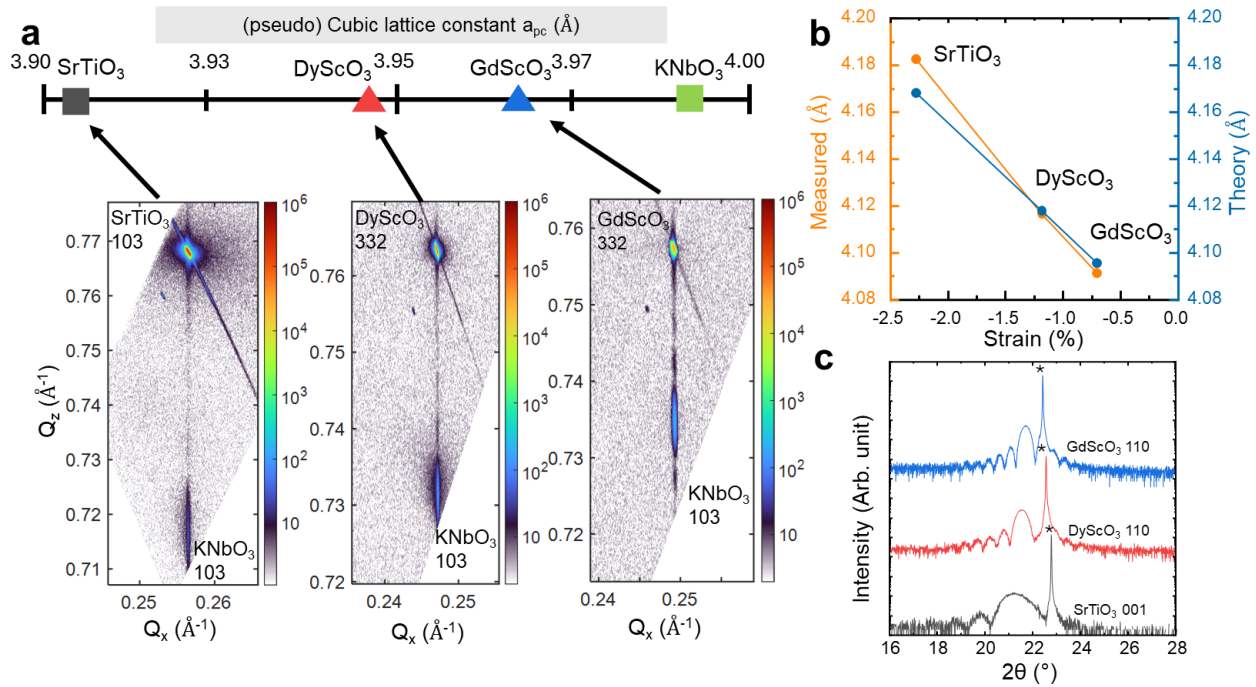


**Figure S6:** (a) Lab X-ray based reciprocal space maps for KNbO<sub>3</sub> grown on SrTiO<sub>3</sub>, GdScO<sub>3</sub> and SrTiO<sub>3</sub> substrates showing coherent strained KNbO<sub>3</sub> thin films on substrates. (b) Measured out-of-plane lattice parameter of KNbO<sub>3</sub> as a function of strain measured by XRD, compared to expected lattice parameter from elastic theory. (c)  $\theta - 2\theta$  XRD scans for the same KNbO<sub>3</sub> films grown on various substrates, exhibiting Laue fringes indicating an abrupt interface between film and substrate. Only (00 $l$ ) reflections are visible and were used to calculate the out-of-plane lattice constant in (b).

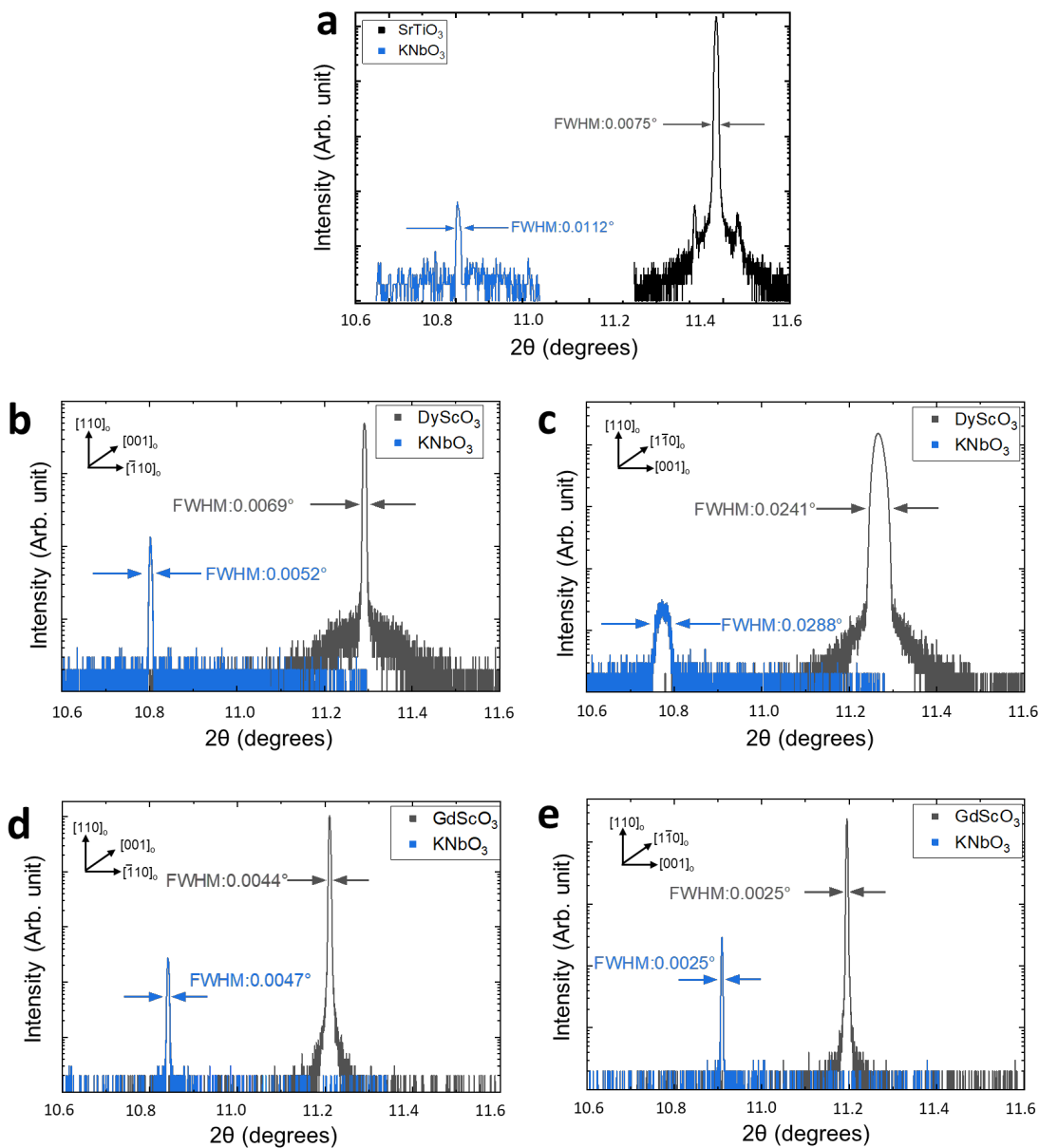


**Figure S7:** Lab X-ray based overlaid rocking curves for KNbO<sub>3</sub> grown on SrTiO<sub>3</sub>, DyScO<sub>3</sub> and GdScO<sub>3</sub> substrates. (a) Overlaid 001 SrTiO<sub>3</sub> and 001 KNbO<sub>3</sub> peaks, showing comparable FWHMs. (b) and (c) Overlaid 001 KNbO<sub>3</sub> and 110 DyScO<sub>3</sub> peaks along the two orthogonal in-plane directions of the substrate. (b) and (c) Overlaid 001 KNbO<sub>3</sub> and 110 GdScO<sub>3</sub> peaks along the two orthogonal in-plane directions of the substrate.

## Note 5: Derivation of out-of-plane lattice constant calculations from elastic theory

The out-of-plane lattice constant  $a_{\perp}$  can be calculated from the out-of-plane strain,  $\epsilon_{33} = \frac{(a_{\perp} - a_{KNO})}{a_{KNO}}$  by expanding the tensor equation (in Einstein notation):  $\sigma_{33} = c_{ijkl}\epsilon_{kl}$  for  $\sigma_{33}$  and recognizing that  $\sigma_{33} = 0$  because the film is free of stress in the out-of-plane direction. This leads to:

$$a_{\perp} = \frac{c_{KNO} \left( c_{33} 2c_{13} \left( \frac{a_{STO} - a_{KNO}}{a_{KNO}} \right) \right)}{c_{33}} \quad (1)$$

Where  $c_{13}$  and  $c_{33}$  are elastic stiffness tensor coefficients<sup>[13]</sup> of KNbO<sub>3</sub> in Voigt notation and  $a_{STO}$  and  $a_{KNO}$  are the lattice constants of unstrained KNbO<sub>3</sub> and SrTiO<sub>3</sub>, respectively. The calculated out-of-plane lattice constant expected for a commensurately strained KNbO<sub>3</sub> film on SrTiO<sub>3</sub> at room temperature is 4.168 Å (**Figure S6b**). This is lower than the 4.182 Å ± 0.015 Å value measured by X-ray diffraction for the commensurately strained 8.3 nm thick KNbO<sub>3</sub> films.

In contrast to the extended out-of-plane lattice spacing observed for the commensurately strained KNbO<sub>3</sub> film grown on a SrTiO<sub>3</sub> substrate, the 17.5 and 20.2 nm thick commensurately strained KNbO<sub>3</sub>/DyScO<sub>3</sub> and KNbO<sub>3</sub>/GdScO<sub>3</sub> shown in **Figure S6 b - c** agree with the expected out-of-plane spacing, calculated with elastic theory. Because GdScO<sub>3</sub> is orthorhombic, the in-plane biaxial strains  $\epsilon_{11}$  and  $\epsilon_{22}$  imposed by the substrate are no longer equal and the equation for  $a_{\perp}$  becomes,

$$a_{\perp} = - \frac{c_{13}c_{KNO} (a_{GSO170} - 4a_{KNO} + a_{GSO001})}{2a_{KNO}c_{33}}$$

where  $a_{GSO001}$  and  $a_{GSO110}$  are the in-plane distances that establish  $\epsilon_{11}$  and  $\epsilon_{22}$  through commensurate strain. Specifically,  $a_{GSO001}$  is the c-axis length of GdScO<sub>3</sub> (7.931 Å) and  $a_{GSO110}$  is the 110 of GdScO<sub>3</sub> (7.940 Å) and  $a_{DSO001}$  is the c-axis length of DyScO<sub>3</sub> (7.903 Å) and  $a_{DSO110}$  is the 110 of DyScO<sub>3</sub> (7.891 Å)<sup>[14]</sup> where we are using the non-standard *Pbnm* setting of GdScO<sub>3</sub> and DyScO<sub>3</sub> as is most common in the literature. Here the calculations result in an expected spacing for GdScO<sub>3</sub> of 4.095 Å and 4.118 Å for DyScO<sub>3</sub> at room temperature compared to the 4.091 Å ± 0.015 Å for GdScO<sub>3</sub> and 4.117 Å ± 0.015 Å for DyScO<sub>3</sub> measured by X-ray diffraction. The films grown on GdScO<sub>3</sub> and DyScO<sub>3</sub> do not show a large deviation between the measured and calculated out-of-plane lattice parameters.

## Note 6: Transmission Electron Microscopy

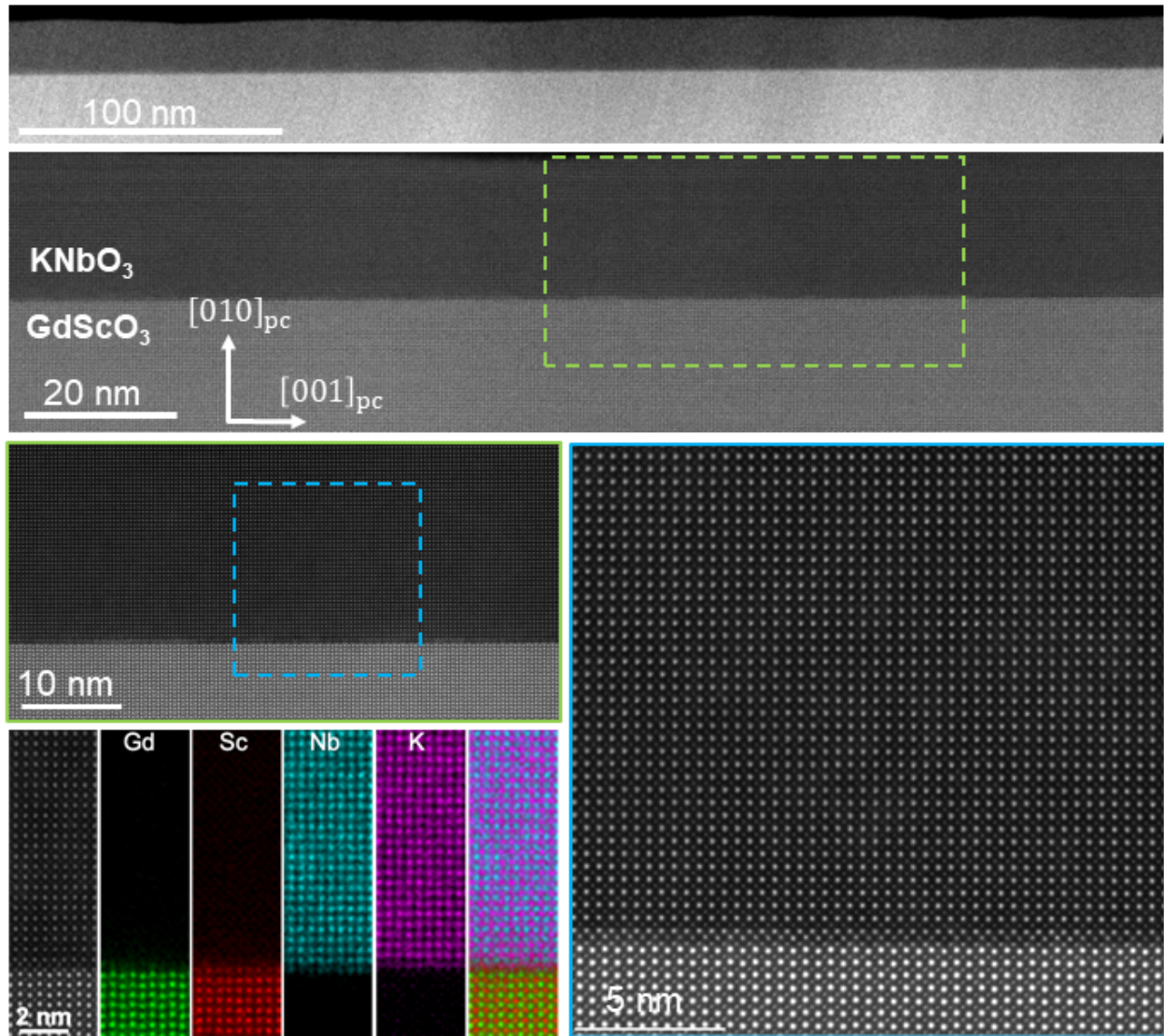


**Figure S8:** HAADF-STEM images of  $\text{KNbO}_3$  thin film grown on  $\text{GdScO}_3$  substrate. The interface structure is uniform throughout the sample, indicating a coherent strain between the film and the substrate. No extended defects are observed, which suggests high-quality epitaxial growth. The atomic resolution EDX map reveals an intermixing of metal ions at the interface, primarily involving scandium from the substrate and niobium from the film. This intermixed layer is crucial for maintaining charge neutrality at the KO terminating layer. The absence of defects and the coherent strain between the  $\text{KNbO}_3$  film and the  $\text{GdScO}_3$  substrate underscore the high quality of the epitaxial growth.

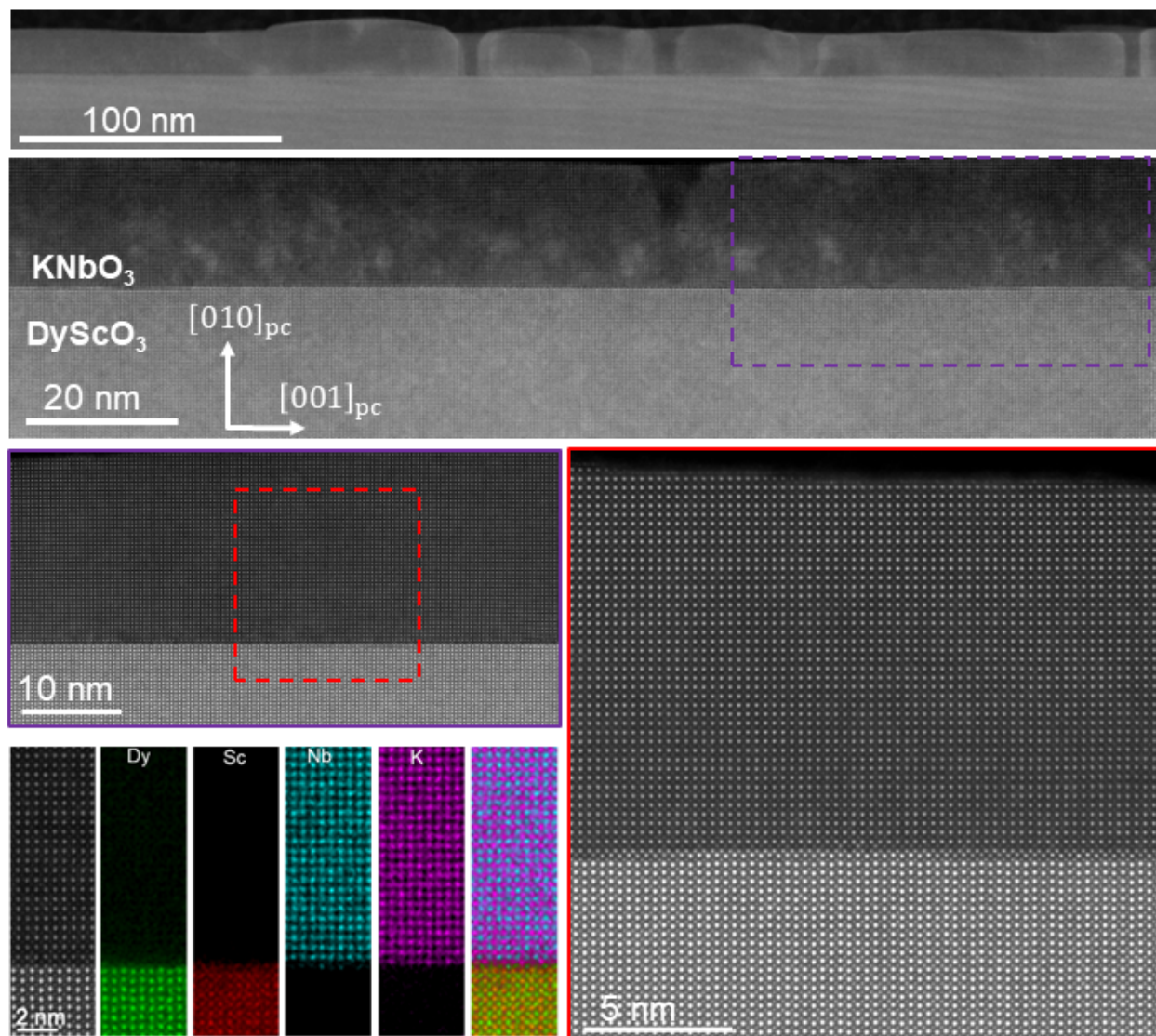


**Figure S9:** HAADF-STEM images of  $\text{KNbO}_3$  thin film grown on  $\text{DyScO}_3$  substrate. At low magnification, the growth appears to follow the island growth model rather than a layer-by-layer growth, as evidenced by the presence of islands throughout the TEM sample. Additionally, low-angle grain boundaries are observed within the film, suggesting some degree of misorientation between the grains. High-magnification images, taken from the larger grains, show that the interface between the film and the substrate is uniform and that the film is coherently strained to the substrate in these regions. This coherence indicates that, despite the island growth mode, large grains maintain a high-quality interface. The atomic resolution EDX map reveals similar intermixing of metal ions at the interface as seen for  $\text{KNbO}_3$  film on  $\text{GdScO}_3$  substrate. This intermixed layer is essential for maintaining the charge neutrality of the KO terminating layer, similar to the behavior observed in the  $\text{KNbO}_3/\text{GdScO}_3$  system.

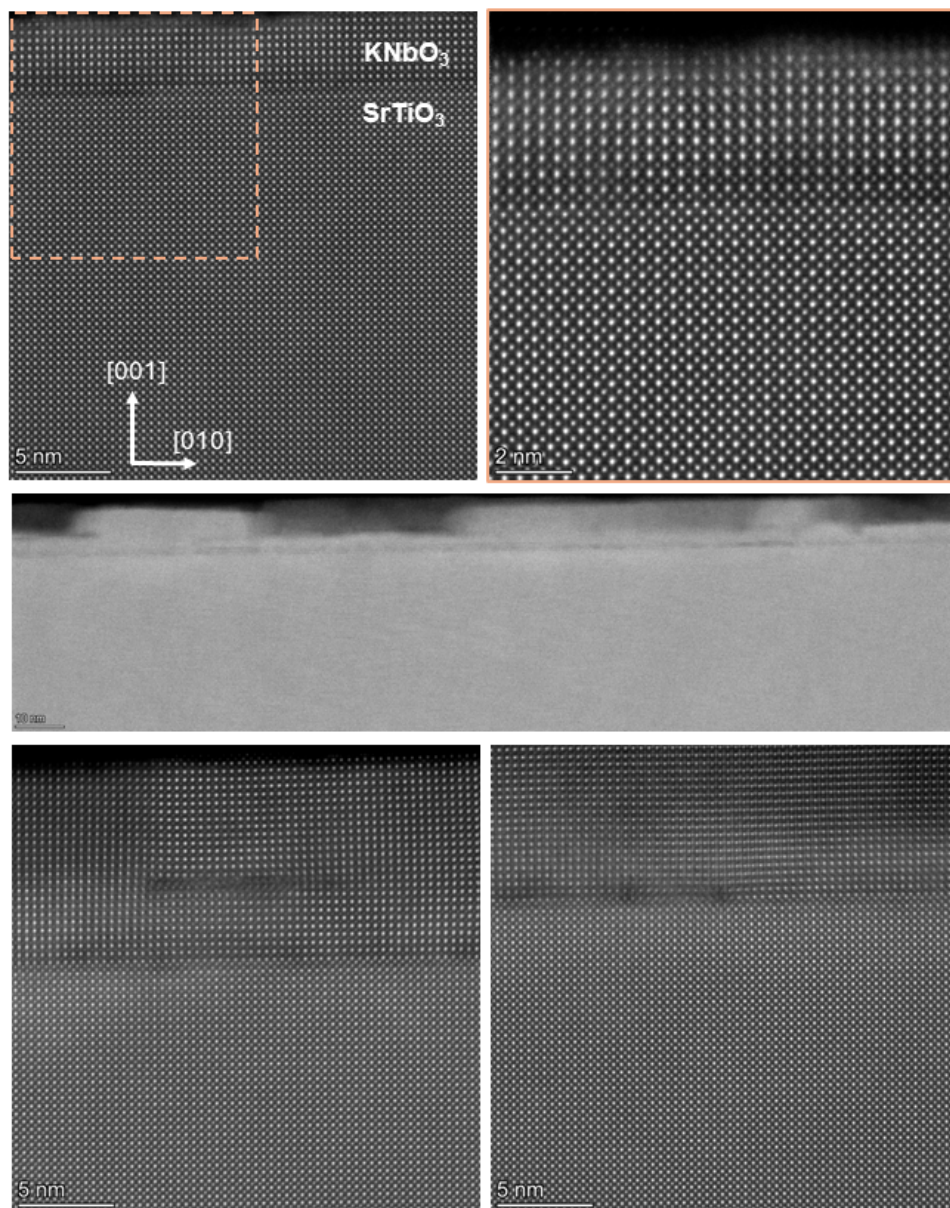


**Figure S10:** HAADF-STEM images of KNbO<sub>3</sub> thin film grown on SrTiO<sub>3</sub> substrate. The high-magnification images reveal small regions where the film has grown uniformly and without defects on the substrate, indicating localized areas of successful epitaxial growth. However, the larger area images indicate that both the interface and the film contain a high density of defects. The significant lattice mismatch between film and SrTiO<sub>3</sub> contributes to the presence of these defects. This large mismatch induces strain in the film, leading to dislocations, misfit dislocations, and other defects as the film attempts to relieve the strain. The high density of these defects disrupts the overall uniformity and coherence of the film. Due to the high density of defects, the film did not withstand the electron dose required for atomic resolution EDX mapping. The instability of the defective regions under the electron beam led to rapid degradation, preventing detailed chemical analysis. This behavior is typical in materials with high defect densities, where the structure is less robust under high-dose electron irradiation.

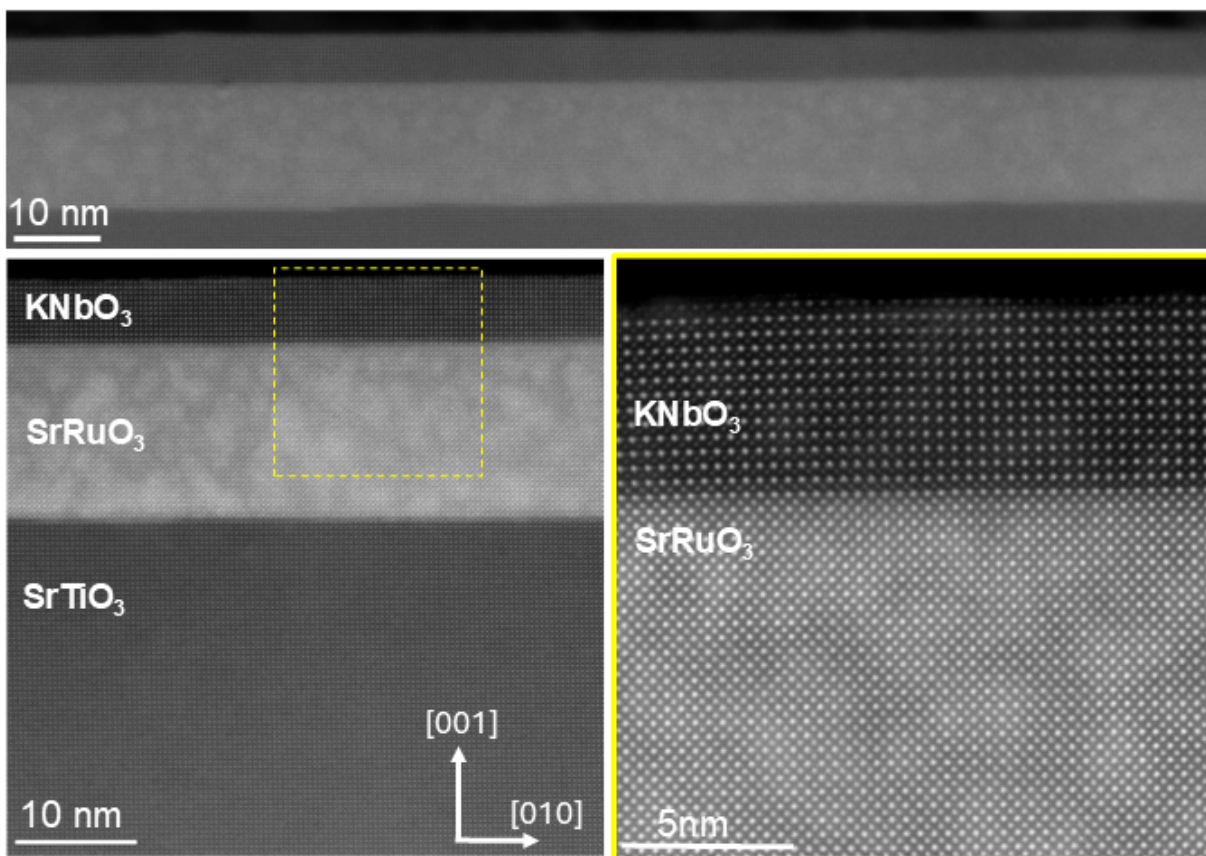


**Figure S11:** HAADF-STEM images of KNbO<sub>3</sub> thin film grown on SrTiO<sub>3</sub> substrate with a SrRuO<sub>3</sub> bottom electrode. Unlike KNbO<sub>3</sub> grown directly on SrTiO<sub>3</sub> substrate, with the introduction of a SrRuO<sub>3</sub> bottom electrode (15 nm thick) no extended defects are observed in the KNbO<sub>3</sub> film, which suggests high-quality epitaxial growth. The interface structure is uniform throughout the sample, indicating a coherent strain between the KNbO<sub>3</sub> film, SrRuO<sub>3</sub> bottom electrode and SrTiO<sub>3</sub> substrate. This suggests significant improvement in KNbO<sub>3</sub> thin film quality with the introduction of a SrRuO<sub>3</sub> bottom electrode.

## Note 7: X-ray photoelectron spectroscopy (XPS)

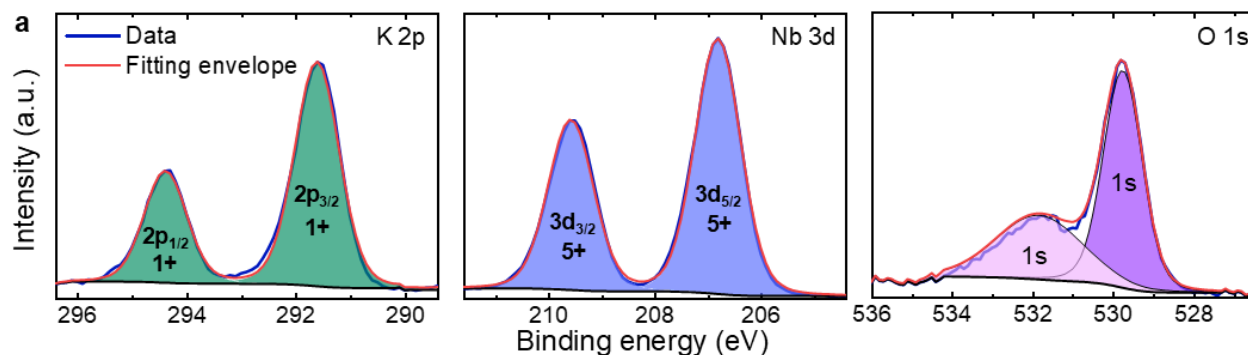


**Figure S12:** XPS spectra of KNbO<sub>3</sub> thin film done on KNbO<sub>3</sub>/SrRuO<sub>3</sub>/SrTiO<sub>3</sub> sample corresponding to (a) K 2p (b) Nb 3d and (c) O 1s core levels.

X-ray photoelectron spectroscopy (XPS) was done on KNbO<sub>3</sub>/SrRuO<sub>3</sub>/SrTiO<sub>3</sub> to confirm the valence state of the elements in KNbO<sub>3</sub> films. The spectra show two peaks at 291.6 eV and 294.3 eV respectively corresponding to K 2p<sub>3/2</sub> and K 2p<sub>1/2</sub> respectively confirming the +1 oxidation of K<sup>[15,16]</sup>. The Nb peaks corresponding to Nb 3d<sub>5/2</sub> and Nb 3d<sub>3/2</sub> levels are observed at 206.7 eV and 209.4 eV which are associated with +5 oxidation state of Nb<sup>[15,17]</sup>. The O 1s peak at 529.8 eV is attributed to -2 oxidation state of O. A smaller shoulder peak is also observed at 531.7 eV which is associated to surface bound hydroxyl groups (-OH)<sup>[15]</sup>.

## Note 8: Derivation of Optical Second Harmonic Generation (SHG) polarimetry expressions for the tetragonal and monoclinic phases

A schematic of the SHG setup is shown in **Figure 2a** of the main text. The lab coordinates (X, Y, Z) attached to the direction of the incoming beam: X || *p* polarization, Y || *s* polarization, where *p* and *s* are defined by a rotating half wave plate as labelled in **Figure 2a**. The crystal axes coordinate *i* = (1,2,3) are attached to the sample and related to the substrate as follows:

For GdScO<sub>3</sub> and DyScO<sub>3</sub> substrates: 1 || [001]<sub>o</sub>, 2 || [1-10]<sub>o</sub>, 3 || [110]<sub>o</sub>, where subscript “o” refers to orthorhombic unit cell of the scandate substrates.

For SrTiO<sub>3</sub> substrate: 1 || [100], 2 || [010], 3 || [001].

In lab coordinates (X, Y, Z), the electric field of the incident beam can be written as ( $E_o \cos \varphi$ ,  $E_o \sin \varphi$ , 0) where  $\varphi$  is the polarization rotation angle introduced by the half wave plate as shown in **Figure 2a**. For an incidence angle  $\theta$  on the sample (see **Figure 2a**), the electric field in the crystal axes coordinates can be expressed as ( $E_o \cos \varphi \cos \theta$ ,  $E_o \sin \varphi$ ,  $-E_o \cos \varphi \sin \theta$ ). The induced nonlinear polarization  $P^{2\omega}$ , is related to the incident electric field through the nonlinear susceptibility tensor,  $d_{ijk}$  through the following equation:

$$P_i^{2\omega} \propto d_{ijk} E_j^\omega E_k^\omega \quad (1)$$

The proportionality constants depend on incident beam fluence, Fresnel’s coefficients at the film-air and film-substrate interfaces and the thickness of the films.

### Tetragonal model:

For tetragonal unit cell the nonlinear susceptibility can be written in Voigt notation as:

$$\begin{pmatrix} 0 & 0 & 0 & 0 & d_{15} & 0 \\ 0 & 0 & 0 & d_{15} & 0 & 0 \\ d_{31} & d_{31} & d_{33} & 0 & 0 & 0 \end{pmatrix}$$

The induced nonlinear polarization in the crystal coordinates *i* = (1,2,3) (calculated through equation 1) can be rotated back to lab coordinates (X, Y, Z), to give the *p* and *s*-polarized components of the SHG (*p* || X and *s* || Y). The *p* and *s*-polarized SHG intensities can be expressed as follows:

For normal incidence ( $\theta = 0^\circ$ )

$$I_p^{2\omega} \propto (P_p^{2\omega})^2 = 0$$

$$I_s^{2\omega} \propto (P_s^{2\omega})^2 = 0$$

For oblique incidence ( $\theta = 45^\circ$ )

$$I_p^{2\omega} \propto (P_p^{2\omega})^2 \propto ((2d_{15} - d_{31} - d_{33})\cos[\varphi]^2 - 2d_{31}\sin[\varphi]^2)^2 \quad (2)$$

$$I_s^{2\omega} \propto (P_s^{2\omega})^2 \propto d_{15}^2 \sin[2\varphi]^2$$

**Figure S13** and upper panel of main text **Figure 2b** show the tetragonal model fitting for KNbO<sub>3</sub> on SrTiO<sub>3</sub> (10K and 300K), KNbO<sub>3</sub> on DyScO<sub>3</sub> (300K) and KNbO<sub>3</sub> on GdScO<sub>3</sub> (300K)

### Monoclinic model:

For the low temperature monoclinic phase ( $M_c$ ) in KNbO<sub>3</sub>, a multi-domain model is assumed consistent with X-ray measurements and phase field theory simulations. In crystal physics coordinates  $i = (1, 2, 3)$ , nonlinear susceptibility in the monoclinic phase can be written as:

$$d_{ij} = \begin{pmatrix} d_{11} & d_{12} & d_{13} & 0 & d_{15} & 0 \\ 0 & 0 & 0 & d_{24} & 0 & d_{26} \\ d_{31} & d_{32} & d_{33} & 0 & d_{35} & 0 \end{pmatrix}$$

Here, the monoclinic mirror plane is perpendicular to the crystallographic  $b$ -axis of the monoclinic cell of KNbO<sub>3</sub> which is parallel to  $i=2$  crystal physics coordinate. Through rotating the unit cell by right angles, 4 such unit cells can be achieved, each associated with an area fraction labelled as below:

- Domain 1:  $a \parallel 1, b \parallel 2, c \parallel 3$  (Area fraction:  $A_1$ )
- Domain 2:  $a \parallel 2, b \parallel -1, c \parallel 3$  (Area fraction:  $A_2$ )
- Domain 3:  $a \parallel -1, b \parallel -2, c \parallel 3$  (Area fraction:  $A_3$ )
- Domain 4:  $a \parallel -2, b \parallel 1, c \parallel 3$  (Area fraction:  $A_4$ )

Here  $(a, b, c)$  denote the crystallographic axes of the monoclinic unit cell,  $i = (1,2,3)$  denote the previously defined crystal physics coordinate system and the area fractions are constrained to  $A_1 + A_2 + A_3 + A_4 = 1$ .

For normal incidence ( $\theta = 0^\circ$ )

From Equation 1, the induced nonlinear polarization can be calculated in the crystal coordinate system and can be transformed into lab coordinates (X, Y, Z). The resultant nonlinear polarization in the lab coordinates X ( $p$ -polarized) and Y ( $s$ -polarized) are tabulated below (Table S5):

**Table S5:  $p$  and  $s$ -polarization components for different domains**

	$P_p^{2\omega}$	$P_s^{2\omega}$
Domain 1	$d_{11}\cos^2 \varphi + d_{12}\sin^2 \varphi$	$d_{26}\sin 2\varphi$
Domain 2	$d_{26}\sin 2\varphi$	$d_{12}\cos^2 \varphi + d_{11}\sin^2 \varphi$
Domain 3	$-(d_{11}\cos^2 \varphi + d_{12}\sin^2 \varphi)$	$-d_{26}\sin 2\varphi$
Domain 4	$-d_{26}\sin 2\varphi$	$-(d_{12}\cos^2 \varphi + d_{11}\sin^2 \varphi)$

The effective SHG intensity can be calculated as follows:

$$I_p^{2\omega} \propto (P_p^{2\omega})^2 \propto (A_1 P_{p, \text{domain } 1}^{2\omega} + A_2 P_{p, \text{domain } 2}^{2\omega} + A_3 P_{p, \text{domain } 3}^{2\omega} + A_4 P_{p, \text{domain } 4}^{2\omega})^2$$

This can be simplified to:

$$I_p^{2\omega} \propto K_{1p} (\sin^2 \varphi + K_{2p} \cos^2 \varphi)^2 + K_{3p} \sin^2 2\varphi + K_{4p} (\sin^2 \varphi + K_{2p} \cos^2 \varphi) \sin 2\varphi \quad (3)$$

where,

$$K_{1p} = \delta A_1^2 d_{12}^2 \quad K_{2p} = \frac{d_{11}}{d_{12}} \quad K_{3p} = \delta A_2^2 d_{26}^2 \quad K_{4p} = 2\delta A_1 \delta A_2 d_{12} d_{26}$$

$\delta A_1 = A_1 - A_3$  and  $\delta A_2 = A_2 - A_4$ . Similar expressions can also be derived for  $I_s^{2\omega}$  with the following coefficients:

$$K_{1s} = \delta A_2^2 d_{11}^2 \quad K_{2s} = \frac{d_{12}}{d_{11}} \quad K_{3s} = \delta A_1^2 d_{26}^2 \quad K_{4s} = 2\delta A_1 \delta A_2 d_{11} d_{26}$$

Similar expression has also been shown earlier for multidomain *mm2* model in epitaxial thin films [18,19]. **Figure S14** shows the normal incidence polarimetry for KNbO<sub>3</sub> on GdScO<sub>3</sub> and DyScO<sub>3</sub> at 10 K fitted to a multidomain monoclinic model.

For oblique incidence ( $\theta = 45^\circ$ ):

Equations for oblique incidence polarimetry involve more convoluted combinations of *d*-coefficients and area fractions, however they can be reduced to the same form as equation (3). The exact convolutions are listed below:

$$K_{1p} = \frac{1}{8} [2(A_1 + A_3)d_{32} + 2\delta A_1 d_{12} + 2d_{31}(A_2 + A_4)]^2$$

$$K_{2p} = \frac{1}{2\sqrt{2}K_{1p}} [\delta A_1(d_{11} + d_{13} - 2d_{35}) + (A_1 + A_3)(d_{31} + d_{33} - 2d_{15}) + (A_2 + A_4)(d_{32} + d_{33} - 2d_{24})]$$

$$K_{3p} = \frac{[\delta A_2(d_{26} - d_{35})]^2}{4}$$

$$K_{4p} = 2\sqrt{K_{1p}K_{3p}}$$

$$K_{1s} = \frac{1}{4} (A_2 - A_4)^2 d_{11}^2$$

$$K_{2s} = \frac{1}{2\sqrt{K_{1s}}} (d_{12} + d_{13})(A_2 - A_4)$$

$$K_{3s} = \frac{1}{4} \left( \sqrt{2}A_1(d_{26} - d_{24}) - \sqrt{2}A_3(d_{26} + d_{24}) + \frac{d_{15}}{\sqrt{2}}(A_4 - A_2) \right)^2$$

$$K_{4s} = 2\sqrt{K_{1s}K_{3s}}$$

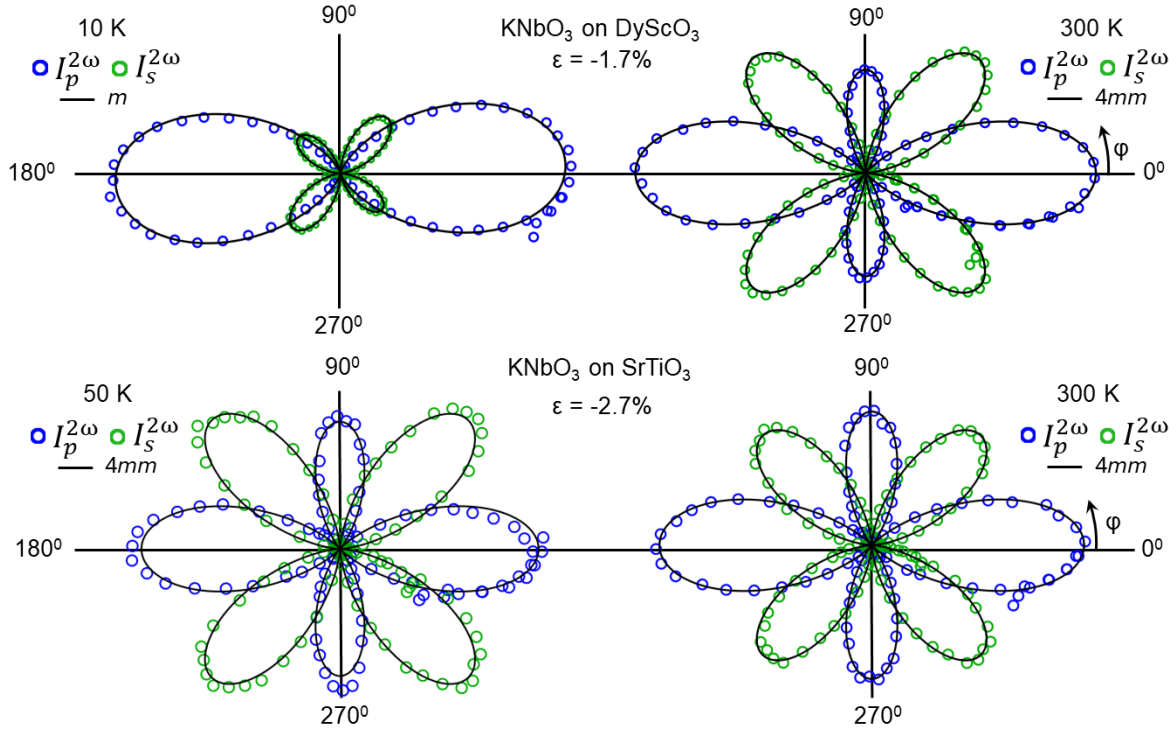


**Figure S13:** Oblique-incidence SHG polarimetry at  $T = 300$  K and  $T = 10$  K for  $\text{KNbO}_3$  film on  $\text{DyScO}_3$  and  $\text{SrTiO}_3$  substrates showing a tetragonal model fitting for both  $\text{KNbO}_3$  on  $\text{DyScO}_3$  and  $\text{SrTiO}_3$  at 300 K. While at 10 K, a multidomain monoclinic model is necessary for  $\text{KNbO}_3$  on  $\text{DyScO}_3$  but  $\text{KNbO}_3$  on  $\text{SrTiO}_3$  can still be fitted with a tetragonal model similar to 300 K.

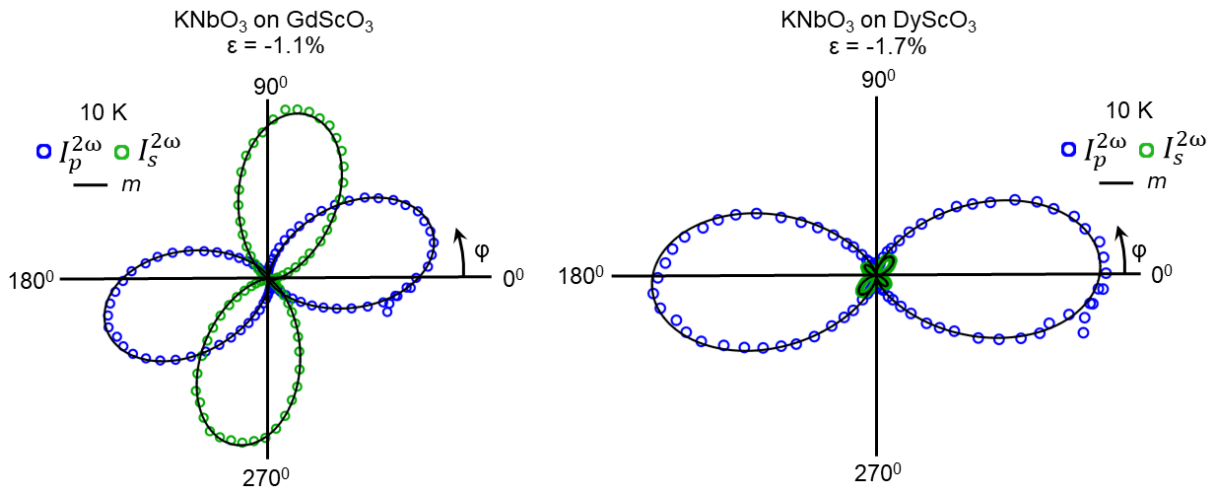


**Figure: S14:** Normal incidence SHG polarimetry at  $T = 10$  K for  $\text{KNbO}_3$  on  $\text{DyScO}_3$  and  $\text{GdScO}_3$  fitted to multidomain monoclinic model.

## Note 9: High temperature decomposition of $\text{KNbO}_3$ on $\text{GdScO}_3$ film measured by SHG

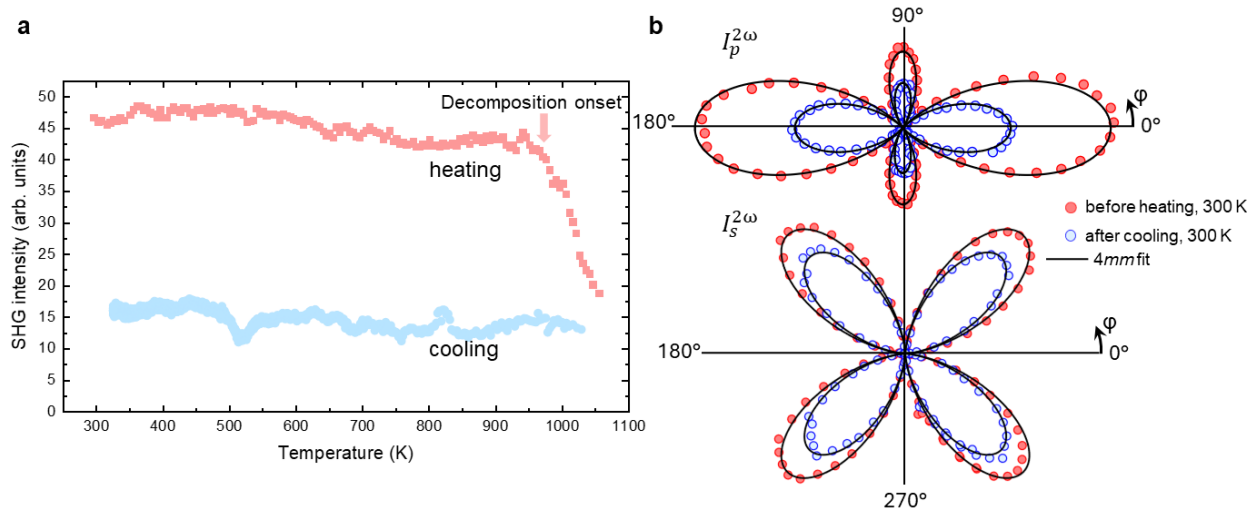


**Figure S15:** a) SHG intensity vs temperature in the high temperature regime for  $\text{KNbO}_3$  on  $\text{GdScO}_3$ . On heating the sample shows irreversible degradation around 975 K, while cooling run shows steady SHG intensity down to room temperature. b) SHG polarimetry at room temperature before starting heating compared to after cooling back down for  $p$ -polarized (upper panel) and  $s$ -polarized (lower panel) SHG. SHG polarimetry before heating and after cooling down can both be fitted to a  $4mm$  model showing the same symmetry, indicating that the only change occurring is in the intensity.

## Note 10: Calculation of Nonlinear optical coefficients in tetragonal and monoclinic symmetry

### Room temperature tetragonal:

#SHAARP.ml<sup>[20]</sup> package was used to characterize the nonlinear optical coefficients of KNbO<sub>3</sub> thin films on different substrates. The measurement geometry is shown in **Figure 2a** of the main text.

The linear optical properties were first characterized via ellipsometry, and x-ray reflectivity was used to measure the thickness of the films. These values are tabulated below in **Table S6** for both the film and substrate, which also serve as the input parameters for the #SHAARP.ml package.

Layer	$n$ (400 nm)	$n$ (800 nm)	Thickness
KNbO <sub>3</sub>	$2.565 + 0.107 i$	$2.260 + 0.110 i$	20.2 nm
GdScO <sub>3</sub>	$2.090 + 0.049 i$	$2.021 + 0.023 i$	Substrate

Layer	$n$ (400 nm)	$n$ (800 nm)	Thickness
KNbO <sub>3</sub>	$2.610 + 0.067 i$	$2.308 + 0.029 i$	17.5 nm
DyScO <sub>3</sub>	$2.084 + 0.068 i$	$2.016 + 0.032 i$	Substrate

Layer	$n$ (400 nm)	$n$ (800 nm)	Thickness
KNbO <sub>3</sub>	$2.419 + 0.046 i$	$2.163 + 0.006 i$	8.5 nm
SrTiO <sub>3</sub>	$2.678 + 0.064 i$	$2.350 + 0.021 i$	Substrate

**Table S6:** Complex refractive index coefficients and thickness values of KNbO<sub>3</sub> thin films on GdScO<sub>3</sub>, DyScO<sub>3</sub> and SrTiO<sub>3</sub> substrates.

Equations for SHG generated for KNbO<sub>3</sub> thin films on the different substrates are generated through the full multiple reflection assumptions in the #SHAARP.ml package, which considers multiple reflections in the two layers (thin film + substrate) for both the fundamental and second harmonic beams. By calibrating the SHG generated from the thin films to a standard LiNbO<sub>3</sub> reference sample, full characterization of the SHG tensor is possible.

For tetragonal unit cell the SHG tensor can be written in Voigt notation as:

$$\begin{pmatrix} 0 & 0 & 0 & 0 & d_{15} & 0 \\ 0 & 0 & 0 & d_{15} & 0 & 0 \\ d_{31} & d_{31} & d_{33} & 0 & 0 & 0 \end{pmatrix}$$

Simultaneous fitting of p-polarized generated SHG for 30°, 45°, 60° incidence angle gives the  $d_{33}/d_{15}$  and  $d_{31}/d_{15}$  ratios. The s-polarized SHG generated from the sample depends only on the  $d_{15}$  coefficient and can be calibrated to LiNbO<sub>3</sub>.

The general form of p and s-polarized SHG for any angle and sample can be written as:

$$I_p^{2\omega} \propto [(A_{1p}d_{15} + A_{2p}d_{31} + A_{3p}d_{33})\cos[\varphi]^2 + A_{4p}d_{31}\sin[\varphi]^2] \times [cc]$$

$$I_s^{2\omega} \propto [A_{1s}d_{15}\sin[2\varphi]] \times [cc]$$

The coefficients are detailed in the following table corresponding to each sample and measurement angle.

Film	Angle	$A_{1p}$	$A_{2p}$	$A_{3p}$	$A_{4p}$	$A_{1s}$
KNbO <sub>3</sub> on GdScO <sub>3</sub>	30°	-5.7 + 9.6 <i>i</i>	1.7 - 3.8 <i>i</i>	0.1 - 0.2 <i>i</i>	1.7 - 3.7 <i>i</i>	
	45°	12.2 - 14.4 <i>i</i>	-3.9 + 6.1 <i>i</i>	-0.3 + 0.7 <i>i</i>	-3.6 + 5.4 <i>i</i>	-11.1 - 12.1 <i>i</i>
	60°	7.7 - 14.9 <i>i</i>	-2.3 + 5.9 <i>i</i>	-0.2 + 1.0 <i>i</i>	-2.0 + 4.5 <i>i</i>	
KNbO <sub>3</sub> on DyScO <sub>3</sub>	30°	-8.4 + 9.1 <i>i</i>	2.5 - 3.8 <i>i</i>	0.1 - 0.1 <i>i</i>	2.5 - 3.7 <i>i</i>	
	45°	11.0 - 12.8 <i>i</i>	-3.3 + 5.2 <i>i</i>	-0.3 + 0.5 <i>i</i>	-3.2 + 4.8 <i>i</i>	-10.3 - 10.8 <i>i</i>
	60°	11.5 - 14.6 <i>i</i>	-3.5 + 5.9 <i>i</i>	-0.5 + 0.9 <i>i</i>	-3.0 + 4.6 <i>i</i>	
KNbO <sub>3</sub> on SrTiO <sub>3</sub>	30°	-1.7 + 6.5 <i>i</i>	0.9 - 3.1 <i>i</i>	0.0 - 0.1 <i>i</i>	0.8 - 3.0 <i>i</i>	
	45°	2.3 - 9.0 <i>i</i>	-1.2 + 4.3 <i>i</i>	-0.1 + 0.5 <i>i</i>	-1.0 + 3.8 <i>i</i>	-0.3 - 2.5 <i>i</i>
	60°	2.7 - 10.1 <i>i</i>	-1.3 + 4.8 <i>i</i>	-0.2 + 0.9 <i>i</i>	-0.9 + 3.5 <i>i</i>	

**Table S7:**  $A_{1p}$ ,  $A_{2p}$ ,  $A_{3p}$ ,  $A_{4p}$  and  $A_{1s}$  coefficients corresponding to all three strained films corresponding to  $I_p^{2\omega}$  and  $I_s^{2\omega}$  equations.

The resulting SHG coefficients are tabulated below:

Film	$d_{15}$ (pm/V)	$d_{31}$ (pm/V)	$d_{33}$ (pm/V)
KNbO <sub>3</sub> on SrTiO <sub>3</sub>	49 ± 1	44 ± 1	59 ± 1
KNbO <sub>3</sub> on DyScO <sub>3</sub>	37 ± 1	31 ± 1	41 ± 1
KNbO <sub>3</sub> on GdScO <sub>3</sub>	32 ± 1	32 ± 1	51 ± 1

**Table S8:**  $d_{15}$ ,  $d_{31}$ ,  $d_{33}$  SHG tensor coefficients of room temperature tetragonal phase of KNbO<sub>3</sub> corresponding to all three strained films.

**Note 11: Temperature dependent reciprocal space mapping of KNbO<sub>3</sub> on GdScO<sub>3</sub>**

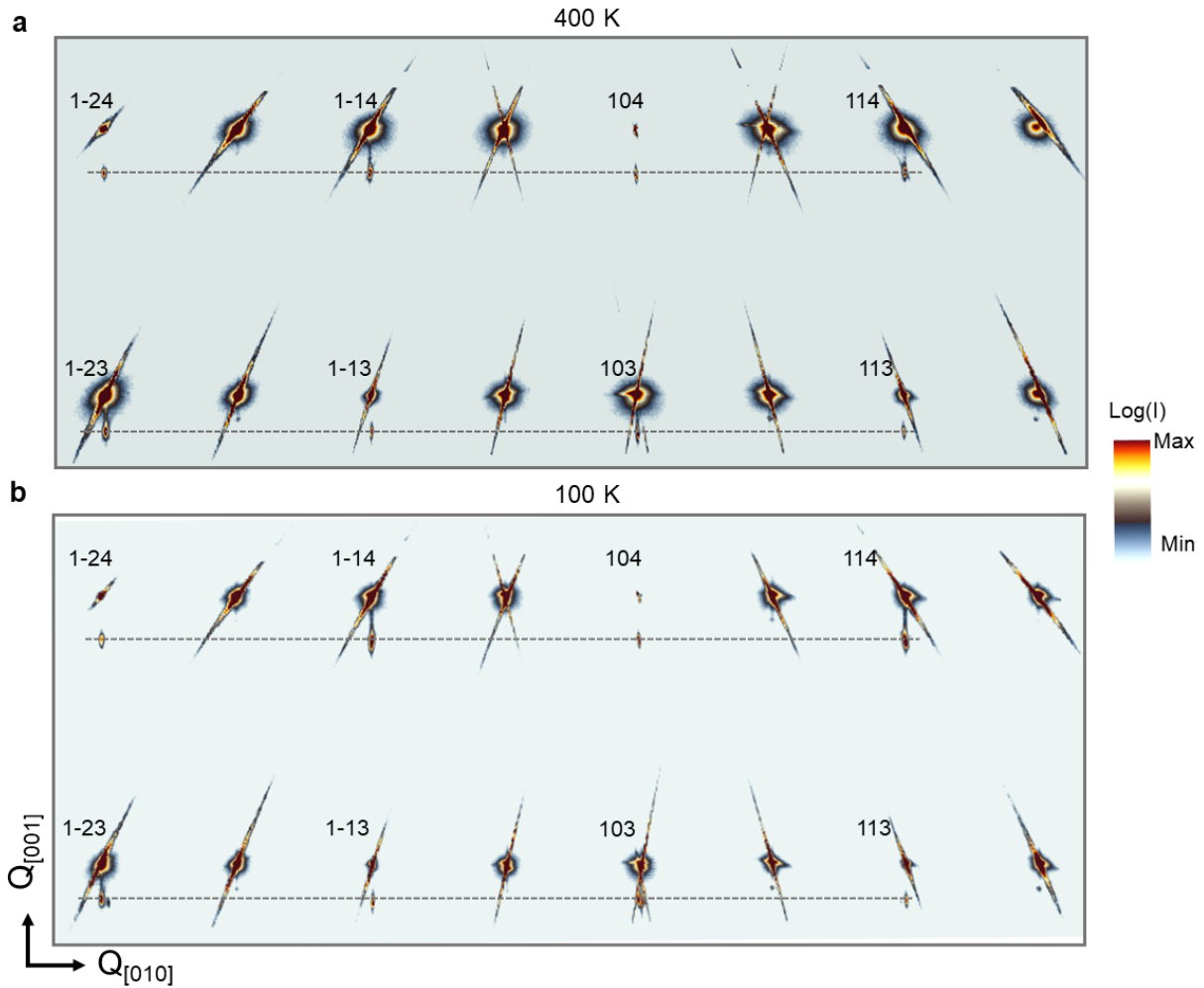


**Figure S16:** Reciprocal space maps (RSM) capturing the effect of temperature on KNbO<sub>3</sub> film structures relative to the GdScO<sub>3</sub> substrate. The maps at 400 K (a) and 100 K (b) correspond to temperatures above and below the tetragonal to monoclinic phase transition (275 K) respectively. The pseudocubic Miller indices of several off-specular substrate peaks are marked in inset. Horizontal dotted lines mark the position of the film peaks relative to each other and the substrate peaks. The film peak alignment along the horizontal [010]-direction indicates that the peak shifts relative to the substrate are only dependent on  $Q_{001}$  and do not depend on the Miller indices of the substrate. This supports strain as the dominating factor for peak position – signifying the average tetragonal structure of the film at both 100 K and 400 K, while the additional occurrence (See **Figure 3b**) of the tilted satellite peaks at 100 K along the  $\langle 110 \rangle$  direction signify the monoclinic distortion at low temperature.

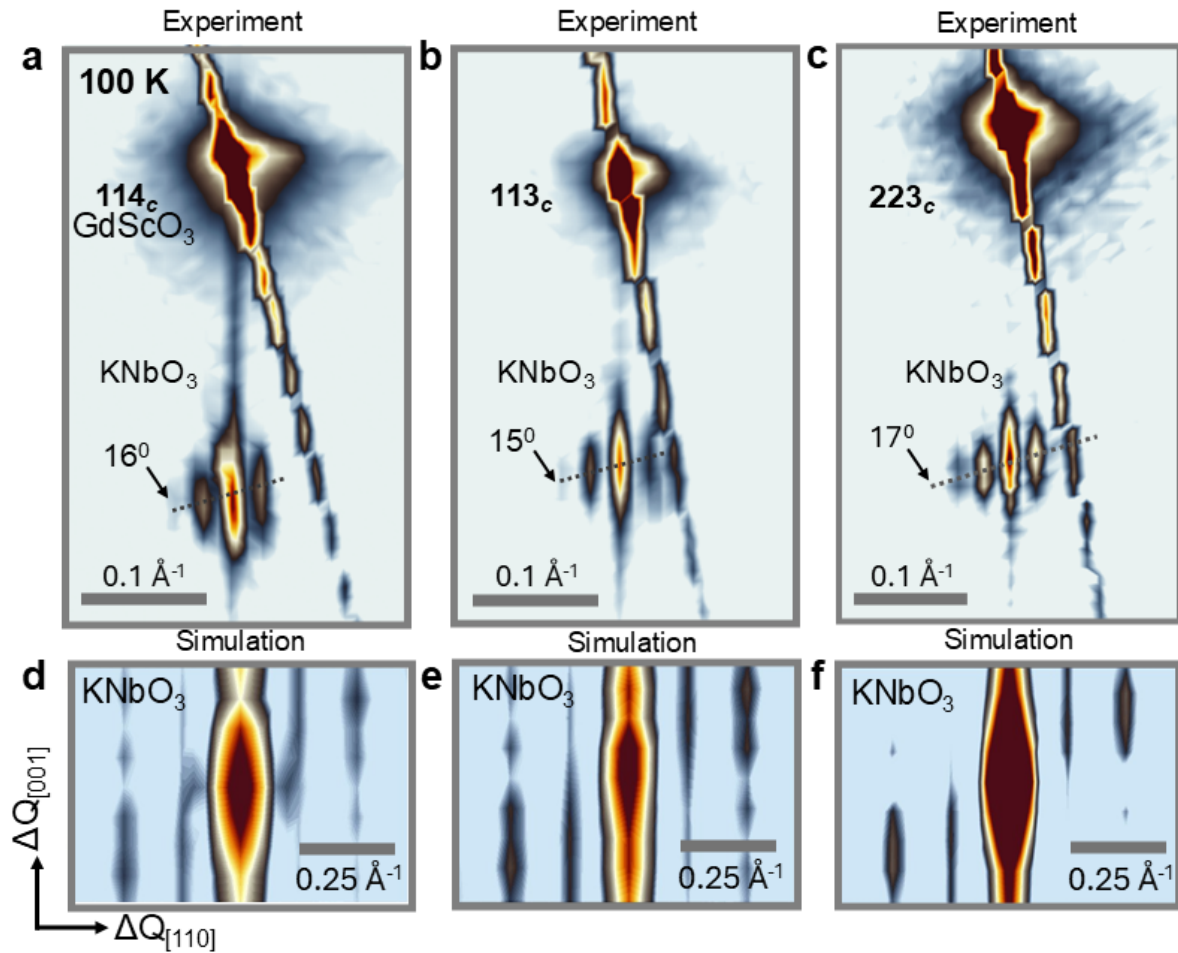


**Figure S17:** Experimentally measured RSM images around different GdScO<sub>3</sub> Bragg peaks (**a**: 114<sub>c</sub>, **b**: 113<sub>c</sub>, **c**: 223<sub>c</sub>) at 100 K showing the tilt of diffused satellites due to tilted monoclinic domain walls. Diffraction simulations conducted on phase-field simulated microstructure at 100 K showing tilted diffused satellite peaks around corresponding KNbO<sub>3</sub> peaks measured experimentally (**d**: 114<sub>c</sub>, **e**: 113<sub>c</sub>, **f**: 223<sub>c</sub>).

**Note 12: Structural characterization of KNbO<sub>3</sub> thin films with SrRuO<sub>3</sub> bottom electrodes**

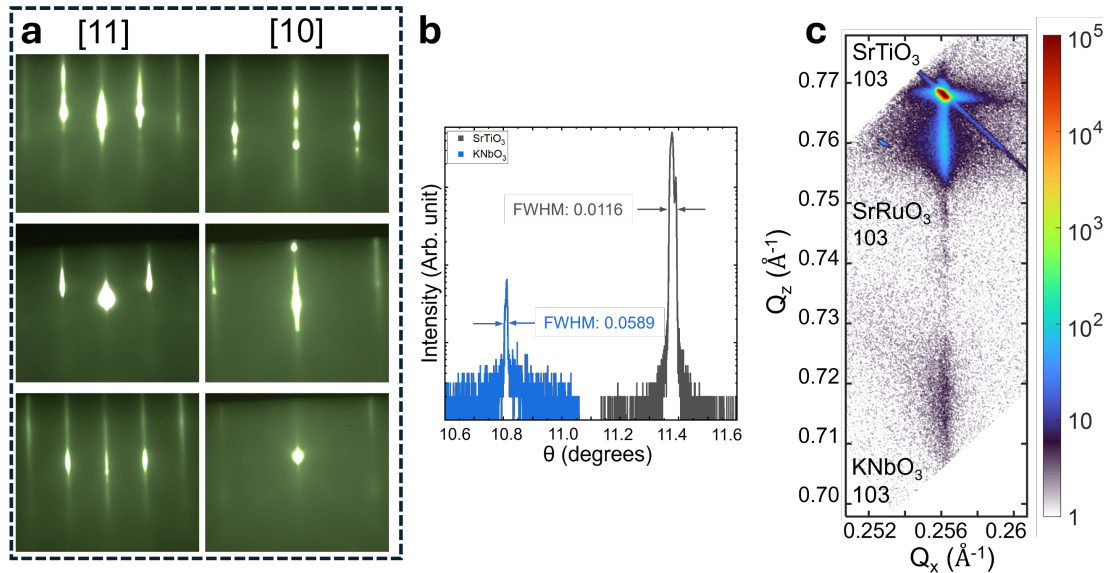


**Figure S18:** Structural characterization of a 19.8 nm thick KNbO<sub>3</sub>/SrRuO<sub>3</sub>/SrTiO<sub>3</sub>. (a) RHEED patterns of the bare SrTiO<sub>3</sub> 001 substrate (top), SrRuO<sub>3</sub> 001 bottom electrode (middle) and the KNbO<sub>3</sub> film (bottom). (b) Overlaid 001 SrTiO<sub>3</sub> and 001 KNbO<sub>3</sub> peaks showing comparable FWHM values. (c) RSM of the KNbO<sub>3</sub>/SrRuO<sub>3</sub>/SrTiO<sub>3</sub> heterostructure indicating that both the bottom electrode and the KNbO<sub>3</sub> film are commensurately strained to the substrate.

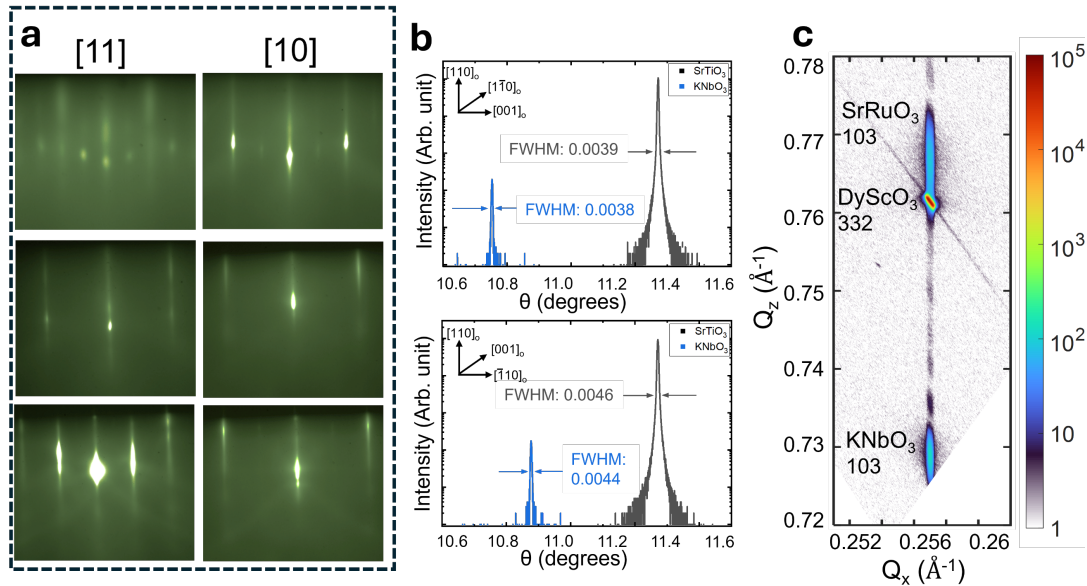


**Figure S19:** 21.8 nm-thick KNbO<sub>3</sub>/SrRuO<sub>3</sub>/DyScO<sub>3</sub> (a) RHEED patterns of the bare SrTiO<sub>3</sub> 001 substrate (top), SrRuO<sub>3</sub> 001 bottom electrode (middle) and the KNbO<sub>3</sub> film (bottom). (b) Overlaid 110 DyScO<sub>3</sub> and 001 KNbO<sub>3</sub> peaks showing comparable FWHM values. (c) RSM of the KNbO<sub>3</sub>/SrRuO<sub>3</sub>/DyScO<sub>3</sub> heterostructure indicating that both the bottom electrode and the KNbO<sub>3</sub> film are commensurately strained to the substrate

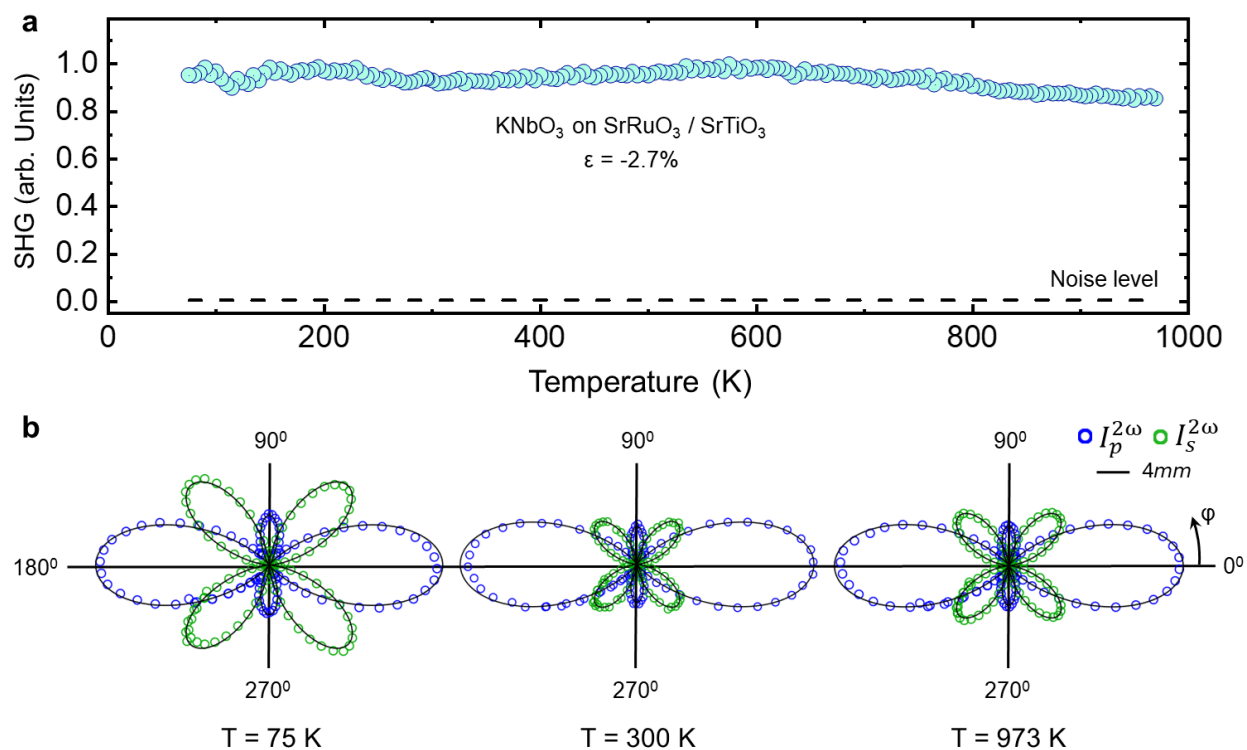


**Figure S20: a)** Temperature dependent SHG intensity of KNbO<sub>3</sub>/SrRuO<sub>3</sub>/SrTiO<sub>3</sub> sample showing absence of any structural phase transitions and  $T_c$  pushed above 975 K consistent with phase-field simulations and SHG measurements on KNbO<sub>3</sub> films without bottom electrode. **b)** SHG polarimetry done at 75 K, 300 K and 973 K fitted to tetragonal  $4mm$  with out-of-plane polarization direction

### Note 13: Electrical characterization of polarization switching in strained $\text{KNbO}_3$

**Figure S21a** shows the PFM switching spectroscopy measured on the free surface of  $\text{KNbO}_3/\text{SrRuO}_3/\text{DyScO}_3$  suggesting a strong upward built-in field. The relaxation measurement in **Figure S21b** suggests that the downward state can be maintained for only  $\sim 10$  ms, making polarization preferentially in the upward single domain state for the as-grown films. **Figure S21c** is the PFM switching spectroscopy on the free surface of  $\text{KNbO}_3/\text{SrRuO}_3/\text{SrTiO}_3$  with a strong upward built-in field leading to both coercive voltages positive, an indication that only upward polarization can be maintained.

**Figure S22a** shows the raw PUND data of the applied voltage and the recorded current from the capacitors, where high leakage is observed for the positive voltages, while much lower leakage is recorded for the negative voltages and the switching current peak can be extracted. **Figure S22b** displays the extracted switching peaks from the PUND measurements with various voltage pulse amplitudes from 3 V to 5.5 V. The calculated  $2P_r$  values are shown in **Figure S22c**, which show a linear increase over the pulse amplitudes suggesting that there is an additional leakage contribution during the polarization switching process which is not subtracted from the PUND non-switching contributions (capacitive current and steady state leakage). Additional testing shows that 3 V of pulse amplitude leads to incomplete switching, so that 4 V is used for the estimation of the upper limit of the remanent polarization value. **Figure S22d** shows a PFM measurement for the polarization relaxation from the downward to upward state after a pulse of 3 V to set the initial state into downward. The PFM phase relaxed from  $\sim 0^\circ$  (corresponding to downward state) to  $\sim 180^\circ$  (corresponding to upward state) in about 10 s. **Figure S22e** shows an  $I$ - $V$  measurement after the capacitor is set to the downward state with 4 V pulse. The first cycle starting with negative voltages shows no switching, suggesting that polarization is relaxed back to upward with a  $\sim 30$  s delay time. **Figure S22f** is an AFM topography image of the  $5 \times 5 \mu\text{m}^2$  top electrode for the capacitors under investigation.

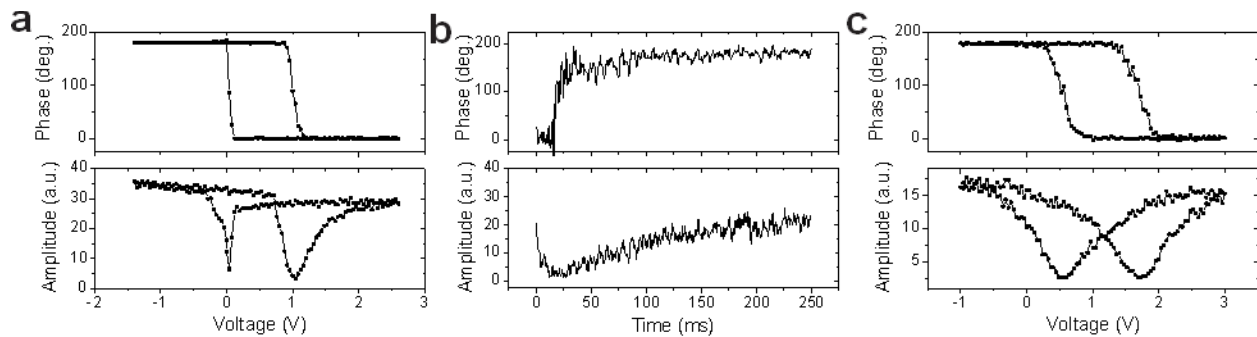


**Figure S21.** PFM switching spectroscopy and relaxation measurements on the free surface of  $\text{KNbO}_3$  thin films. (a) PFM switching spectroscopy on the 21.8 nm-thick  $\text{KNbO}_3/\text{SrRuO}_3/\text{DyScO}_3$  shows a strong upward built-in field that makes polarization down very unstable. (b) PFM measurement of the polarization relaxation of the downward state after a 4 V pulse shows polarization downward relaxes back to upward in 10–20 ms. (c) PFM switching spectroscopy on

the 19.8 nm thick  $\text{KNbO}_3/\text{SrRuO}_3/\text{SrTiO}_3$  shows a strong upward built-in field leading to both coercive voltages positive.

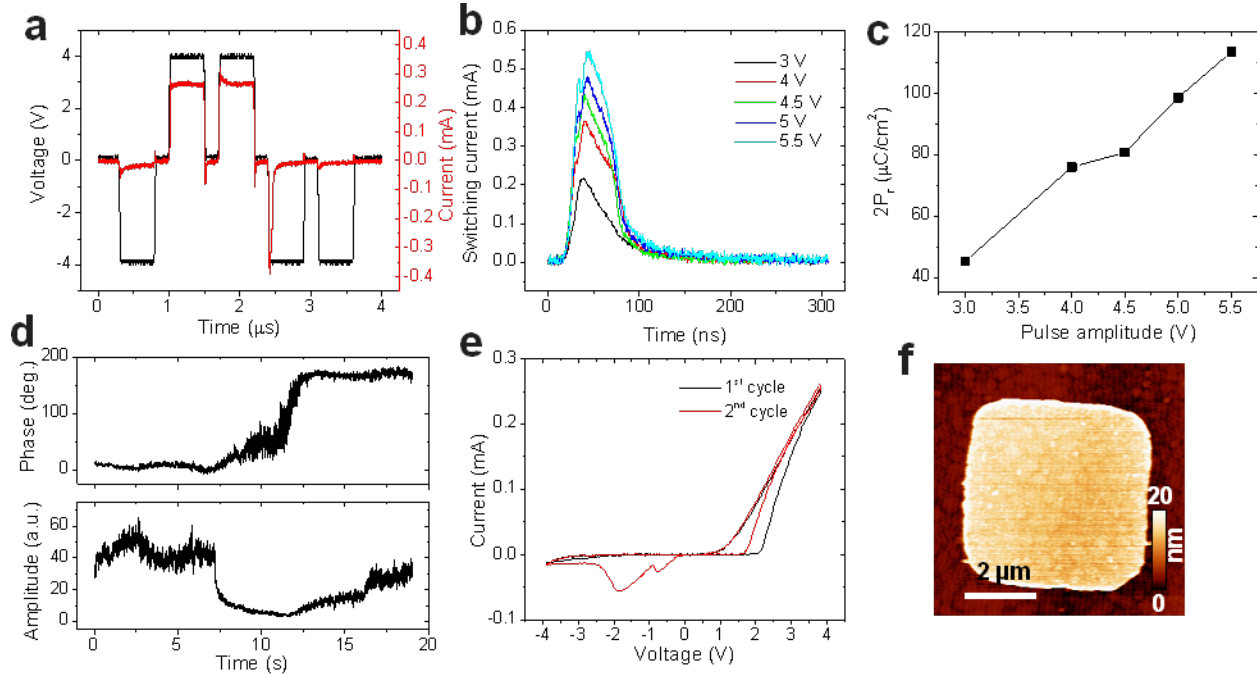


**Figure S22.** Electrical and PFM measurements on the Pt/KNbO<sub>3</sub>/SrRuO<sub>3</sub>/DyScO<sub>3</sub> capacitors. **(a)** Raw PUND data of the applied voltage and the recorded current from the capacitor shows high leakage current for the positive voltage, while much lower leakage is recorded on the negative voltages enabling the extraction of the switching current peak. **(b)** The switching current peaks from the PUND measurements at various voltage pulse amplitudes from 3 V to 5.5 V. **(c)** The calculated switching charges ( $2P_r$ ) from the PUND measurements in (b) shows a linear increase with the pulse amplitude, which indicates a dynamic leakage during the polarization switching process. **(d)** PFM measurement of the relaxation of the downward polarization state after a pulse of 3 V, 10 ms, which relaxes to the upward state in about 10 s. **(e)**  $I$ - $V$  measurement ~30 s after application of a 4 V pulse to set the initial polarization state downward, with a sweeping voltage from 0 V → -4 V → +4 V → 0 V and repeat again. The first cycle on the negative side shows no polarization switching, suggesting that polarization has been relaxed to the upward state during the 30 s delay, while the second cycle shows clear switching peaks on the negative side. **(f)** An AFM topography image of the 5×5 μm<sup>2</sup> top electrode.

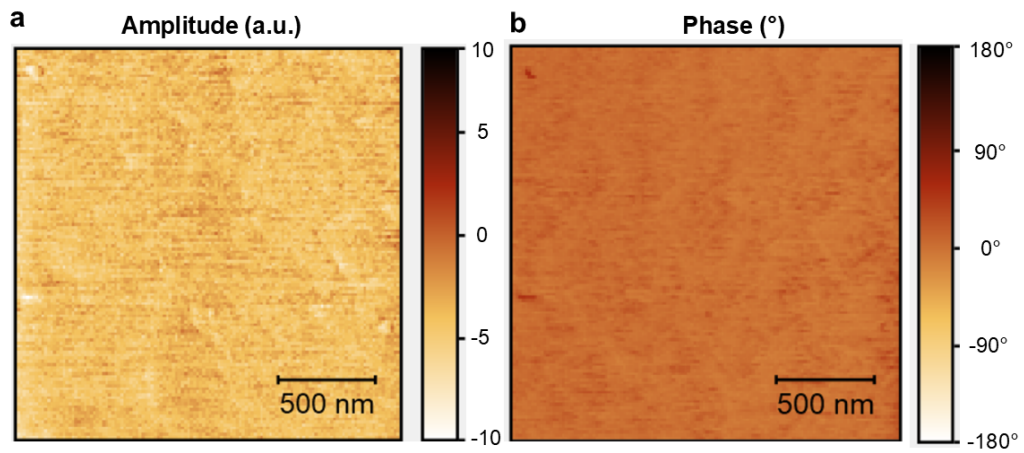


**Figure S23.** Room temperature piezoresponse force microscopy (PFM) maps across  $2 \times 2 \mu\text{m}^2$  region on  $\text{KNbO}_3/\text{SrRuO}_3/\text{DyScO}_3$  film showing no amplitude (a) and phase contrast (b) confirming the absence of  $180^\circ$  tetragonal domains.

## Note 14: Dielectric loss and electrical leakage characterization of KNbO<sub>3</sub> films

To investigate the dominant conduction mechanisms responsible for the rise in leakage current in KNbO<sub>3</sub> films, leakage current measurements were performed on 21.8 nm thick KNbO<sub>3</sub> films grown on DyScO<sub>3</sub> with a 15 nm thick SrRuO<sub>3</sub> bottom electrode, using a 4140 Pico-Ampere Meter/DC Voltage Source (Hewlett Packard). 100 nm thick Pt electrodes, which were lithographically patterned into 50  $\mu\text{m}$  x 50  $\mu\text{m}$  squares, were used as the top electrode.

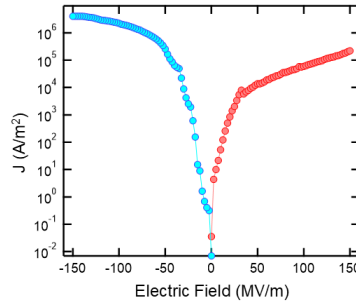


**Figure S24:** Polarity-dependent leakage current density ( $J$ ) with increasing applied electric field. The blue curve corresponds to the field-down configuration (bottom electrode negatively biased). The red curve corresponds to the field-up configuration (top electrode negative biased)

A noticeable difference in the leakage current behavior was observed for opposite polarities (**Figure S24**). The leakage current increases more significantly with applied voltage when the bottom electrode is negatively biased compared to the top electrode (field-down). Conversely, the current levels are lower when the top electrode is negatively biased (field-up). This is consistent with PFM measurements of switching current shown in **Main Text, Figure 4b**, and suggests a significant contribution of an *interface-controlled mechanism* in the observed asymmetry of the leakage current.

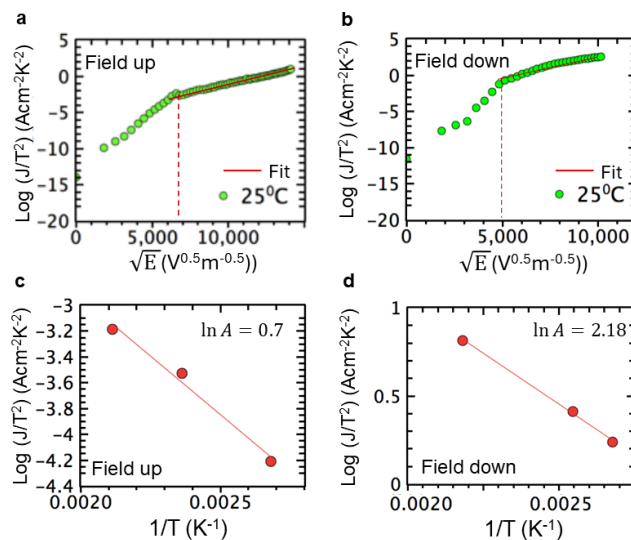


**Figure S25:** Current density vs electric field ( $\ln(J/T^2)$  versus  $E^{1/2}$ ) fitted to Equation 1 showing the onset of Schottky emission for field-up **(a)** and field-down **(b)** configurations. Estimation of Richardson constant ( $A$ ) from intercept of the  $\ln(J/T^2)$  versus  $1/T$  at a given field for field-up **(c)** and field-down **(d)** configurations.

To further investigate the leakage characteristics, the temperature dependent I-V data was fitted to equations representing various interface-controlled conduction mechanisms. The current density-electric field ( $J$ - $E$ ) characteristics in KNbO<sub>3</sub> display a good linearity consistent with Schottky emission ( $\ln(J/T^2)$  versus  $E^{1/2}$ ) for both polarities **(Figure S25a - b)**. The optical dielectric permittivity,  $\epsilon_r$ , was extracted from the slope of the linear fits, and the refractive index,  $n = \sqrt{\epsilon_r}$ , was calculated. The refractive index derived from the Schottky plots ranged from 2.2 to 2.9, which is in good agreement with the refractive index of KNbO<sub>3</sub> ( $n \approx 2.25$ )<sup>[21]</sup>. This suggests that interface dominated Schottky emission to be one of the dominant contributors of the leakage in these KNbO<sub>3</sub> films.

To estimate the Schottky barrier height, the Richardson constant,  $A$ , was first determined from the intercept of the  $\ln(J/T^2)$  versus  $1/T$  at a given field **(Figure S25c - d)**. Then, the Schottky barrier height ( $\Phi_B$ ) was extracted from the intercept of  $\ln(J/T^2)$  vs.  $E^{1/2}$  plot using the following equation:

$$\ln\left(\frac{J_{Sch}}{T^2}\right) = \ln A - \frac{q\Phi_B^{Sch}}{k_B T} + \frac{q\sqrt{\frac{qE}{4\epsilon_0\epsilon_\infty\pi}}}{k_B T} \quad \text{Equation 1}$$

where  $A$  is the Richardson constant,  $\epsilon_\infty$  is the high frequency permittivity,  $\Phi_B^{Sch}$  is the barrier height, and  $q$  is the charge per carrier.  $\Phi_B$  is estimated to be  $0.4 \pm 0.04$  eV for the top Pt/KNbO<sub>3</sub> interface and  $0.25 \pm 0.03$  eV for the bottom SrRuO<sub>3</sub>/KNbO<sub>3</sub> interface. The difference in  $\Phi_B$  is likely due to the difference in work function of top Pt (5.6 eV)<sup>[22]</sup> and bottom SrRuO<sub>3</sub> (5.2 eV)<sup>[23]</sup> electrodes. The higher work function of Pt results in a higher  $\Phi_B$ , which leads to lower leakage current levels under field-up conditions and contributes to the polarity-dependent leakage current behavior observed in KNbO<sub>3</sub> films. A schematic representation of the band bending in KNbO<sub>3</sub> at both interfaces is shown in **Figure S26**.

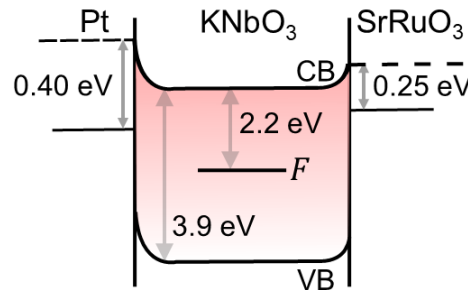


**Figure S26:** Schematic band diagram of KNbO<sub>3</sub> showing the measured Schottky barrier heights at both Pt-KNbO<sub>3</sub> and SrRuO<sub>3</sub>-KNbO<sub>3</sub> interfaces and known  $F$ -center (Oxygen-vacancy which traps electrons) energy level in KNbO<sub>3</sub><sup>[24,25]</sup>. The  $F$ -center energy level in KNbO<sub>3</sub> is deep due to its molecular orbital being primarily contributed by the two nearest Nb atoms from the oxygen vacancy<sup>[24]</sup>.

To further explore the charge transport mechanisms in the KNbO<sub>3</sub> film, temperature dependent modulus spectroscopy measurements were performed using a Solartron 1260 Impedance analyzer with a 100 mV AC amplitude, over a frequency range from 1 MHz to 0.01 Hz. **Figure S27** shows the frequency dependence of the imaginary part of the electric modulus ( $M''(f)$ ) of the measured the KNbO<sub>3</sub> film at temperatures ranging from 30°C to 200°C.

$M''(f)$  exhibits a maximum at the relaxation frequency,  $f(r)$ , which can indicate the volume fraction of material with similar conductivity. The relaxation frequency  $f(r)$  of the modulus peak is expressed as:

$$f(r) = \frac{1}{2\pi RC} = \frac{\sigma}{2\pi\epsilon_0\epsilon_r} \quad \text{Equation 2}$$

where  $\sigma$  is the conductivity,  $\epsilon_r$  is the relative permittivity, C is capacitance, and R is resistance.

The temperature dependence of the modulus peak was analyzed to determine the origin of the charge transport mechanism (**Figure S27a**). By fitting the conductivity calculated through Equation 2 to the Arrhenius equation, the activation energy related to dielectric relaxation associated with the observed modulus peak is calculated to be  $0.45 \pm 0.04$  eV (**Figure S27b**).

The exact mechanism responsible for such relaxation behavior is unknown. We speculate that this relaxation process is related to polaron hopping mechanism which has previously been observed in KNbO<sub>3</sub> single crystals [26,27]. Oxygen vacancies are one of the main sources of point defects in KNbO<sub>3</sub> which acts as electron donors. These electrons can be bound to Nb<sup>5+</sup> ion cation forming a polaron. Hopping of such polarons between symmetry equivalent sites results in increased conductivity.

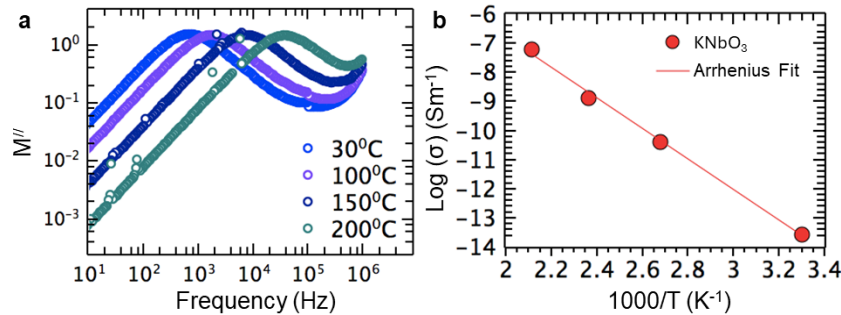


**Figure S27:** (a) Imaginary part of electric modulus ( $M''$ ) as a function of frequency showing a dielectric relaxation peak moving to higher frequencies with increasing temperature. (b)  $\sigma$  vs T curve ( $\text{Log} \sigma$  vs  $1000/T$ ) corresponding to the observed dielectric relaxation peak fitted to the Arrhenius equation.

### Origin of defects in KNbO<sub>3</sub>:

Potassium vacancies and oxygen vacancies are the primary point defects in KNbO<sub>3</sub>. Due to the high K vapor pressure, K vacancies form on high temperature exposure of KNbO<sub>3</sub>, including

during growth. Subsequently, this leads to oxygen vacancies, in order to maintain charge neutrality, as can be described in Kroger-Vink notation as follows:



Since these oxygen vacancies are necessary for charge neutrality, they are thermodynamically stable and cannot be removed via annealing. Localized hopping of such singly ionized oxygen vacancies can lead to dielectric relaxation [28]. A secondary pathway of forming oxygen vacancies is due to oxygen leaving lattice positions; these defects serve as electron donor defects, which can be expressed in Kroger-Vink notation as follows:



These electrons could be weakly bound to  $Nb^{5+}$  cations, forming dipoles giving rise to dielectric relaxation mechanisms in  $KNbO_3$  [28,29]. Oxygen vacancies in  $KNbO_3$  can also serve as electron trapping sites (*F*-centre) which produces deep energy levels,  $\sim 2.2$  eV below the conduction band [24] in  $KNbO_3$  (**Figure S26**). A high concentration of oxygen vacancies in  $KNbO_3$  films can also modulate the potential barrier height via Fermi level pinning, accelerating charge injection under DC electric fields. Consequently, the distribution of oxygen vacancies throughout the thickness of  $KNbO_3$  films can contribute to asymmetric leakage current characteristics and polarity-dependent lifetimes. Furthermore, oxygen vacancies can contribute to both electronic and ionic conductivity in  $KNbO_3$  films [28].

Finally, migration of  $K^+$  ions and oxygen vacancies, having activation energies of 0.6 eV and 1.2 eV, respectively, are another source of conduction (especially at high temperatures) which has been observed in  $KNbO_3$  single crystals [30]. The formation of conductive domain walls and pinholes across a thin film are also possible contributors to leakage in  $KNbO_3$  thin films.

Further investigations are necessary to understand the relative influence of different defect mechanisms involved in high leakage current levels in  $KNbO_3$  films.

### **Improving leakage characteristics of $KNbO_3$ :**

All said, the primary source of leakage and slower switching dynamics in  $KNbO_3$  is understood to be due to oxygen vacancies formed either due to K vacancy formation or O leaving lattice positions during material processing which contribute to the dielectric leakage properties of  $KNbO_3$ . A possible method to eradicate this is by growing  $KNbO_3/SrTiO_3$  superlattices. Superlattices on substrates on  $SrTiO_3$  or  $DyScO_3$  substrates, similar to the well-studied  $PbTiO_3/SrTiO_3$  superlattice system [31], will allow the growth of thicker films while maintaining coherent strain in  $KNbO_3$ . This will help eradicate mechanical sources of leakage such as pinhole formation in films. More importantly, in superlattice heterostructures,  $KNbO_3$  can be capped with a  $SrTiO_3$  layer, which will reduce the loss of K from the film. This in turn should significantly decrease oxygen vacancy

concentrations in the films leading to improved dielectric loss characteristics. Finally, doping the  $\text{KNbO}_3$  with a small amount of electron acceptors such as  $\text{Ba}^{2+}$  and  $\text{Sr}^{2+}$  can as also potentially reduce leakage.

## References

- [1] L. Liang, Y. L. Li, L.-Q. Chen, S. Y. Hu, G.-H. Lu, *J Appl Phys* **2009**, *106*, DOI 10.1063/1.3260242.
- [2] A. Nazeri-Eshghi, A. X. Kuang, J. D. Mackenzie, *J Mater Sci* **1990**, *25*, 3333.
- [3] S. Triebwasser, *Physical Review* **1956**, *101*, 993.
- [4] G. Shirane, H. Danner, A. Pavlovic, R. Pepinsky, *Physical Review* **1954**, *93*, 672.
- [5] G. Sheng, Y. L. Li, J. X. Zhang, S. Choudhury, Q. X. Jia, V. Gopalan, D. G. Schlom, Z. K. Liu, L. Q. Chen, *Appl Phys Lett* **2010**, *96*, DOI 10.1063/1.3442915.
- [6] M. J. Haun, E. Furman, S. J. Jang, H. A. McKinstry, L. E. Cross, *J Appl Phys* **1987**, *62*, 3331.
- [7] Y. L. Li, L. E. Cross, L. Q. Chen, *J Appl Phys* **2005**, *98*, DOI 10.1063/1.2042528.
- [8] H. Uwe, T. Sakudo, *J Physical Soc Japan* **1975**, *38*, 183.
- [9] M. J. Weber, *Handbook of Optical Materials*, CRC Press, **2018**.
- [10] L. Chen, *Journal of the American Ceramic Society* **2008**, *91*, 1835.
- [11] B. Wang, L.-Q. Chen, *Acta Mater* **2024**, *274*, 120025.
- [12] B. Wang, H.-N. Chen, J.-J. Wang, L.-Q. Chen, *Appl Phys Lett* **2019**, *115*, DOI 10.1063/1.5116910.
- [13] L. F. Wan, T. Nishimatsu, S. P. Beckman, *J Appl Phys* **2012**, *111*, DOI 10.1063/1.4712052.
- [14] R. Uecker, B. Velickov, D. Klimm, R. Bertram, M. Bernhagen, M. Rabe, M. Albrecht, R. Fornari, D. G. Schlom, *J Cryst Growth* **2008**, *310*, 2649.
- [15] W. Zheng, Y. Tang, C. Jia, Z. Liu, Z. Zhang, K. Zhao, *J Mater Chem A Mater* **2024**, *12*, 11378.
- [16] A. Winiarski, T. Neumann, B. Mayer, G. Borstel, M. Neumann, *physica status solidi (b)* **1994**, *183*, 475.
- [17] T. Zhang, K. Zhao, J. Yu, J. Jin, Y. Qi, H. Li, X. Hou, G. Liu, *Nanoscale* **2013**, *5*, 8375.
- [18] V. Gopalan, R. Raj, *Appl Phys Lett* **1996**, *68*, 1323.
- [19] V. Gopalan, R. Raj, *J Appl Phys* **1997**, *81*, 865.
- [20] R. Zu, B. Wang, J. He, L. Weber, A. Saha, L.-Q. Chen, V. Gopalan, *NPJ Comput Mater* **2024**, *10*, 64.
- [21] Y. Shiozaki, E. Nakamura, T. Mitsui, Eds., *Oxides*, Springer-Verlag, Berlin/Heidelberg, **2002**.
- [22] B. Ofuonye, J. Lee, M. Yan, C. Sun, J.-M. Zuo, I. Adesida, *Semicond Sci Technol* **2014**, *29*, 095005.
- [23] V. Sampath Kumar, M. K. Niranjan, *J Appl Phys* **2014**, *115*, DOI 10.1063/1.4872466.
- [24] R. I. Eglitis, E. A. Kotomin, A. V. Postnikov, N. E. Christensen, M. A. Korotin, G. Borstel, *Ferroelectrics* **1999**, *229*, 69.
- [25] R. I. Eglitis, N. E. Christensen, E. A. Kotomin, A. V. Postnikov, G. Borstel, *Phys Rev B* **1997**, *56*, 8599.
- [26] J. Handerek, R. Manka, A. Aleksandrowicz, J. Szatanek, *Ferroelectrics* **1978**, *22*, 735.
- [27] S. Torbrügge, M. Imlau, B. Schoke, C. Merschjann, O. F. Schirmer, S. Vernay, A. Gross, V. Wesemann, D. Rytz, *Phys Rev B* **2008**, *78*, 125112.

- [28] G. Singh, V. S. Tiwari, P. K. Gupta, *J Appl Phys* **2010**, *107*, DOI 10.1063/1.3309745.
- [29] Y. Wu, M. J. Forbess, S. Seraji, S. J. Limmer, T. P. Chou, G. Cao, *J Appl Phys* **2001**, *89*, 5647.
- [30] R. I. Eglitis, E. A. Kotomin, G. Borstel, *physica status solidi (c)* **2005**, *2*, 113.
- [31] A. K. Yadav, C. T. Nelson, S. L. Hsu, Z. Hong, J. D. Clarkson, C. M. Schlepütz, A. R. Damodaran, P. Shafer, E. Arenholz, L. R. Dedon, D. Chen, A. Vishwanath, A. M. Minor, L. Q. Chen, J. F. Scott, L. W. Martin, R. Ramesh, *Nature* **2016**, *530*, 198.